UNIVERSITA' DEGLI STUDI DI PADOVA

DIPARTIMENTO DI INGEGNERIA INDUSTRIALE

Corso di Laurea Magistrale in Ingegneria Elettrica

TESI DI LAUREA MAGISTRALE

MULTIOBJECTIVE OPTIMIZATION TECHNIQUES FOR THE SOLUTION OF FREE-BOUNDARY PLASMA EQUILIBRIUM INVERSE PROBLEMS

OTTIMIZZAZIONE MULTIOBIETTIVO PER LA SOLUZIONE DI PROBLEMI INVERSI DI EQUILIBRIO DI PLASMA FREE-BOUNDARY

Relatore: Prof. Paolo Bettini

Laureando: Domenico Abate

Anno accademico
2013-2014

UNIVERSITA' DEGLI STUDI DI PADOVA

DIPARTIMENTO DI INGEGNERIA INDUSTRIALE

Corso di Laurea Magistrale in Ingegneria Elettrica

TESI DI LAUREA MAGISTRALE

MULTIOBJECTIVE OPTIMIZATION TECHNIQUES FOR THE SOLUTION OF FREE-BOUNDARY PLASMA EQUILIBRIUM INVERSE PROBLEMS

OTTIMIZZAZIONE MULTIOBIETTIVO PER LA SOLUZIONE DI PROBLEMI INVERSI DI EQUILIBRIO DI PLASMA FREE-BOUNDARY

Relatore: Prof. Paolo Bettini

Laureando: Domenico Abate

Anno accademico
2013-2014

Abstract

Lo scopo di questo studio è quello di sviluppare un codice per la soluzione numerica del problema inverso per l'equilibrio di plasmi confinati magneticamente con un approccio di ottimizzazione multiobiettivo e un controllo analitico funzionale della forma del boundary di plasma. Il problema inverso consiste nel determinare i valori ottimali di correnti circolanti nelle bobine attive della macchina tali da mantenere in equilibrio un plasma il cui boundary sia il più vicino possibile a quello prestabilito mediante l'uso del modello analitico funzionale. Il modello, basato sulla famiglia di funzioni chiamate superellissi, fornisce i mezzi per caratterizzare boundary di plasmi in configurazione Limiter e anche per generare una famiglia di soluzioni variando il solo grado di libertà, denominato "squareness ", e mantenendo costanti gli altri parametri di forma. Il modello è stato esteso ai plasmi in configurazione Divertor, senza perdere la possibilità di controllare la forma del boundary, mediante l'uso di una funzione interpolante basata sulle curve di Bézier che permette di interpolare l'insieme ordinato di punti ai minimi quadrati, riducendo cioè al minimo la somma dei residui in entrambe le direzioni, con una curva chiusa che realizzi il punto angoloso rappresentato dall'X-point. Partendo dalla caratterizzazione fornita dal modello analitico è stata svillupata una mesh strutturata specificata da funzioni implicite, utilizzando *DistMesh*, un codice open source basato su un semplice algoritmo che combina il principio fisico di equilibrio delle forze in una struttura reticolare con una rappresentazione matematica della geometria usando una funzione distanza. La seconda parte della tesi riguarda lo studio dell'equilibrio magnetoidrodinamico di un plasma da fusione. Inizialmente le sorgenti di campo magnetico, ovvero le bobine attive del sistema magnetico, sono state modellate con diversi metodi numerici ed i risultati sono stati confrontati per determinare il modello ottimale. In seguito si è proseguito con la determinazione dell'equilibrio risolvendo l'equazione di Grad-Shafranov mediante una formulazione algebrica globale, nota anche come "metodo delle celle", in uno schema iterativo di Picard. Si è ipotizzata nota la posizione spaziale del boundary del plasma, fornita dal modello funzionale analitico, quindi il problema è stato riformulato imponendo una condizione al contorno di flusso magnetico costante in corrispondenza del boundary di plasma. L'equilibrio è stato risolto per i due casi tipici di plasma Limiter e Divertor analizzando la procedura iterativa nelle sue dinamiche di convergenza. Infine si è affrontato il problema inverso per le correnti con un approccio di ottimizzazione basato su logica fuzzy. La prima soluzione ottenuta con tecnica SVD è stata ottimizzata usando algoritmi evoluzionistici.

Acknowledgements

Domenico Abate would like to thank everyone that helped make this thesis exist: God, Family, Prof. Paolo Bettini, Prof. Piergiorgio Alotto, Doct. Andrea Garbo, S.T. Richter, J.A. Gillis, J. Milton, Don Van Vliet, Friends, Fools and C.P., the only responsible of the road so far.

Contents

List of Figures

List of Tables

Nomenclature

κ	Elongation
a	Minor radius
R_{geo}	Major radius
ϵ^*	Inverse aspect ratio
δ	Triangularity
A	Minor semi-axis
B	Major semi-axis
ξ	Squareness
$\mathbf{P}(t)$	Bézier curve
t	Bézier curve parameter
$B_{n,i}(t)$	Bernstein polynomial
$\mathbf{P}$	Bézier control point
$\mathbf{P}^t(t)$	Tangent vector
$\mathbf{Q}$	Data point
$B(t)$	Bernstein matrix
P	Control points matrix
Q	Data points matrix
$[M(t)]$	Bernstein uncoupled block matrix
$[P]$	Control points block matrix
$[Q]$	Data points block matrix
$M(t)*$	Moore-Penrose generalized inverse matrix
$d(x, y)$	Signed distance function
$h(x, y)$	Edge length function
G	Green Matrix
ϵ	Per cent relative error
p	Static pressure
F	Poloidal current function
ψ	Magnetic poloidal flux
ε	Relative magnetic flux per cent error
R	Residual
X	Unknown vector of coils currents
f	Objective function
z	Membership function

Chapter 1

Introduction

The most promising results in the controlled thermonuclear fusion research field has been obtained by using closed magnetic confinement plasma devices such as Tokamaks. Starting from the development of Tokamaks in the Soviet Union followed from theoretical ideas of Tamm and Sakharov [4] through the late 1970s large scale ignition experiments, the history brings to the project of the International Thermonuclear Experimental tokamak-Reactor (ITER). This project has the crucial role of being the flagship facility for the world's fusion program for the next decades.

One of the main key role in controlled magnetic fusion science is covered by the plasma equilibirum and stability problems since they have far reaching consequences in the design and operation of present and future fusion devices. The necessary condition to succesfully design the fusion devices and predict plasma preformances is the development of mathematical models and computational codes to simulate and analyze the plasma behaviour in the device and, in particular, to solve the plasma equilibirum problems. The basic equation of the axysimmetrically plasma toroidal equilibrium is a second-order elliptic non-linear partial differential equation of the magnetic flux, known as "Grad-Shafranov" equation. In addition to the possible analytical solutions, which provide an understanding of the basic effects, numerical methods are required for exact calculations of desired equilibrium configurations characterized by desired plasma pressure and current density profiles. Throughout the 1970s various numerical methods were developed, investigated, and applied to various numerical equilibrium codes to solve the Grad-Shafranov equation [6]. The computation of axi-symmetric plasma equilibrium configurations and their stability analysis is an important problem, which provides data for optimization of the magnetic system parameters in tokamaks.

The plasma equilibrium problem can be divided in two broad classes: *direct* and *inverse* equilibrium problem. The *direct equilibrium problem*, mainly for the analysis of transient electro-magnetic phenomena, is the computation of the evolution of the plasma current, shape and current profile parameters, in presence of assigned external currents, flowing in the Poloidal Field PF coils (equilibrium currents) and in the surrounding metallic structures (eddy currents) [7].

On the other hand, in the *inverse equilibrium problem*, which is mainly applied for the Poloidal Field (PF) system design purposes, it is required to compute the currents in the PF coils to keep in equilibrium a plasma with the boundary as close as possible to a pre-defined boundary flux line, total current Ip and current density profile (typically the plasma poloidal beta β_p and internal inductance li are assigned) [7].

Both of these problems are related to the numerical solution of the Grad-Shafranov equation

inside an a-priori unknown domain. This problem can be described by using two main formulations, each one defined by the type of imposition of the boundary conditions at the plasma surface: the free boundary equilibrium problem and the fixed boundary equilibrium problem. The free boundary equilibrium problem is solved over an infinite domain with unknown position of the plasma boundary which complicates the solution of the problem that, in essence, is a fairly standard elliptic type problem with a (mild) non-linearity deriving from the fairly smooth dependence of the source term upon the flux function . The fixed boundary equilibrium problem is defined over a finite domain with prescribed fixed plasma boundary which corresponds to the solution of a boundary value problem with the boundary condition $\psi = const.$ at the plasma boundary so the Grad-Shafranov equation is solved only in the plasma region.

The aim of this study is to develop a procedure code for the numerical solution of the Inverse equilibrium problem for magnetically confined fusion plasmas with a multiobjective optimization approach and an analytical functional control of the plasma boundary shape. The first part of this study concerns the definition of the plasma region, in which the plasma inverse equilibrium problem will be solved. An analytical functional model has been developed in order to characterize Limiter plasma boundaries and to generate family of solutions by varying a freedom parameter. Thus provides an additional degree of freedom in the multiobjective optimization of the inverse equilibrum problem for the external currents. The model has been extended to the Divertor plasma boundaries, i.e. with X-point, by developing a Bézier curve interpolating function. Starting from the boundary characterization given by the models, an unstructured mesh for this geometry, specified by implicit functions, is obtained.

The second part of the study concerns the solution of the inverse fixed boundary plasma equilibrium problem. It consists on the indentification of the optimal values for the PF currents by means of a multiobjective optimization approach. First of all, the magnetic field sources has been modelled with different numerical methods and the results has been compared. Then, the Grad-Shafranov equation has been solved for the fixed plasma equilibrium problem by using a direct algebraic global formulation, i.e. cell method, in an iterative Picard scheme. Finally the inverse problem for the currents has been solved with a multiobjective optimization approach based on evolutionary algorithms (Different Evolution and Particle Swarm Optimization). The initial solution is based on SVD technique and the four objective functions has been reduced to a single objective function by using a fuzzy logic.

Chapter 2

An analytical functional model for plasma boundaries

2.1 Introduction

Plasma boundaries of existing magnetic confinement devices, as Tokamaks, are generally described by using a compact notation of five standard parameters. This compact charatecterization of the geometric shape of an axisymmmetric toroidal plasma is used in many fields. Confinement scalings that are used to project fusion gain in burning plasmas in tokamaks employ basic shaping parameters as variables. Magnetohydrodynamic (MHD) stability of tokamak plasmas that has been cast in terms of similar geometric parameters but generally with a larger number of parameters. The design of the poloidal field coil systems for fusion experiments which requires the means to generate the boundary condition for the equilibrium solver, including the possibility of X-points[8].

The analytic functional model proposed here provides the means to characterize boundaries of plasmas in Limiter configuration and also to generate a family of solutions by varying only a single parameter: it is possible to generate a series of boundaries where the "freedom parameter" is changed but the remaining shape parameters are fixed. These variations can then be used to generate equilibria for testing models; for example models of pedestal stability, energy transport or the magnitude of fast ion ripple loss. Second, this form can be used to determine whether the distribution of coil currents required to make a desired shape that has not been made previously are within the capabilities of a given coil set [8]. The model can be also used as a starting point to characterize and generate plasma boundaries in the Divertor configuration, i.e. with X-point, by using a Bezier interpolating function. The original model proposed by T C Luce [8], which allows only up-down asymmetry, has been extended to provide both up-down and left-right asymmetry, i.e. asymmetry with respect of a system of two-dymensional orthogonal axes, positioned at the center of the plasma whose are respectively parallels to the main reference R and Z axes, leading to a more detailed characterization of boundaries.

2.2 Boundary layer configurations

The magnetic confinement devices the plasma is confined within closed magnetic flux surfaces which are generated by a combination of fields due to both contributions of external coils currents

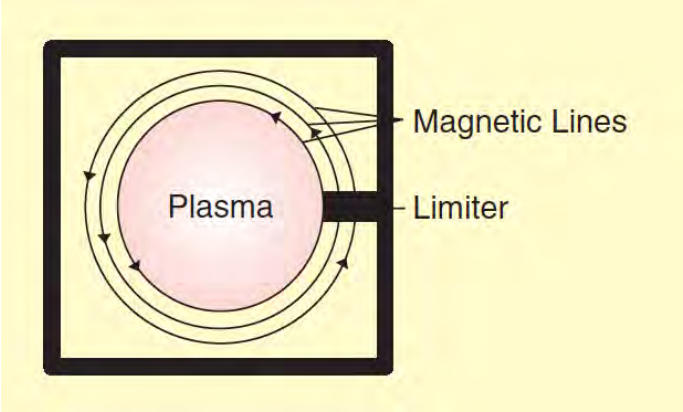

Figure 2.1: [1] Limiter configuration

and plasma current. Since fields can be generated only inside a portion of a restricted volume of the space, it is obvious the existence of a plasma boundary which is the outermost closed flux surface entirely contained inside the vacuum vessel. The boundary is therefore determined by the last closed flux surface (LCFS) and the shape of this is determined by the external magnetic fields. There are two different configurations for the plasma LCFS: "Limiter" and "Divertor". In the first one, the closed magnetic surfaces are interrupted by a solid surface, called Limiter, which determines the position of the LCFS. In this way, the external layer of the plasma magnetic lines are intercepted by the limiter, and the LCFS is kept separated from the first wall. In other words, the mechanical limiter protects the chamber from plasma bombardment and serves to define the edge of the plasma (Fig. 2.1). In the second configuration, the LCFS is entirely determined by the magnetic fields due to the magnetic Divertor so that, outside the LCFS, the plasma flows towards and interact with the Divertor solid surface (Fig. 2.2). The magnetic divertor is a structure that creates a magnetic configuration where the external layer of magnetic lines is guided away from the main plasma and collides onto a collector plate. A poloidal divertor is obtained by placing several coils near the plasma surface, with a current parallel to that of the plasma and flowing in the opposite direction, to generate a local field that opposes the poloidal field in the plasma. Consequently, the resulting magnetic field is locally characterized by the presence of a null point, or equivalently the flux function presents a saddle point (X-point), and thus the magnetic surface defining the plasma boundary is referred to as the separatrix. In other words, the divertor locally modifies the magnetic lines so that the main plasma does not contact the vessel. The magnetic lines external to tha plasma boundary collide onto a collector plate equiped with cryocondensation pumps to remove impurities, which could reenter the plasma [1].

The essential difference between the two is that with a limiter the LCFS is in contact with a solid surface, while with a divertor the solid surface is removed some distance from the LCFS, thus reducing the flux of impurities or recycling particles which get directly back inside the LCFS [2] (Fig. 2.3). Those concepts provide the possibility to give a topologically definition of the plasma boundary which is the outermost flux contour not intersecting any solid object (Limiter configuration) or it is a separatrix, that is a surface containing an X-point. The X-point often exists independently of whether it is a part of the most external closed flux surface [1].

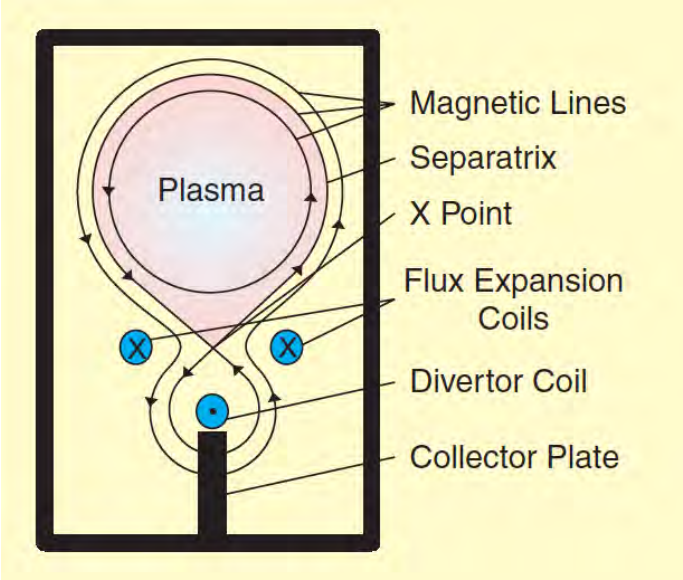

Figure 2.2: [1] Divertor configuration

2.3 Generalized shape parameters

Plasma shape is, in general, geometrically described by a collection of a small number of global shape parameters which are used by physics and engineers to develop reactor-relevant scenarios needed to improve high fusion performances. A general approach for the definition of this collection starts by the definition of the plasma cross section area A, which is important to estimate the nuclear reaction volume. Then other quantities such the elongation κ and the triangularity δ are defined and used to describe the distribution of the cross section area A with respect to the poloidal section. Elongation κ is a characteristic of the plasma poloidal cross section, defined as the ratio of the plasma sectional area A to the area of a circle having the same minor radius a as the plasma:

$$\kappa = \frac{A}{\pi a^2} \tag{2.1}$$

where the minor radius a of a noncircular plasma is defined as the semidistance between the outermost and innermost points of the boundary curve [1]. This approach is not usefull for the purpose of this aim. In the poloidal plane RZ, the plasma is geometrically identifiable by using four extremal parameters, therefore the calculation of the global shape parameters can be done with respect of those local point-based information of the plasma cross section despite the using of integral parameters such the cross section area. The elongation is computed as:

$$\kappa = \frac{z_{max} - z_{min}}{r_{max} - r_{min}} \tag{2.2}$$

From the four extremal points, the following standard definitions and nomenclature are made [8].

- Major radius:

$$R_{geo} = \frac{R_{max} + R_{min}}{2} \tag{2.3}$$

- Minor radius:

$$a = \frac{R_{max} - R_{min}}{2} \tag{2.4}$$

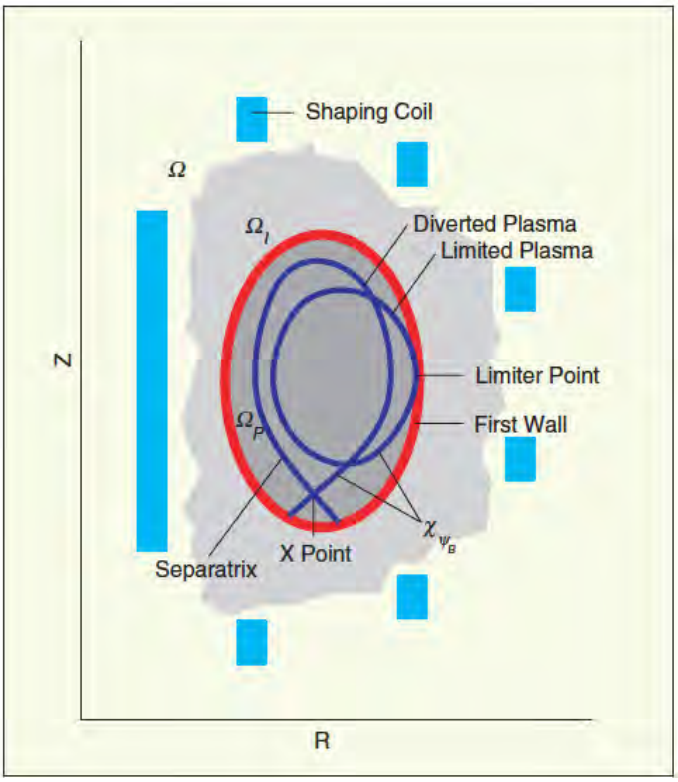

Figure 2.3: [2]Limiter-Divertor configuration

- Inverse aspect ratio:

$$\epsilon^* = \frac{a}{R_{geo}} \tag{2.5}$$

- Elongation:

$$\kappa = \frac{z_{max} - z_{min}}{2a} \tag{2.6}$$

- Upper Triangularity:

$$\delta_u = \frac{R_{geo} - R_{Z_{max}}}{a} \tag{2.7}$$

- Lower Triangularity:

$$\delta_l = \frac{R_{geo} - R_{z_{min}}}{a} \tag{2.8}$$

where the triangularity δ indicates the extent to which the plasma assumes a triangular shape.

2.4 Additionally shape parameters

The model is geometrically based on the construction of a four quadrant structure, derived from the four plasma extremal points, starting from the definition of four axes whose intersections will define the four centers of the quadrants. In addition to the standard parameters is therefore necessary, in order to obtain the final analytical model, to define an additional set of new parameters, four of which are a straightforward extension, over the four quadrants, of the elongation defined in Eq. 2.6. In other words, in order to maintain the possibility of a different height for the minimum major radius R_{min} and for the maximum major radius R_{max}, i.e. $Z_{R_{min}}$ and $Z_{R_{max}}$, a separate

Quadrant		x	y	A	B
I	Upper outer	$R - R_{Z_{max}}$	$z - z_{R_{max}}$	$R_{max} - R_{z_{max}}$	$z_{max} - z_{R_{max}}$
II	Upper inner	$R_{Z_{max}-R}$	$z - z_{R_{min}}$	$R_{z_{max}} - R_{min}$	$z_{max} - z_{R_{min}}$
III	Lower inner	$R_{Z_{min}} - R$	$z_{R_{min}} - z$	$R_{z_{min}} - R_{min}$	$z_{R_{min}} - z_{min}$
IV	Lower outer	$R - R_{Z_{min}}$	$z_{R_{max}} - z$	$R_{max} - R_{z_{min}}$	$z_{R_{max}} - z_{min}$

Table 2.1: Definitions of the parameters of the ellipse reference for the four quadrants

elongation for each quadrant of the plasma is defined:

$$\kappa_I = \frac{z_{max} - z_{R_{max}}}{a} \tag{2.9}$$

$$\kappa_{II} = \frac{z_{max} - z_{R_{min}}}{a} \tag{2.10}$$

$$\kappa_{III} = \frac{z_{R_{min}} - z_{min}}{a} \tag{2.11}$$

$$\kappa_{IV} = \frac{z_{R_{max}} - z_{min}}{a} \tag{2.12}$$

where

$$Z_{r_{max}} \equiv Z_{off_{1-4}} \tag{2.13}$$

$$Z_{r_{min}} \equiv Z_{off_{2-3}} \tag{2.14}$$

$$R_{z_{max}} \equiv R_{off_{1-4}} \tag{2.15}$$

$$R_{z_{min}} \equiv R_{off_{2-3}} \tag{2.16}$$

are the four quadrant axes. Those definitions means that the vertical offset of the plasma along the axes $Z_{off_{1-4}}$ and $Z_{off_{2-3}}$ is respectively referenced to the height of the maximum radius R_{max} and minimum radius R_{min}. Similarly for the horizzontal offset along the axes $R_{off_{1-4}}$ and $R_{off_{2-3}}$.

Even without introducing the mathematical form of the analytical model, it is intuitive to expect that the boundary will be characterized in four different parts, one for each quadrant. The "freedom parameter" also is not single but in fact it assumes four values, again, one for each quadrant. This new set of parameters is a set of "shaping degree of freedom" of the analytical model each one consists of a measure of the curvature of the boundary between the extremal points. This measure, i.e. the "freedom parameter", will be called the *squareness*. In order to define the *squareness*, two new references must be introduced.

The first one is an ellipse connecting one of the radius extrema to one of the elevation extrema and described by the standard analytic form:

$$\frac{x^2}{A^2} + \frac{y^2}{B^2} = 1 \tag{2.17}$$

where A and B are respectevely the minor and the major semi-axes. The definitions of the parameters for generating reference ellipses for the four quadrants are given in Tab. 2.1. A particular note must be done in the definitions of the two cartesian coordinates in Tab. 2.1: x and y are defined positive, with reference of the centre of the quadrant, for each quadrant. This is fondamental for the later mathematical form of the analytical model, which will have non-integer exponents. The second reference is the diagonal bisecting the quadrant bounding box; in the

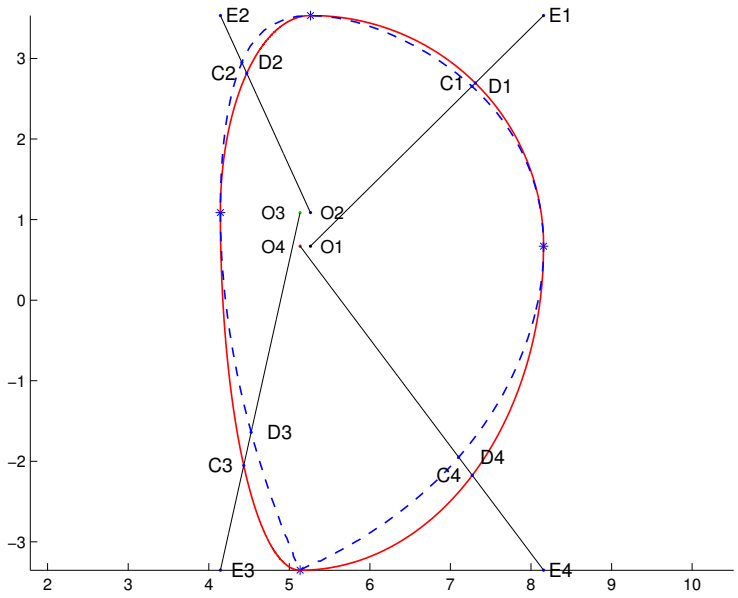

Figure 2.4: Quadrant references for the squareness calculation for Diverted plasma boundary

fourth quadrant, i.e. lower outer quadrant, this diagonal is the line segment OE, that connects the centre of the quadrant O with the intersection point between the diagonal and the reference ellipse of the quadrant. Another intersection point between the bisecting diagonal and the actual, or desired, boundary is defined as point D. In Fig. 2.4 and Fig. 2.5 are shown: the reference ellipse in red line, the four diagonals and intersection points and the real plasma boundary in blue dashed line. Now the squareness can be defined as:

$$\xi_{IV} = \frac{L_{OD} - L_{OC}}{L_{CE}} \tag{2.18}$$

where L is the length of the line segment connecting the two points in the subscript. The *squareness* is literally the condition of being square. It provides a geometrical comparison information between the desired boundary and the reference ellipse for each quadrant. By analyzing three typical range of values of ξ it is possible to give a practical behaviour of this parameter:

- for $\xi \longrightarrow 1$ the plasma boundary will conform to the quadrant bounding box, having a "square" corner; more in general if $\xi > 0$ than the boundary is more square than the ellipse.
- for $\xi = 0$ plasma boundary corresponds exactly to the ellipse.
- for $\xi < 0$ plasma boundary is less square, i.e. has lower squareness, than the ellipse.

2.5 Analytical model for Limiter plasma boundaries

With definitions in Sect. 2.4 it is now possible to introduce the mathematycal form used to obtain the analytical functional model for plasma boundaries in Limiter configuration, i.e. without X-points. The analytic form adopted is that of the family of superellipses, also known as a special case of Lamé curves who was the first to discuss these curves in 1818 [9].

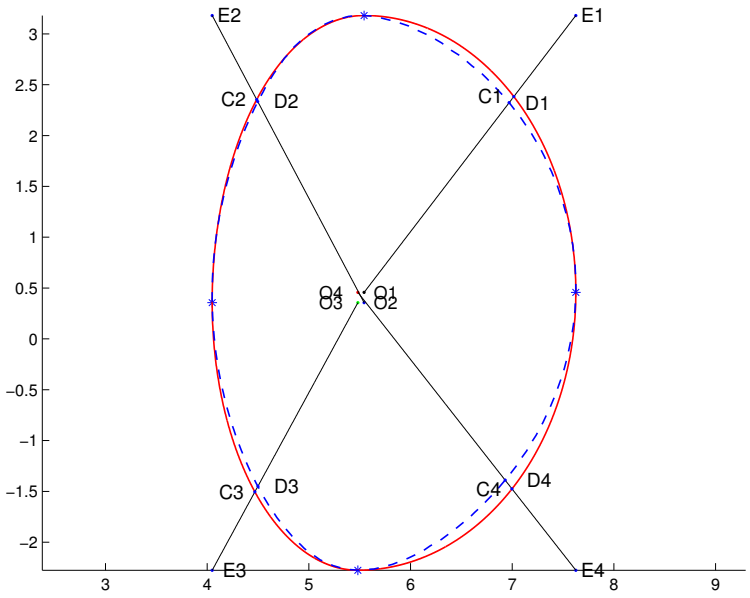

Figure 2.5: Quadrant references for the squareness calculation for Limited plasma boundary

A superellipse is basically an extension of the Eq. 2.17, defined in the Cartesian coordinate system as the set of points (x, y) with:

$$(\frac{x}{A})^n + (\frac{y}{B})^n = 1 \tag{2.19}$$

where n is a positive rational number and A,B are positive. If n assumes rational values then the curve is algebraic but, for irrational values the curve is trascendental. For Lamé curves n can be any rational number. From the topological point of view, there are nine different types of Lamé curves depending on the form of the exponent (Fig. 2.6). The superellipse formula (Eq. 2.19) defines a closed curve contained in the rectangle $-A \leq x \leq A$ and $-B \leq y \leq B$ and which shape is determined by the value assumed by the exponent n. It's possible to indicate two categories of this curve: for $n > 2$, the hyperellipses and for $n < 2$ the hypoellipses: the particular cases $n = 2$ and $n = 1$ defines respectevely the ellipse and the rhombus (Fig. 2.7).

The choice of superellipse is determined by their fondamental property of being continuous and differentiable across all of the matching points, $x = 0$ or $y = 0$, since the limiting values of the derivative in these points, approached from different sides, do not depend on the values of the superellipses parameters A, B or n. This allows A, B and n to assume different values in each quadrant. In other words the superellipse allows to treat each quadrant separately, as already done in the definitions of the additionally shape parameters in Sect. 2.4. For each quadrant there are three unknowns (A,B,n) that must be determined from geometrical constraints. The values of the two semi-axes are the same of Tab. 2.1, but instead to express them in terms of the extremal coordinates it is usefull to redefine them, without loss of generality, as a linear combination of dimensionless geometric quantities, defined in Sect. 2.3 and three dimensional quantities a, $Z_{off_{1-4}}$, $Z_{off_{2-3}}$.

The value of n in each quadrant is univocally determined by the value of the squareness ξ in

Quadrant		x	y	A	B	n
I	Upper outer	$R - a(1/\epsilon^* - \delta_u)$	$z - Z_{off_{1-4}}$	$a(1+\delta_u)$	$a\kappa_I$	$-\ln(2)/\ln[1/\sqrt{2} + \xi_I(1-1/\sqrt{2})]$
II	Upper inner	$a(1/\epsilon^* - \delta_u) - R$	$z - Z_{off_{2-3}}$	$a(1-\delta_u)$	$a\kappa_{II}$	$-\ln(2)/\ln[1/\sqrt{2} + \xi_{II}(1-1/\sqrt{2})]$
III	Lower inner	$a(1/\epsilon^* - \delta_l) - R$	$Z_{off_{2-3}} - z$	$a(1-\delta_l)$	$a\kappa_{III}$	$-\ln(2)/\ln[1/\sqrt{2} + \xi_{III}(1-1/\sqrt{2})]$
IV	Lower outer	$R - a(1/\epsilon^* - \delta_l)$	$Z_{off_{1-4}} - z$	$a(1+\delta_l)$	$a\kappa_{IV}$	$-\ln(2)/\ln[1/\sqrt{2} + \xi_{IV}(1-1/\sqrt{2})]$

Table 2.2: Definitions of the superellipse parameters in each quadrants in terms of dimensionless geometric parameters

ξ_I	-0.0749
ξ_{II}	-0.0235
ξ_{III}	-0.0707
ξ_{IV}	-0.1075

Table 2.3: Squareness values for the characterized ITER Limiter plasma boundary

that quadrant by using the fact that point D of each quadrant, in Fig. 2.4, must lie both on the quadrant portion of superellipse, defined by Eq. 2.19, and on the diagonal reference, i.e. the line OE [8]. The new formulations of superellipse parameters for each quadrant are transcripted in Tab. 2.2. This definition of n, as a function of ξ, highlights the interpretation of the squareness as a measure of the relative position of the boundary with respect of the reference ellipse.

The only relevant limitation in the analytical model for limiter boundaries is that it can not characterize and generate indented plasmas and plasmas with higher order indentations. This limit is due to the convex hull property of the superellipse which permits to generate curves that are everywhere convex. Despite this limitation, the form invoked here should suffice to generate the vast majority of plasmas of interest for experimental analysis and theoretical study [8].

2.6 Results

As introduced in Sect. 2.1, the model already introduced gives the possibility to generate a family of boundary solution starting by varying the *freedom parameter*, which has been introduced in Sect. 2.4 as the *squareness* ξ, but with no modifications on the remaining shape parameters, which are and remain fixed. Starting from the first boundary solution, i.e. the superellipse characterization of the original boundary, it is possible to determine the four original values of the squareness, each one for each quadrant, and then to modify one or all of them in order to generate new plasma boundaries.

For example: the Limiter plasma boundary shown in blue line in Fig. 2.8, is obtained by using the analytical Limiter model applied to the experimental equilibrium data points from the ITER equilibria database [10]. This boundary is characterized by four values of the *squareness* ξ (Tab. 2.3) which must be modified in order to obtain new boundary solutions: by imposing the same ξ values for the four quadrants, a huniform plasma boundary is obtained and its shape is determined by the value of ξ as shown in Fig. 2.9 and Fig. 2.10 and as described in Sect. 2.4.

It is possible also to modify just one or more of the four quadrant values of ξ in order to modify the shape of the plasma boundary of that modified quadrant: few examples of this are shown in Fig. 2.11 and Fig. 2.12. This procedure is still valid starting from a Diverted plasma boundary as shown in Fig. 2.13 and Fig. 2.14.

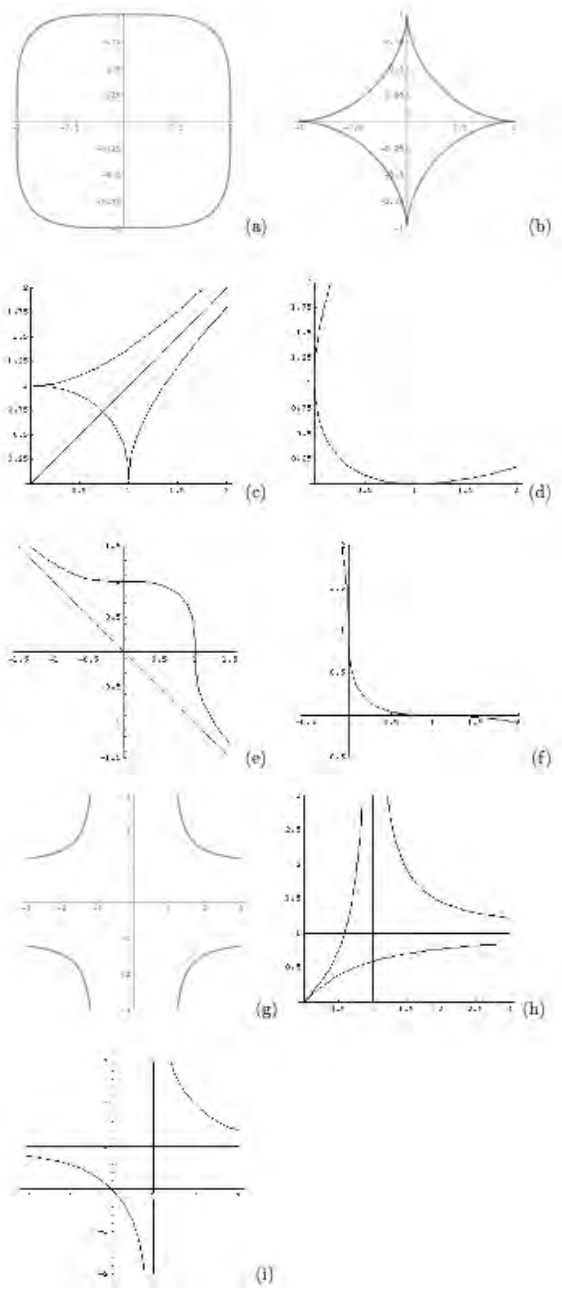

Figure 2.6: Lamé curves with positive, (a) to (f), and negative, (g) to (i) exponent: only the first two types (a) and (b) are superellipses.

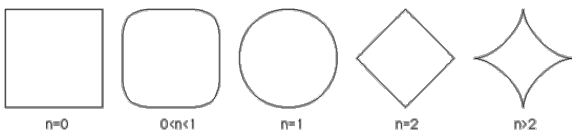

Figure 2.7: Typical cases of superellipses

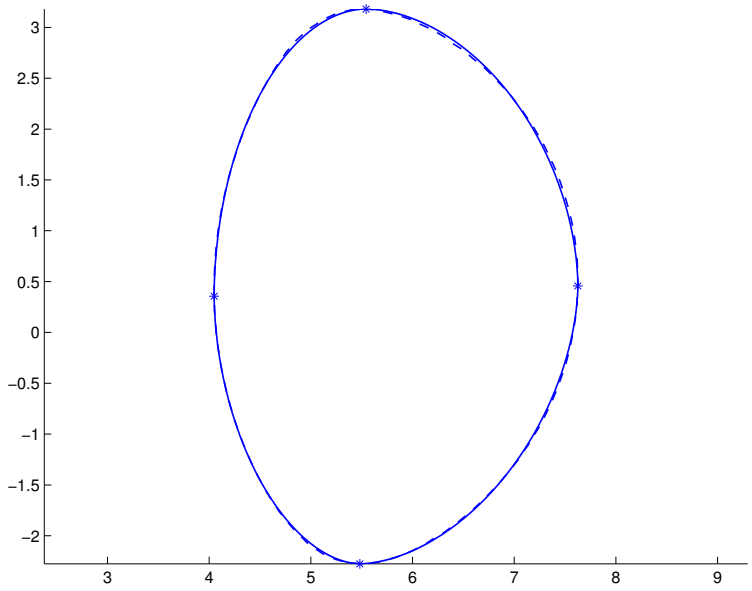

Figure 2.8: Characterization of a real Limiter plasma boundary

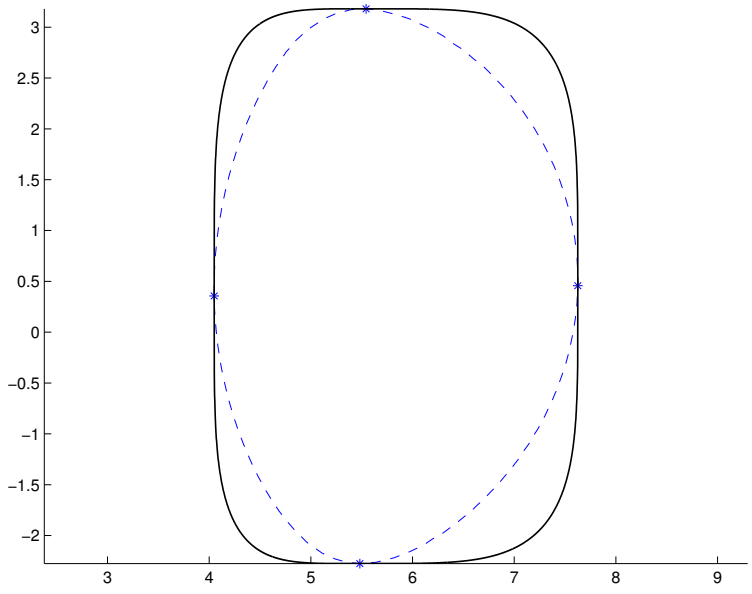

Figure 2.9: Generated plasma boundary by imposing $\xi = 0.5$ for all the four quadrants

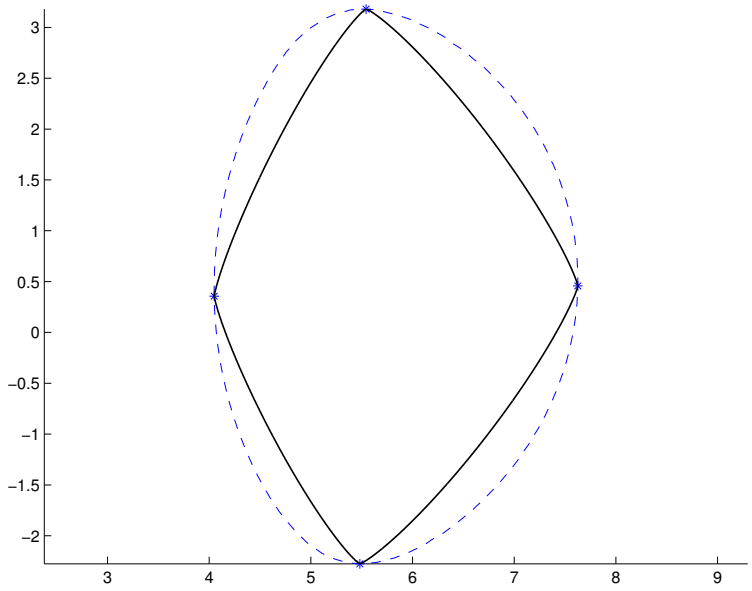

Figure 2.10: Generated plasma boundary by imposing $\xi = -0.5$ for all the four quadrants

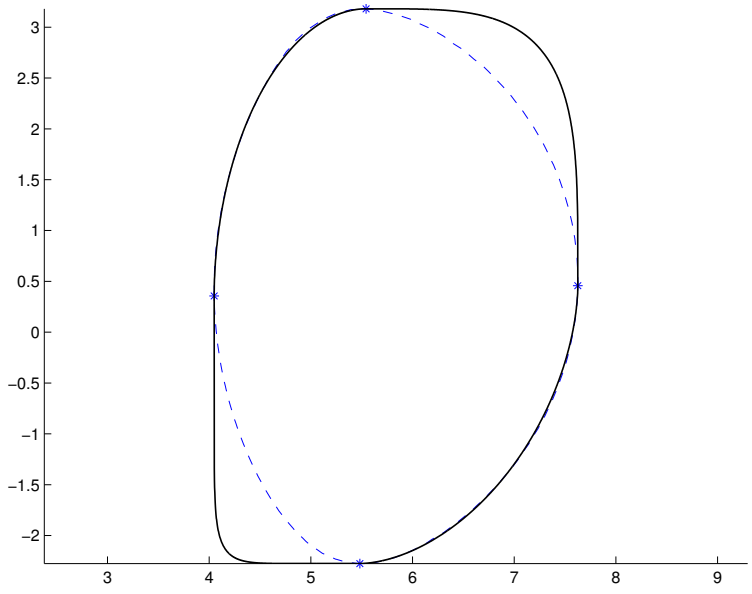

Figure 2.11: Generated plasma boundary by imposing $\xi_I = 0.45$ and $\xi_{III} = 0.78$

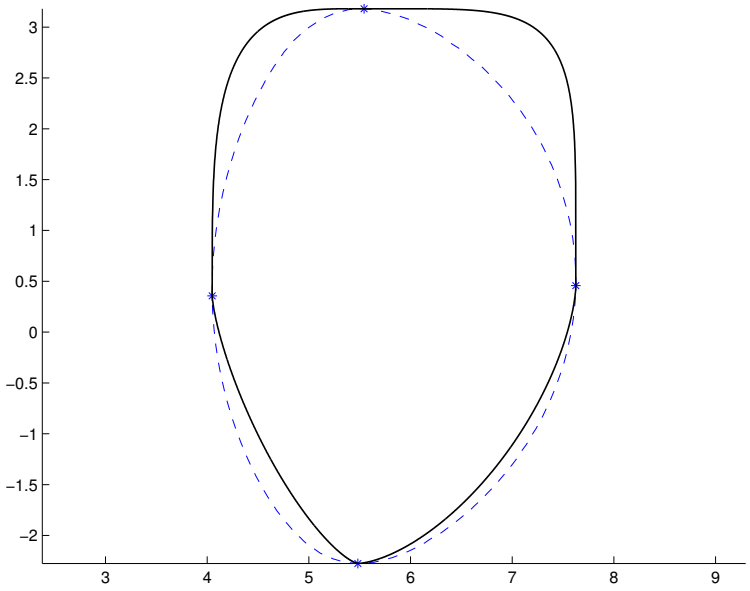

Figure 2.12: Generated plasma boundary by imposing $\xi_I = 0.58$, $\xi_{II} = 0.42$, $\xi_{III} = -0.35$ and $\xi_{IV} = -0.22$

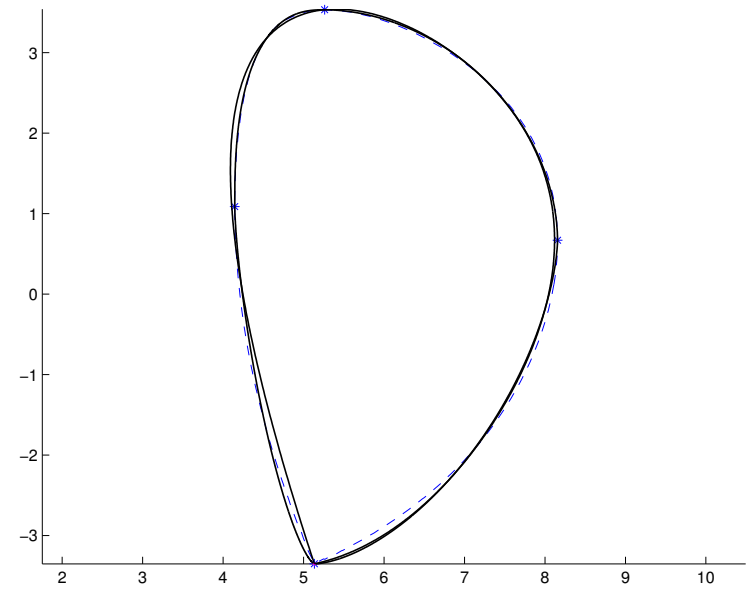

Figure 2.13: Characterization of a real diverted plasma boundary (without representation of the X-point)

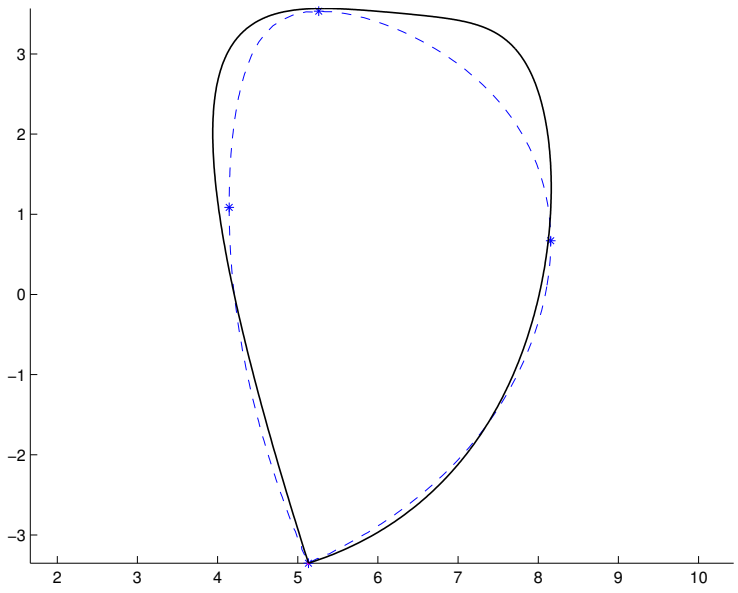

Figure 2.14: Generated plasma boundary by imposing $\xi_I = 0.45$, $\xi_{II} = 0.58$

Chapter 3

Extended analytical model for divertor plasma boundaries

3.1 Introduction

The model introduced for Limiter boundaries (Sect. 2.5) provide a characterization and generation of boundaries which are continuous and differentiable in every point. These important properties eliminate a whole category of boundary shapes relative to the plasmas with a divertor configuration, i.e. with an X-point where the magnetic field orthogonal to the direction of simmetry has a null. Diverted plasmas can not be represented by a closed form solution just because of the X-point. The analytic form can be extended in a manner for which a closed-form solution can not been found, but does have an exact solution that can be found numerically [8].

The X-point is geometrically defined as the point where the product of the slope of the boundary approaching on either directions equal to -1; it is therefore a singular point. The matemathical form of the superellipse (Eq. 2.19) is characterized by the fact that the slopes of the boundary approach from either direction of the extremum points asimptotically to zero. Despite this property, the superellipse form can be used as a starting point to introduce the X-point without losing the possibility to control the shape of the boundary: the points defined by the superellipse can be used as a set of starting data points for a Bézier interpolating function, which allows to introduce the X-point. The use of the points of the superellipse rather than the experimental data points allows to generate families of boundary by varying, for each quadrant, the "freedom parameter" as described in Sect. 2.5.

3.2 Bézier curves

Bézier curves are named after their inventor, Dr. Pierre Bézier, an engineer with the Renault car company who set out in the early 1960s to develop a curve formulation for use in shape design that would be intuitive enough for designers and artists to use, without requiring a background in mathematics [11].

The Bézier curve is a parametric curve $\mathbf{P}(t)$, that is a polynomial function of the parameter t, and its grade depends on the number of points used to define the curve. These points are called *control points* and by connecting them in their natural order with straight segments, the

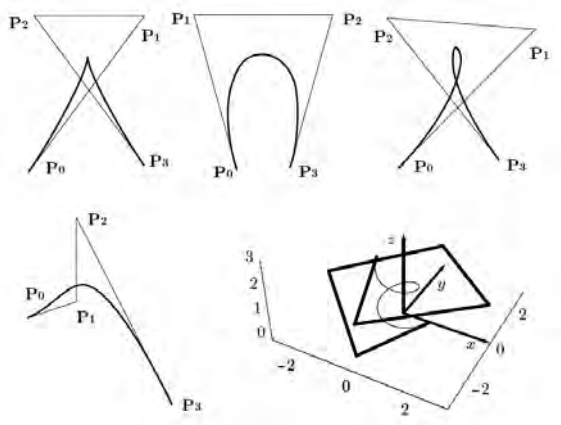

Figure 3.1: Four plane cubic and one cpace Bézier curves with their control points and polygons.

control polygon is defined. The Bé zier curve does not pass through all the control points but only through its first and last, as shown in Fig. 3.1. The curve is also tangent to the control polygon at those end points. Each point influences the direction of the curve by pulling it toward itself, and that influence is stronger when the curve gets nearer the point. The interior control points are in fact free to be moved, and that is what makes the Bé zier curve so easy to be edited, modified and reshaped. The curve can be derived with two different approaches, weighted sum and linear intepolation, which are identical [12].

3.2.1 Bernstein form of the Bézier curve: Bernstein polynomials

The first approach to the Bézier curve express its points as a weighted sum of the control points $\mathbf{P}_i$, $i = 0, 1, ...n$, each one multiplied by a different weight B_i. Since the result $\mathbf{P}(t)$ depends on the parameter t and the points are given by the user, it is the weights that must depend on t. The weight functions chosen by Bézier were derived by the Russian mathematician Sergei Natanovich Bernstein in 1912, as part of his work on approximation theory. They are known as Bernstein polynomials and have the following general form:

$$B_{n,i}(t) = \binom{n}{i} t^i (1-t)^{n-i} \tag{3.1}$$

where $\binom{n}{i} = \frac{n!}{i!(n-i)!}$. In calculating the curve is assumed that the quantity 0^0, which is normally undefined, equals 1.

It is now possible to define the Bézier curve as:

$$\mathbf{P(t)} = \sum_{i=0}^{n} \mathbf{P}_i B_{n,i}(t) \tag{3.2}$$

where $0 \leq t \leq 1$ and each control point, which is a pair of coordinate in two dimensional case, is multiplied by its weight which is in the range of $[0, 1]$. The weights described by Bernstein act as *blending functions* that blend the contributions of the different points (Fig. 3.2). The set of Bernstein polynomials of degree n form a basis for the space of polynomials of degree n or less [13]. It's easy to note that $n + 1$ control points are needed to obtain a degree n curve.

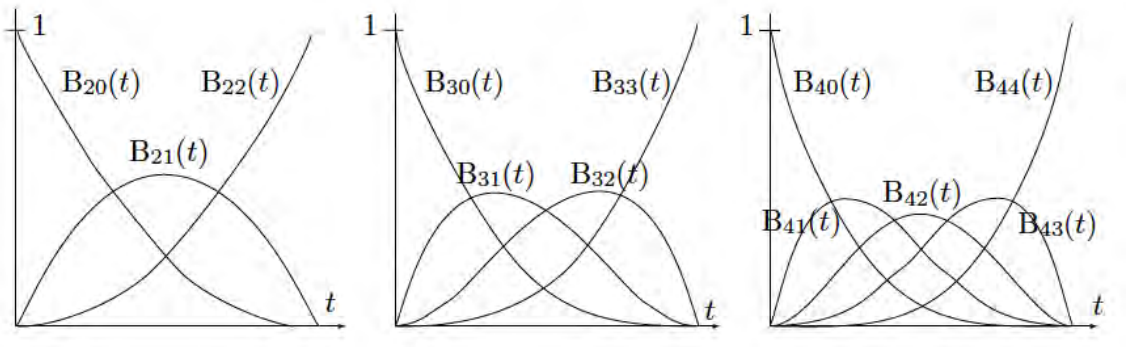

Figure 3.2: The Bernstein polynomials for degree n=2,3,4

3.2.2 Properties of Bézier curves

The following properties have been derived from Bézier requirements setted in the early 1960s when he started searching for such functions and are fondamental to understand the behaviour of these curves. Note that the definition shown in Eq. 3.2, using Bernstein polynomials as the weights, satisfies all these requirements [12].

1. The weights are barycentric which means that they add up to 1, which guarantee that the shape of the curve is indipendent of the coordinate system.

$$\sum_{i=0}^{n} B_{n,i}(t) = 1 \tag{3.3}$$

The property is easy to be demontrate by using Newton's binomial theorem:

$$(a+b)^n = \sum_{i=0}^{n} \binom{n}{i} a^i b^{n-i} \tag{3.4}$$

2. The curve passes through its first and last control points, $\mathbf{P}_0$ and $\mathbf{P}_n$, and it is always tangent to the control polygon at those endpoints. In fact it is possible to note that the first and the last Bernstein polynomial at the extremal values of the parameter t assumes:

$$\begin{aligned} B_{n,0}(0) &= \binom{n}{0} 0^0 (1-0)^{n-0} = 1 * 1 * 1^n = 1 \\ B_{n,n}(1) &= \binom{n}{n} 1^n (1-1)^{n-n} = 1 * 1 * 0^0 = 1 \end{aligned} \tag{3.5}$$

which implies:

$$\begin{aligned} \mathbf{P(0)} &= \sum_{i=0}^{n} \mathbf{P}_i B_{n,i}(0) = \mathbf{P}_0 B_{n,0}(0) = \mathbf{P}_0 \\ \mathbf{P(1)} &= \sum_{i=0}^{n} \mathbf{P}_i B_{n,i}(1) = \mathbf{P}_n B_{n,n}(1) = \mathbf{P}_n \end{aligned} \tag{3.6}$$

3. The curve is simmetry with respect to the numbering of the control points: if control points are numbered in decrescending order which means from $\mathbf{P}_n$ to 1, the same curve is obtained,

except from the fact that it proceeds from right (point $\mathbf{P}_0$) to left (point $\mathbf{P}_n$). Bernstein polynomials satisfy the following identity:

$$B_{n,j}(t) = B_{n,n-j}(1-t) \tag{3.7}$$

which brings to the simmetry property:

$$\sum_{j=0}^{n} \mathbf{P}_j B_{n,j}(t) = \sum_{j=0}^{n} \mathbf{P}_{n-j} B_{n,j}(1-t) \tag{3.8}$$

4. The k-th derivative of the curve at the first control point $\mathbf{P}_0$ depends only by the first point, $\mathbf{P}_0$, and its k neighbors control points. In particular, the tangent vector $\mathbf{P}^t(t)$, i.e. the first derivative, of the curve is a weighted sum of n terms where each Bernstein polynomial is the weight of a "control point" $\triangle\mathbf{P}_i$ which is the difference between the $i+1$th and the ith point:

$$\mathbf{P}^t(t) = \sum_{i=0}^{n} \mathbf{P}_i B_{n,i}^{'}(t) = n \sum_{i=0}^{n-1} \triangle\mathbf{P}_i B_{n-1,i}(t) B_{n,i}^{'}(t) \tag{3.9}$$

where:

$$\triangle\mathbf{P}_i = \mathbf{P}_{i+1} - \mathbf{P}_i \tag{3.10}$$

The two tangent vectors at the initial $\mathbf{P}^t(0)$ and final $\mathbf{P}^t(1)$ of the curve are easy to find by using Eq. 3.9 and they are used to reshape the curve since the initial tangent of the curve points in the direction from $\mathbf{P}_0$ to $\mathbf{P}_1$ as described in Eq. 3.11. Similarly for the final tangent of the curve (Eq. 3.12). It is clear that both of these tangents, initial and final, can be controlled by moving respectevely the point $\mathbf{P}_1$ and $\mathbf{P}_{n-1}$.

$$\mathbf{P}^t(0) = n(\mathbf{P}_1 - \mathbf{P}_0) \tag{3.11}$$

where:

$$\mathbf{P}^t(1) = n(\mathbf{P}_n - \mathbf{P}_{n-1}) \tag{3.12}$$

5. The "Global control property" means that moving one control point $\mathbf{P}_i$ modifies the entire curve such that most of the change occurs in the proximity of $\mathbf{P}_i$. This property is due to the fact that the weight functions $B_{n,i}(t)$ are non zero for all values except for $t = 0$ and $t = 1$. Therefore any change in control point $\mathbf{P}_i$ affects the contribution of the term $\mathbf{P}_i B_{n,i}(t)$ for all values of t. If a control point is moved in a direction, every point $\mathbf{P}(t_0)$ of the curve are moved in the same direction but by different amounts depending on t_0 [12].

6. *Convex hull* property which means that the Bézier curve always lie within the convex hull of their control points. The convex hull can be envisioned by pounding an imaginary nail into each control point, stretching an imaginary rubber band so that it surrounds the group of nails, and then collapsing that rubber band around the nails: the polygon created by that imaginary rubber band is the convex hull [11]. Fig. 3.3 illustrates.

7. Bézier curve is invariant under affine transformations (i.e. rotations, reflections, translations) but is not invariant under projections. Invariance under projections can be achieved by switching from the standard Bézier to the rational Bézier curve [12].

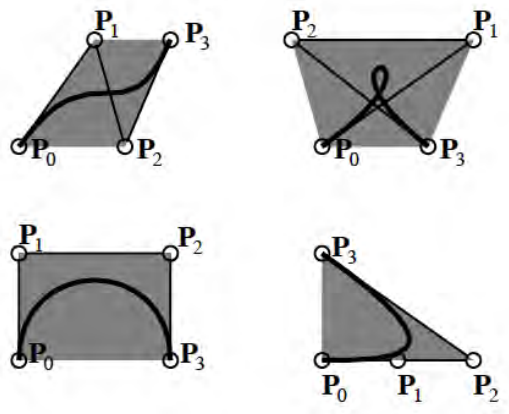

Figure 3.3: Convex hull property

3.2.3 Matrix formulation of Bézier curve

Bézier curves can be expressed in linear algebra form since the curve described by Eq. 3.2 is a polynomial of degree n. It results:

$$\mathbf{P}(t)^T = \begin{bmatrix} B_{n,0}(t)B_{n,1}(t)...B_{n,n}(t) \end{bmatrix} \begin{bmatrix} \mathbf{P}_0 \\ \mathbf{P}_1 \\ ... \\ \mathbf{P}_n \end{bmatrix} = B(t)P \tag{3.13}$$

where $B(t)$ is the *Bernstein matrix* and P is the *control points matrix*.

The Bernstein matrix is a generalized Vandermonde matrix which, for a vector $\mathbf{t} = [t_1, t_2, ..., t_m]^T$, $t_i \in [0, 1]$ and a given degree n, has the form:

$$B(t) = \begin{bmatrix} B_{n,0}(t_1) & B_{n,1}(t_1) & ... & B_{n,n}(t_1) \\ B_{n,0}(t_2) & B_{n,1}(t_2) & ... & B_{n,n}(t_2) \\ . & . & . & . \\ . & . & . & . \\ . & . & . & . \\ B_{n,0}(t_m) & B_{n,1}(t_m) & ... & B_{n,n}(t_m) \end{bmatrix} \tag{3.14}$$

therefore we see that for $t \in R^m$ and a given degree n we have $B(t) \in R^{m\times(n+1)}$ [13].

The control points matrix P is composed by the coordinates of the control points, which can be pairs or triplets of coordinates depending on the dimension of the problem space. In our bidimensional cases P contains the x and y coordinates:

$$P = \begin{bmatrix} P_{0,x} & P_{0,y} \\ P_{1,x} & P_{1,y} \\ . & . \\ . & . \\ . & . \\ P_{n,x} & P_{n,y} \end{bmatrix} \tag{3.15}$$

where $P_{0,x}$ and $P_{0,y}$ indicates respectevely the x component and y component of vector $\mathbf{P}_0$. Similarly it is possible to define the data points matrix Q:

$$Q = \begin{bmatrix} Q_{0,x} & Q_{0,y} \\ Q_{1,x} & Q_{1,y} \\ . & . \\ . & . \\ . & . \\ Q_{n,x} & Q_{n,y} \end{bmatrix} \tag{3.16}$$

3.3 Bézier interpolation of Divertor plasmas

In order to obtain the *extended analytical model* introduced in Sect. 3.1 it is necessary to resolve the main interpolation problem which consists in fitting an ordered set of superellipse data points with a closed Bézier curve in total least square sense, i.e. where the sum of the residuals in both horizontal and vertical directions is minimized, and to generate the X-point by imposing the X-point constraints. The problem is solved by using the matrix formulation of Bézier curves, introduced in Sect. 3.2.3 and a new *Block matrix representation.* The main problem will be split in two subproblems, which depend from each other.

3.3.1 Problem statement

The problem can be expressed in this terms: given an ordered set of m data points, which describes the superellipse characterization of the plasma boundary, $\mathbf{Q}_i$, $i = 0, 1, ..., m$, find a set of n control points $\mathbf{P}_i$, $i = 0, 1, ..., n$, and a vector t, $0 \leq t_i \leq 1$, $i = 0, 1, ..., m$, that minimize:

$$\|B(t)P - Q\|_F \tag{3.17}$$

and at the same time respect the *closed surface constraints* and the *X-point constraint*:

$$\begin{aligned} \mathbf{P}(0) &= \mathbf{P}_0 = \mathbf{Q}_0 \\ \mathbf{P}(1) &= \mathbf{P}_n = \mathbf{Q}_0 \end{aligned} \tag{3.18}$$

$$\mathbf{P}^t(1) = -\frac{1}{\mathbf{P}^t(0)} \tag{3.19}$$

In Eq. 3.17 there is $B(t)$,P, Q which are respectively the Bernstein matrix, the control points matrix and the data points matrix, which have been already introduced in Sect. 3.2.3, and $\| \quad \|_F$ that is called the *Frobenius norm* which for $X \in R^{m \times n}$ is given by:

$$\|X\|_F = (\sum_{i=1}^{m} \sum_{j=1}^{n} x_{i,j}^2)^{\frac{1}{2}} \tag{3.20}$$

The closed surface constraints expressed in Eq. 3.18 is used to obtain a closed Bézier curve which ends at the starting point that is the X-point of the plasma boundary. The X-point constraint in Eq. 3.19 is applied on the first derivative, i.e. tangent vector, at the final of the curve in order to obtain the geometry condition of X-point, which has been introduced in Sect. 3.1.

3.3.2 Reformulation of the problem

The problem can be stated as an *overdetermined constrained parametric non linear least square problem* characterized by $n-1$ unknown control points and m equations with m parametric unknowns values for the nodes vector $\mathbf{t}$. In order to minimize the residual with the respect of the constraints, the problem in Eq. 3.17 has been reformulate in an uncoupled form, by defining new block matrices which include the constraints defined in Eq. 3.18 and Eq. 3.19:

$$[M(t)] = \left[\begin{array}{cccc|cccc} B_{n,1}(t_2) & B_{n,2}(t_2) & \cdots & B_{n,n}(t_2) & 0 & 0 & \cdots & 0 \\ B_{n,1}(t_3) & B_{n,2}(t_3) & \cdots & B_{n,n}(t_3) & 0 & 0 & \cdots & 0 \\ \vdots & & \ddots & \vdots & 0 & 0 & \cdots & 0 \\ B_{n,1}(t_{m-1}) & B_{n,2}(t_{m-1}) & \cdots & B_{n,n}(t_{m-1} & 0 & 0 & \cdots & 0 \\ 0 & 0 & \cdots & 0 & B_{n,1}(t_2) & B_{n,2}(t_2) & \cdots & \\ 0 & 0 & \cdots & 0 & B_{n,1}(t_3) & B_{n,2}(t_3) & \cdots & \\ 0 & 0 & \cdots & 0 & \vdots & & \ddots & \vdots \\ 0 & 0 & \cdots & 0 & B_{n,1}(t_{m-1}) & B_{n,2}(t_{m-1}) & & \\ \hline \\ m_i & 0 & \cdots & 0 & -1 & 0 & \cdots & 0 \\ 0 & \cdots & 0 & -m_f & 0 & \cdots & 0 & 1 \end{array}\right] \tag{3.21}$$

where m_i and m_f are the slopes at the initial and final of the curve:

$$m_i = \frac{Q_{1,y} - Q_{0,y}}{Q_{1,x} - Q_{0,x}} \tag{3.22}$$

$$m_f = -\frac{1}{m_i} \tag{3.23}$$

$$[P] = \begin{bmatrix} P_{1,x} \\ P_{2,x} \\ \vdots \\ P_{n-1,x} \\ P_{1,y} \\ P_{2,y} \\ \vdots \\ P_{n-1,y} \end{bmatrix} \tag{3.24}$$

$$[Q] = \begin{bmatrix} Q_{1,x} \\ Q_{2,x} \\ \vdots \\ Q_{n-1,x} \\ Q_{1,y} \\ Q_{2,y} \\ \vdots \\ Q_{n-1,y} \end{bmatrix} \tag{3.25}$$

The X-point constraint is defined by Eq. 3.23 and it is included in the new blocking matrices $[M(t)]$ and $[Q(t)]$. The closed surface constraints are also included in this new formulation by modifying the elements of the known data points matrix $[Q(t)]$ by adding to it the known elements referred to the first and last point of the curve and by adding two new rows referred to the slope constraints imposed in matrix $[M(t)]$:

$$[Q] = \begin{bmatrix} Q_{1,x} \\ Q_{2,x} \\ \vdots \\ Q_{n,x} \\ Q_{1,y} \\ Q_{2,y} \\ \vdots \\ Q_{n,y} \\ m_i Q_{1,x} - Q_{1,y} \\ -m_f Q_{n,x} + Q_{n,y} \end{bmatrix} - \begin{bmatrix} B_{n,1}(t_2) \\ B_{n,1}(t_3) \\ \vdots \\ B_{n,1} \\ 0 \\ 0 \\ \vdots \\ 0 \end{bmatrix} Q_{1,x} - \begin{bmatrix} B_{n,n}(t_2) \\ B_{n,n}(t_3) \\ \vdots \\ B_{n,n}(t_{m-1}) \\ 0 \\ 0 \\ \vdots \\ 0 \end{bmatrix} Q_{n,x} - \begin{bmatrix} 0 \\ 0 \\ \vdots \\ 0 \\ B_{n,1}(t_2) \\ B_{n,1}(t_3) \\ \vdots \\ B_{n,1} \end{bmatrix} Q_{1,y} - \begin{bmatrix} 0 \\ 0 \\ \vdots \\ 0 \\ B_{n,1}(t_2) \\ B_{n,1}(t_3) \\ \vdots \\ B_{n,1} \end{bmatrix} Q_{n,y} \tag{3.26}$$

The residual can be expressed in terms of block matrices formulation as follows:

$$R = [M(t)]\,[P] - [Q] \tag{3.27}$$

Minimizing the Phrobenius norm of the residual is the same as minimizing the 2 norm of Eq. 3.27, which is called the uncoupled form of the residual. Since the non-linearity is localized to matrix $M(t)$, the main problem can be separated in two subproblems each one for each typology of unknown, P or $\mathbf{t}$. In other words, if the vector $\mathbf{t}$ is given than the first linear subproblem is obtained; if the matrix P is given than the second nonlinear subproblem is obtained.

The first subproblem is an overdetermined constrained linear least square problem for the matrix P: for a given vector $\mathbf{t}$, matrix P is separable from the minimizing residual equation (Eq. 3.17) and satisfies the:

$$P = M(t)^* Q \tag{3.28}$$

where $M(t)^*$ is the Moore-Penrose generalized inverse, i.e. pseudo-inverse, of matrix $M(t)$.

The second sub-problem is a non-linear least square problem for the vector $\mathbf{t}$, with a given P resulting from the solution of Eq. 3.28. Minimizing the residual in Eq. 3.17 determines the nearest Bézier curve points $\mathbf{P}(t_i)$ to their associated data points, for a particular control point matrix P. Since nodes and control points that minimize Eq. 3.17 also minimize the norm 2 of Eq. 3.27, it is possible to demonstrate, see [13], that this is equivalent to minimizing the objective function:

$$(P(t_1)_x - Q_{1,x})^2 + ... + (P(t_m)_x - Q_{m,x})^2 + (P(t_1)_y - Q_{1,y})^2 + ... + (P(t_m)_y - Q_{m,y})^2 \tag{3.29}$$

For a given matrix P, a change in node t_i only affects the point $\mathbf{P}(t_i)$ therefore the Eq. 3.29 can be split in m indipendent objective functions [13]:

$$(P(t_i)_x - Q_{i,x})^2 + (P(t_i)_y - Q_{i,y})^2 \tag{3.30}$$

Minimizing Eq. 3.30 is equivalent to determining the nearest point for data point $(Q_{i,x}, Q_{i,y})$. By doing this for each node, it is possible to determine each nearest point and minimize Eq. 3.17 for

a particular matrix P. So the second subproblem is to solve the nonlinear least squares problem for the vector $\mathbf{t}$ that it is equivalent to solving the nearest point problem. Minimizing Eq. 3.30 is equal to find the stationary point of:

$$g(t_i) = (P(t_i)_x - Q_{i,x})^2 + (P(t_i)_y - Q_{i,y})^2 \tag{3.31}$$

that becomes:

$$\frac{d}{dt_i} g(t_i) = 2(P(t_i)_x - Q_{i,x}) \frac{d}{dt_i} P(t_i)_x + 2(P(t_i)_y - Q_{i,y}) \frac{d}{dt_i} P(t_i)_y = 0 \tag{3.32}$$

Thus the necessary condition for minimizing Eq. 3.30 is found: the point $\mathbf{P}(t_i)$ which minimize Eq. 3.30 is perpendicular to the tangent vector at the same point [13].

To start the solution of the first subproblem, an initial set of nodes $\mathbf{t}$ and a the desired degree of the Bézier curve are required. Than the control points matrix $[P]$ is found and it represent the best answer possible given the initial set of nodes and the desired degree of the curve. Afterwards, matrix $[P]$ is used as initial set of control points data to solve the second subproblem, the nonlinear least square problem for t. It is clear that an initial set of nodes $\mathbf{t}$ must be produced to solve the least squares problem for control points $[P]$ and to start the entire solution procedure. This initial set of nodes can be found with several methods, see [13].

3.3.3 Solution procedure

As introduced in Sect. 3.3.2, the main problem can be split into two subproblems that can be solved separately by using each "sub-solution" as starting data for each solution procedure. The main algorithm is composed by four steps:

1. Determination of the initial set of nodes $\mathbf{t}$.
2. Resolution of the first subproblem, the overdetermined constrained linear least square problem for the control points $[P]_i$ and calculation of the residual.
3. Resolution of the nonlinear least square problem for the nearest points, with the given matrix $[P]_i$ calculated in the previous step. Gauss-Newthon method is used to solve the nonlinear least squares problem and to obtain the improved estimate nodes vector $\mathbf{t}_{i+1}$. For detailed discussion on Gauss-Newthon method, see [13].
4. Resolution of the overdetermined constrained linear least square problem for the matrix $[P]_{i+1}$ and calculation of the new residual. Return to step two and repeat steps two and three until the stopping criteria over the residual is reached.

3.3.4 Results

As introduced in Sect. 3.1, the Bézier interpolating function allows to introduce the X-point without losing the possibility to control the shape of the boundary and to generate families of boundary by varying the "squareness" of the limited model described in Sect. 2.5. The Bézier interpolating function has been applied to a typical diverted configuration as shown in Fig. 3.4 where the blue dotted line is the experimental data set of plasma boundary and the black continuous line is the interpolated plasma boundary. A new plasma boundary has been obtained by imponing the squareness of the two upper quadrant $\xi_I = 0.45$ and $\xi_{II} = 0.22$, as shown in Fig. 3.5.

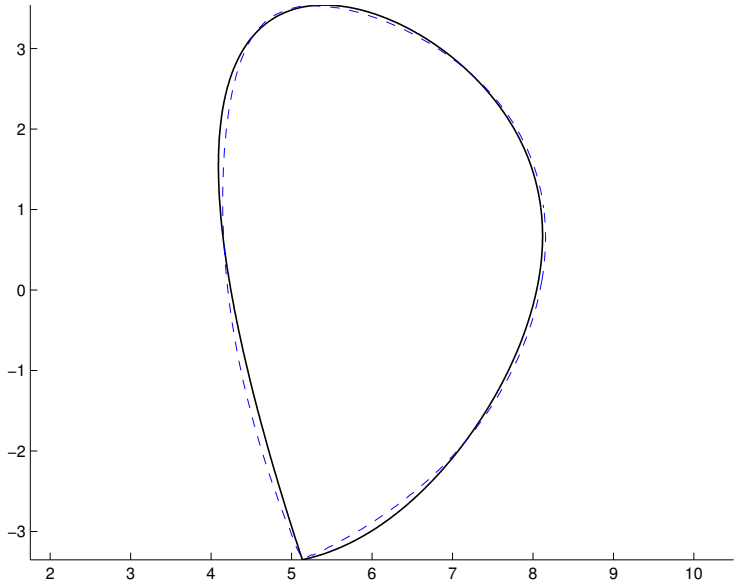

Figure 3.4: Bézier interpolation of a diverted plasma boundary

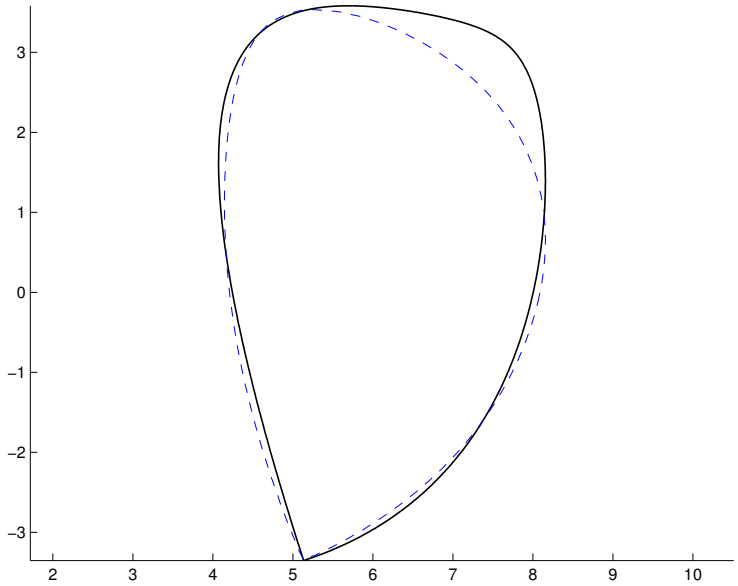

Figure 3.5: Bézier interpolation of a diverted plasma boundary

Chapter 4

Mesh

4.1 Introduction to mesh generation

The analytical models introduced in Chap. 2 and Chap. 3 are the starting point for the important process of discretized representation of the spatial physical domain of the plasma region and the consequently numerical computations of the plasma equilibrium problem solution. This process of discretizing representation, also known as *mesh generation*, can be indipendently considered, in sub-domain methods (e.g. Finite Element Method), to the problem solution procedure: they are two distinct problems and therefore mesh data can conveniently be stored for reuse several times.

The problem is to generate an unstructured mesh for a geometry specified by implicit functions. The alghorithm adopted is the *DistMesh* [14], which is a simple algorithm that combines a physical principle of force equilibrium in a truss structure with a mathematical representation of the geometry using *signed distance function*, which is negative inside the region, zero at the boundary and positive outside the region. It is important to specify that the signed distance function for rectangular geometries avoids square roots from distances to corner points, and no meshpoints end up in these four regions when the corner points are fixed: for the rectangle it is the minimum distance to the four boundary lines (each extended to infinity and with the desired negative sign inside the rectangle) [14]. A part from being simple, the *DistMesh* algorithm generates uniform or refined meshes of high quality. For more informations about *DistMesh* see [14].

The geometry region is basically implicitly described by its distance function to the boundary so it brings to the problem of computing distance functions for the Limited boundary geometry and the Diverted boundary geometry. These distances can't be the same because of the different nature of the two characterizing model: as introduced in previous Chap. 2 and Chap. 3, the Limited boundary is described by an analytical functional form while the Diverted boundary by an interpolating function.

4.2 Mesh for Limiter plasma boundaries

Despite it is easy to create distance functions for simple geometries, it is not for complex geometries like the Limiter plasma boundary, which is a composition of superellipses, and the Diverted plasma boundary which is the result of an interpolation. Anyway it is possible to combine geometries defined by distance functions by using the boolean operations of *union*, *difference* and *intersection* which are described in Tab. 4.1.

Boolean operation	function
Union	$d_{A\cup B}(x,y) = min(d_A(x,y), d_B(x,y)$
Difference	$d_{A\setminus B}(x,y) = max(d_A(x,y), -d_B(x,y)$
Intersection	$d_{A\cap B}(x,y) = max(d_A(x,y), d_B(x,y)$

Table 4.1: Boolean distance function operation for two regions A and B

In order to mesh a Limiter plasma boundary, it is necessary to define a distance function for implicit expressions $f(x,y)$ where the boundary is the zero level set of the given implicit function and the gradient of this function is equal to 1. For each node $\mathbf{p}_0 = (x_0, y_0)$, the closest point $\mathbf{P}$ is needed on that zero level set - which means that $f(\mathbf{P}) = 0$ and $\mathbf{P} - \mathbf{p}_0$ is parallel to the gradient (f_x, f_y) at $\mathbf{P}$ [14].

$$\mathbf{L}(\mathbf{P}) = \begin{bmatrix} f(x,y) \\ (x-x_0)f_y - (y-y_0)f_x \end{bmatrix} = 0 \tag{4.1}$$

Eq. 4.1 is solved for each column vector $\mathbf{P} = (x,y)$ by using the damped Newton's method with $\mathbf{p}_0 = (x_0, y_0)$ as initial guess [14].

$$\mathbf{J}(\mathbf{P}) = \frac{\partial \mathbf{L}}{\partial \mathbf{P}} = \begin{bmatrix} f(_x & f_y + (x-x_0)f_{xy} - (y-y_0)f_{xx} \\ f_y & -f_x - (y-y_0)f_{xy} + (x-x_0)f_{yy} \end{bmatrix}^T \tag{4.2}$$

$$\mathbf{p}_{k+1} = \mathbf{p}_k - \alpha \mathbf{J}^{-1}(\mathbf{p}_k)\mathbf{L}(\mathbf{p}_k) \tag{4.3}$$

The method is described in Eq. 4.2 and Eq. 4.3 where α is the damping factor which can be set to 1 as default but it can be reduced adaptively for convergence. The signed distance function from (x_0, y_0) to $\mathbf{P} = (x,y)$ on the zero level set of $f(x,y)$ is [14]:

$$d(\mathbf{p}_0) = sign(f(x_0, y_0))\sqrt{(x-x_0)^2 + (y-y_0)^2} \tag{4.4}$$

This implicit distance function has been applied and generalized to a superellipse equation with centre coordinates (x_c, y_c), bringing to an exact representation of the portion of the geometry. The complete Limiter plasma boundary is obtained by applying the boolean operations for each of the four portions of superellipses of each quadrant. As the element size gets smaller, the mesh automatically fits to the exact boundary, without any need to refine the representation. The signed distance function can also be used in the definition of the (relative) desired edge length function $h(x,y)$ [14]. A uniform mesh, charcterized by a uniform distribution of the edge length function $h(x,y)$, is represented in Fig. 4.1. A non-uniform mesh with a higher resolution near the boundary is defined by using a varying size functions $h(x,y)$ which elements increases with the distances from the boundary, see Fig. 4.2.

The boundaries generated in Sect. 2.6 and shown in Fig. 2.11, Fig. 2.12 has been meshed by using a uniform edge length function as shown in Fig. 4.3 and Fig. 4.4.

4.3 Mesh for Divertor plasma boundaries

The Diverted plasma boundary has been meshed by using a different approach: as the boundary is the results of the Bézier interpolating function described in Sect. 3.3, the implicit expression approach used for the Limiter plasma boundaries results complicated and computational expens-

ive due to the fact that the Bézier curve is a parametric curve. The interpolation is treated as a given polygon specified by the ordered set of the Bézier curve points resulted from the interpolating process. The distance function is so determined with respect of the polygon by using the $MATALAB$'s *inpolygon* function to determine the sign. The only fixed point for the mesh generation is the X-point, which is also the only real data point that is forced to be fitted by the Bézier interpolating function, as already seen in Sect. 3.3. The mesh can again be uniform (Fig. 4.5) or non-uniform with different edge length functions $h(x, y)$ as shown in Fig. 4.6, Fig. 4.7 and Fig. 4.8. These functions are defined by using the signed distance function as introduced in Sect. 4.2.

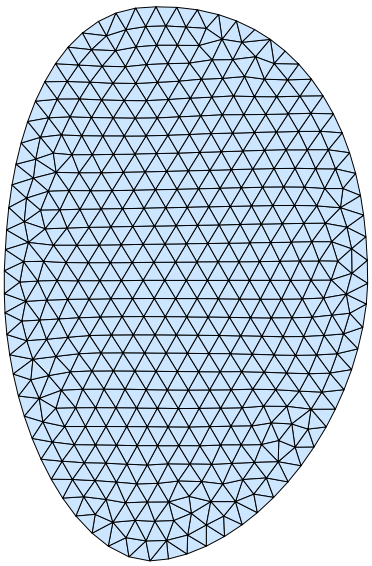

Figure 4.1: Uniform mesh for Limiter plasma Boundary

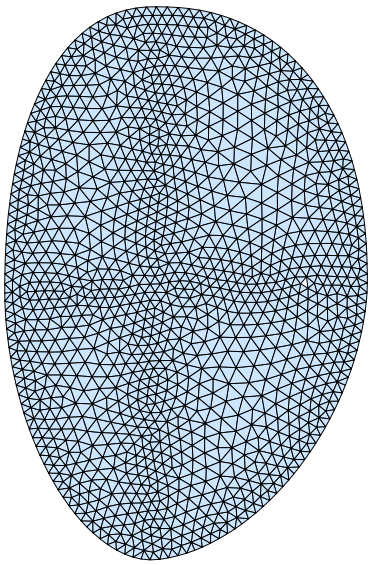

Figure 4.2: Non-uniform mesh for Limiter plasma Boundary

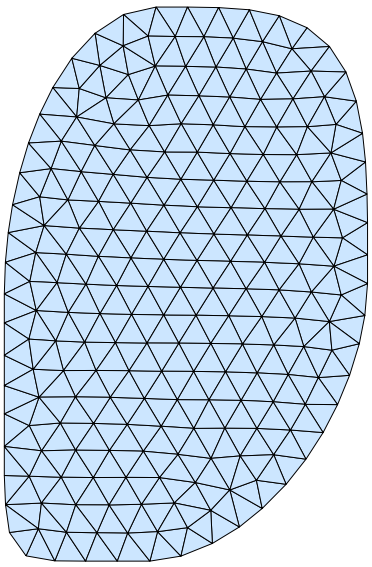

Figure 4.3: Uniform mesh for generated plasma boundary with $\xi_I = 0.45$ and $\xi_{III} = 0.78$

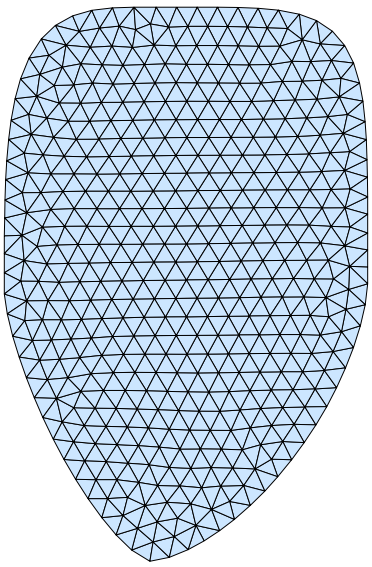

Figure 4.4: Uniform mesh for generated plasma boundary with $\xi_I = 0.58$, $\xi_{II} = 0.42$, $\xi_{III} = -0.35$ and $\xi_{IV} = -0.22$

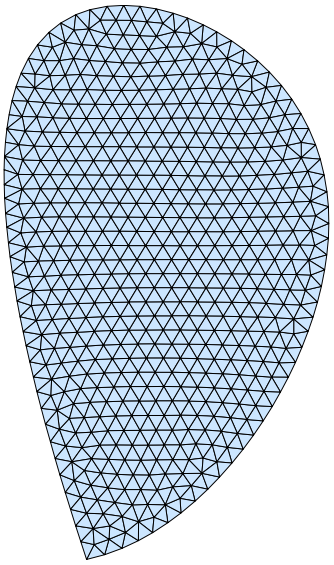

Figure 4.5: Uniform mesh for Diverted plasma Boundary

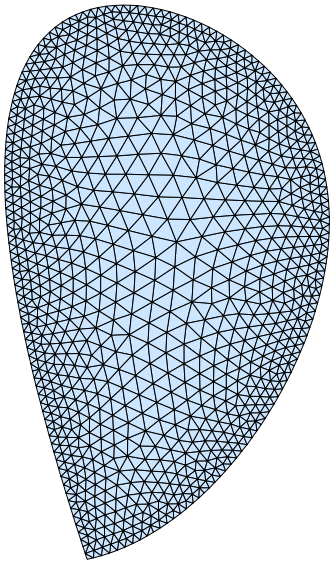

Figure 4.6: Non-uniform mesh for Diverted plasma Boundary

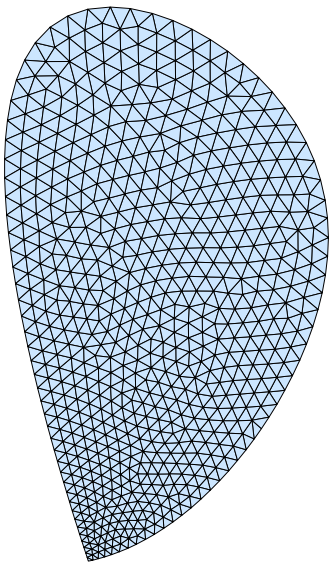

Figure 4.7: Non-uniform X-point refined mesh for Diverted plasma Boundary

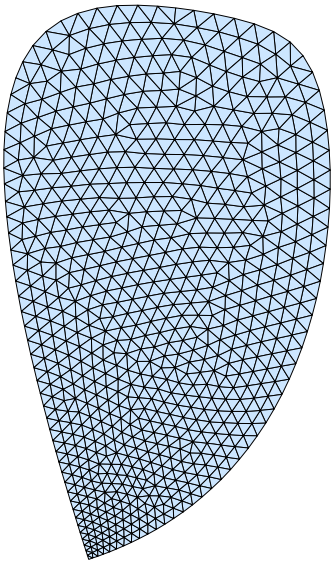

Figure 4.8: Non-uniform X-point refined mesh for Bézier interpolated plasma Boundary with $\xi_I = 0.45$ and $\xi_{II} = 0.22$

Chapter 5

Numerical models for fusion magnetic field sources

5.1 Introduction

Closed magnetic confinement systems have helical magnetic field lines which are due to both simultaneous contributions of internal sources, i.e the plasma itself drive a current that produces magnetic fields, and external sources, i.e the magnet systems. All the main important magnetic confinement machines (like Tokamaks, RFP,...) comprises three basic magnetic systems: the toroidal field (TF) coils, which produce the large toroidal magnetic field, the central solenoid (CS), i.e. ohmic transformer or inner poloidal field coil, which induces the toroidal plasma current required for equilibrium ohmic heating, the poloidal field (PF) coils which ensure toroidal force balance and produce a non-circular cross section to improve MHD stability and control plasma shape. ITER magnet system comprises all of these coils, as shown in Fig. 5.1. In more detail, the poloidal field coil system consists of six horizontal coils placed outside the toroidal magnet structure and each coil is composed by a different number of turns; in addition there are two in-vessel coils each one made by 4 turns. The central solenoid system consists in six coils each one constitued by 553 turns.

The starting point for a computational numerical analysis of the plasma equilibrium is the numerical representation of the magnetic field sources of the reactor as the ITER magnet system. In other words it is necessary to obtain an efficient numerical model that can compute the magnetic fields produced by the magnetic field sources. This model can be achieved by using different representation of the magnet systems geometry, each one based on different approximations and numerical integration methods.

The law that allows to compute the resultant magnetic field $\mathbf{B}$ at a position P_0 of the space generated by a current $\mathbf{J}$ in the point of space P is the Biot-Savart law which in presence of uniform magnetic permeability μ_0 and by introducing the magnetic vector potential $\mathbf{A}$, brings to the following esxpressions:

$$\mathbf{A} = \frac{\mu_0}{4\pi} \int_\tau \frac{\mathbf{J}}{d} d\tau \tag{5.1}$$

$$\mathbf{B} = \frac{\mu_0}{4\pi} \int_\tau \frac{\mathbf{J} \times \mathbf{d}}{d^3} d\tau \tag{5.2}$$

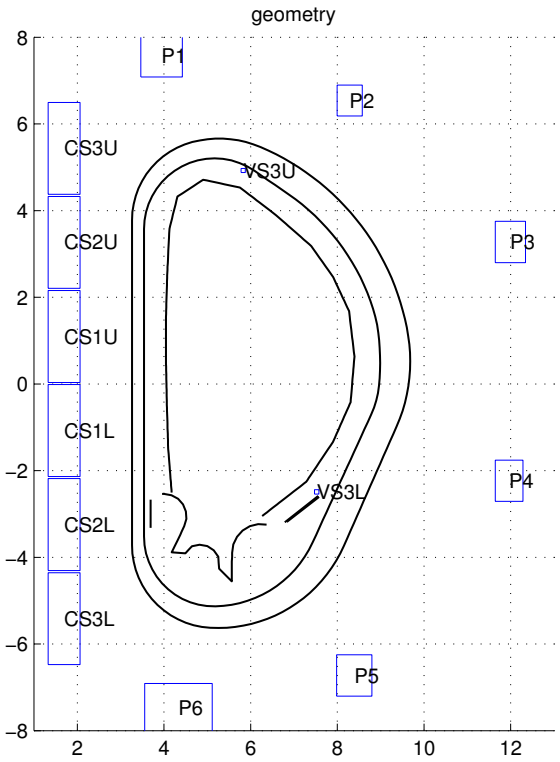

Figure 5.1: ITER geometry

where τ is the volume of space where the current $\mathbf{J}$ is present and $d = \|\mathbf{d}\|_F$ with $\mathbf{d} = \overline{P_0 P}$. These integrals are usually applied around a close curve and more in general, an analytical solution exists for monodimensional or bidimensional sources. For some types of source geometry and current density distribution, a mixed analytical-numerical approach is used by numerically integrating the analytical contribution, i.e. the monodimensional or bidimensional contribution, in order to obtain the volume integration of the Eq. 5.1 and Eq. 5.2.

5.2 Axisymmetric current density distribution sources

The ITER magnet systems can be stated as a set of axisymmetric current density distribution of sources. It is assumed a cylindrical coordinate system (r, ϑ, z), a current density $\mathbf{J} = J_\vartheta(r_0, z_0)\mathbf{u}_\vartheta$ which is always tangent to ϑ coordinate lines and a calculation point P. The toroidal volume where the current density is present is indicated with τ and the toroidal corss-section with S. These assumptions are shown in Fig. 5.2.

In these conditions Eq. 5.1 and Eq. 5.2 can be integrated along ϑ:

$$\mathbf{A} = \mathbf{A}_\vartheta \mathbf{u}_\vartheta = \frac{\mu_0}{4\pi} G_A \int_S J(r_0, z_0) dS \tag{5.3}$$

$$\mathbf{B} = B_r(r, z)\mathbf{u}_r + B_z(r, z)\mathbf{u}_z = \frac{\mu_0}{4\pi} G_B \int_S J(r_0, z_0) dS \tag{5.4}$$

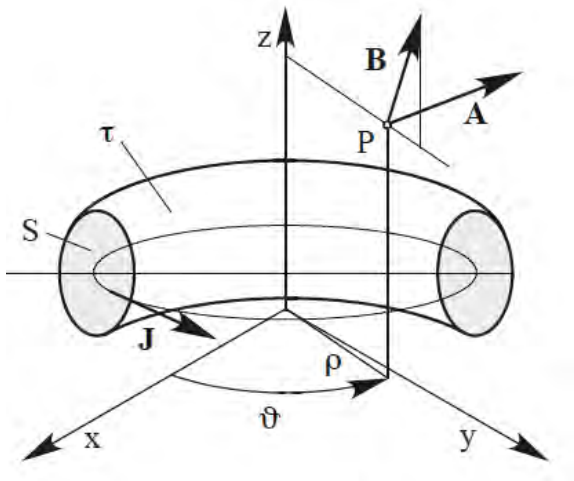

Figure 5.2: Cylindrical coordinate system

$$G_A = \int_0^{2\pi} r_0 \frac{\mathbf{u}_\vartheta}{d} d\vartheta \tag{5.5}$$

$$G_B = \int_0^{2\pi} r_0 \frac{\mathbf{u}_\vartheta \times \mathbf{d}}{d} d\vartheta \tag{5.6}$$

where $P_0 = (r_0, z_0)$ is the integration point in the cross-section and G_A and G_B are respectevely the *Green functions* for the magnetic vector potential and the magnetic induction expressed by Eq. 5.5 and Eq. 5.6 in cylindrical coordinates.

The Green funtions indicates the type of approximation assumed to represent the source of the magnetic field. Poloidal field coils and central solenoid coils can represented by several approximated model and for each one the corresponding Green functions can be calculated. It will be described in the next sections for the main typical cases. Since numerical methods are very sensitive in its efficiency, several approaches are used and compared to represent the magnet systems and to obtain the best procedure to compute the magnetic fields.

5.2.1 Thin circular loop

The thin circular loop model is the most simple and approximated representation of a magnet fusion source since the loop cross-section size is negligible. The model is shown in Fig. 5.3 where r_1 is the radius, I is the current located at $z = z_1$.

The computation of the magnetic vector potential and the magnetic induction due to a thin circular loop of current is defined by two different set of expressions, each one defined by the position of the calculation point. This position can be defined by introducing these parameters $\varrho_1 = \frac{r}{r_1}$, $\zeta_1 = \frac{z - z_1}{r_1}$ and $k_1 = 2\sqrt{\varrho_1}/\sqrt{(\varrho_1 + 1)^2 + \zeta_1^2}$. There are now three clear cases: the first one is when the calculation point is in a generic position of the space,i.e. $0 < k_1 < 1$, the second one is when the calculation point is along the loop axis,i.e. $\varrho_1 = 0$ and the third one is when the calculating point belongs to the loop.

The following expressions are valid for the first case:

$$A_\vartheta = \frac{\mu_0 I}{4\pi} G_A = \frac{\mu_0 I}{\pi k_1 \sqrt{\varrho_1}} [(K(k_1) - E(k_1)) - \frac{k_1^2}{2} E(k_1)] \tag{5.7}$$

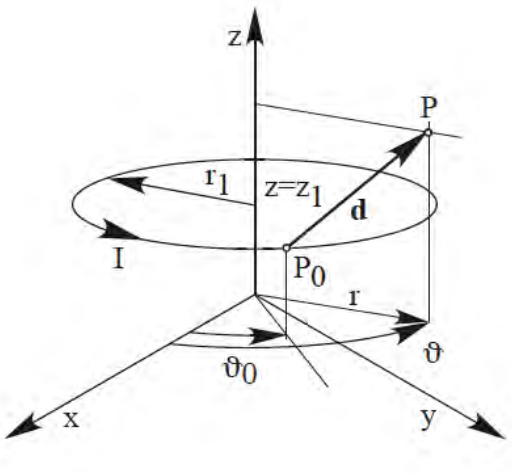

Figure 5.3: Thin circular loop model

$$B_r = \frac{\mu_0 I}{4\pi} G_{B_r} = \frac{\mu_0 I k_1 \zeta_1}{4\pi r_1 \varrho_1 \sqrt{\varrho_1}} [-(K(k_1) - E(k_1)) + \frac{k_1^2}{2(1-k_1^2)} E(k_1)] \tag{5.8}$$

$$B_z = \frac{\mu_0 I}{4\pi} G_{B_z} = \frac{\mu_0 I k_1}{4\pi r_1 \sqrt{\varrho_1}} [(K(k_1) - E(k_1)) + \frac{(1-\varrho_1)}{\varrho_1} \frac{k_1^2}{2(1-k_1^2)} E(k_1)] \tag{5.9}$$

where $K(k1)$ and $E(k1)$ are the complete elliptic integral of the first and second kind:

$$K(k_1) = \int_0^{\pi/2} \frac{d\varphi}{\sqrt{1 - k_1^2 \sin^2(\varphi)}} \tag{5.10}$$

$$E(k_1) = \int_0^{\pi/2} \sqrt{1 - k_1^2 \sin^2(\varphi)} d\varphi \tag{5.11}$$

In the second case, in which the point of calculation is along the loop axis and so $k_1 = 0$ as a consequence of $\varrho_1 = 0$, i.e. $r = 0$, the Eq. 5.7-Eq. 5.9 are no longer valid. In order to get a smooth solution for the magnetic induction , the magnetic vector potential is set to zero for all the axis points, $A_\vartheta(0, z) = 0$ and the magnetic induction components are straightforwardly computed as follows:

$$B_r(0, z) = 0 \tag{5.12}$$

$$B_z(0, z) = \frac{\mu_0 I}{4 r_1 \sqrt{\zeta_1^2 + 1}} \tag{5.13}$$

The last case is when the calculation point P belongs to the loop, i.e. $k_1 \to 1$ when $\varrho \to 0$ and $\zeta \to 0$: in this case the magnetic vector potential diverges logarithmically and the magnetic field diverges too as $1/(r_1 \sqrt{(\varrho_1 + 1)^2 + \zeta_1^2})$.

5.2.2 Thin circular solenoid

The thin circular solenoid model allows an analytical expression of vector potential and magnetic induction by integrating Eq. 5.7 along the z coordinate and therefore deriving magnetic induction by $\mathbf{B} = \nabla \times \mathbf{A}$. The model is characterized by a thin circular solenoid with current I, radius r_1 and lower and upper edges respectevely at coordinates z_1 and z_2 as shown in Fig. 5.4. As described in Sect. 5.2.1, the procedure to compute the fields changes with the position of the calculating

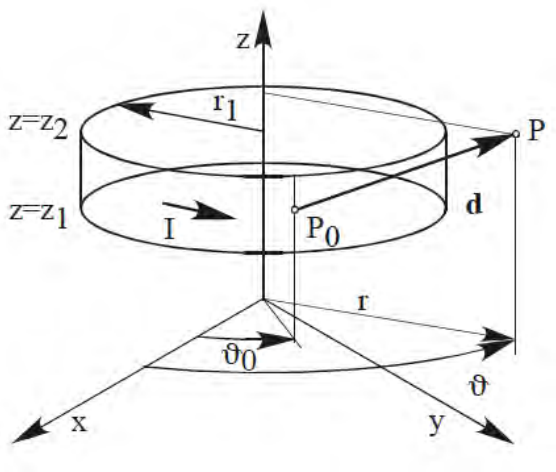

Figure 5.4: Thin circular solenoid model

points.

The following expressions, applicable for $0 < k1 < 1$ and $n < 1$, can be obtained:

$$A_\vartheta = \frac{\mu_0 J r_1}{2\pi\sqrt{\varrho_1}} \sum_{k=1}^{2} (-1)^k \zeta_k [k_k (1 - \frac{1}{k^2})(\Pi(n^2, k_k) - K(k_k)) + \frac{1}{k_k}(K(k_k) - E(k_k))] \tag{5.14}$$

$$B_r = \frac{\mu_0 J}{\pi\sqrt{\varrho_1}} \sum_{k=1}^{2} (-1)^k \frac{1}{k_k} [(1 - \frac{k_k^2}{2})((K(k_k) - E(k_k))] \tag{5.15}$$

$$B_z = \frac{\mu_0 J}{4\pi\sqrt{\varrho_1}} \sum_{k=1}^{2} (-1)^k \zeta_k k_k [-\frac{\varrho_1 - 1}{\varrho_1 + 1}\Pi(n^2, k_k) + K(k_k))] \tag{5.16}$$

where $J = I/(z_2 - z_1)$ is the superficial current density, $\zeta_k = (z_k - z)/r_1$, $k_k = 2\sqrt{\varrho_1}/\sqrt{(\varrho_1 + 1)^2 + \zeta_k^2}$ is the complete elliptic parameter, $n = 2\sqrt{\varrho_1}/(\varrho_1 + 1)$ is the complete integral charachteristic. $\Pi(n^2, k_k)$ is the complete elliptic integral of third kind:

$$\Pi(n^2, k_k) = \int_0^{\pi/2} \frac{d\varphi}{(1 - n^2 \sin^2 \varphi)\sqrt{1 - k_k \sin^2 \varphi}} \tag{5.17}$$

The second case is when $\zeta_k \to 0$ and $\varrho_1 \to 1$ therefore $k_k \to 1$, i.e. the calcultaion point belongs to one of the two solenoid circular eges: in this case the vector potential diverges logarithmically and the magnetic field diverges with a larger infinity order.

The third significally case is when $\varrho = 0$ then both $k_k = 0$ and $n = 0$, i.e. the calculation point belongs to the solenoid axis: in this case, the following expressions can be used:

$$A_{\vartheta\vartheta}(0, z) = 0 \tag{5.18}$$

$$B_r(0, z) = 0 \tag{5.19}$$

$$B_z(0, z) = \frac{\mu_0 J}{2} \sum_{k=1}^{2} (-1)^k \frac{\zeta_k}{\sqrt{\zeta_k^2 + 1}} \tag{5.20}$$

The last case is when the point is located at the same radius of the solenoid, i.e.$\varrho_1 = 1$ therefore

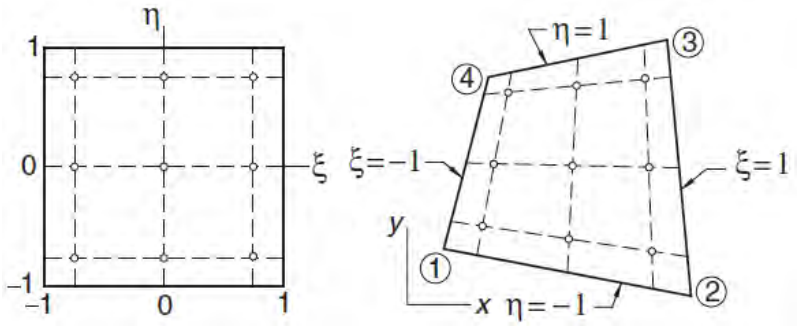

Figure 5.5: Standard rectangle and generic quadrilateral

$n = 1$: in this case, provided that $0 < k_k < 1$, a removable singularity is present and the expressions are:

$$A_{\vartheta\vartheta}(r_1, z) = \frac{\mu_0 J}{\pi} \sum_{k=1}^{2} (-1)^k \frac{\zeta_k}{k_k} [K(k_k) - E(k_k)] \tag{5.21}$$

$$B_r(r_1, z) = \frac{\mu_0 J}{\pi} \sum_{k=1}^{2} (-1)^k \frac{1}{k_k} [(1 - \frac{k_k^2}{2}) K(k_k) - E(k_k)] \tag{5.22}$$

$$B_z(r_1, z) = \frac{\mu_0 J}{4\pi} \sum_{k=1}^{2} (-1)^k k_k K(k_k) \tag{5.23}$$

5.3 Thick circular solenoid

The magnet systems are stranded coils (circular solenoids with rectangular cross section). In order to compute the magnetic fields produced by each coil it is necessary a numerical model to describe these sources. Two different methods has been implemented and compared: both of them use the Gauss-Legendre quadrature integration method but with different approaches and results.

The first method is the straightforward application of the Gauss quadrature integration method over a quadrilateral element. Multiple integrals like, such area integrals $\int\int_A f(x, y) dxdy$, can be evaluated by computing each integral in turn by Gauss-Legendre quadrature using n nodes in each coordinate direction, which is called the *integration order*. The computations are straightforward if the region of integration has a simple geometric shape, such as quadrilateral. For more informations about Gauss-Legendre quadrature method see reference [15]. Each coil is therefore modelled by a Gauss quadrature integration over two coordinates, r and z, since the problem is analyzed in two dimensions. Coils cross-sections are mapped into the standard rectangle by using coordinates transformations, $r = r(\xi, \eta)$ and $z = z(\xi, \eta)$, as shown in Fig. 5.5. It is possible to write the Gauss-Legendre quadrature over a quadrilateral region:

$$I = \sum_{i=1}^{n} \sum_{j=1}^{n} A_i A_j f[x(\xi_i, \eta_j), y(\xi_i, \eta_j)] \mid J(\xi_i, \eta_j) \mid \tag{5.24}$$

where the weights A_i and A_j are known for Gauss-Legendre polynomials and $\mid J(\xi_i, \eta_j) \mid$ is the determinant of the Jacobian matrix which is needed to map the quadrilateral into the standard rectangle without distorce its area, i.e. $dxdy = \mid J(\xi_i, \eta_j) \mid d\xi d\eta$. It is clear that the accuracy of the numerical representation of the coil depends on the order of the integration, i.e. the number of points for each direction n and m which are usually chosen as the same.

The second method to model a thick coil is an extension of the thin circular solenoid, introduced in Sect. 5.2.2. The general idea of the method is to provide a fast and precise computation of the fields generated by any limited spacial size source represented as the integration of a set of subdomains that have elementary geometry. The simplest cases seen in Sect. 5.2.2 and Sect. 5.2.1 can be used to represent more complex geometries in all dimensional cases. The main domain can be considered as generated by an infinite set of lower-dimension subdomains, an infinite set of circular loops or thin solenoids or a finite set of adjacent subdomains that have elementary geometry. In order to obtain a bidimensional representation of the thick coils, a fourth order Gauss quadrature integration of a thin circular solenoid over only one of the two directions, r or z depending on the definition of the thin solenoid, has been implemented.

5.4 Numerical results

The different models introduced in the previous sections represent, with different approximations, the magnet systems of ITER. Each one of these models has been tested with a specific procedure which depends on the type of the represented coils: the magnetic fluxes have been computed, for each model, along a "reference line" usefull to determine the behaviour of the magnetic flux with respect of the calculation points. The models has also been compared by a standard numerical approach in order to identify the most appropriate model in terms of best numerically results as efficiency and accuracy. This model will be used as reference model for the representation of magnetic sources in the solution of the plasma equilibrium problem.

The computation of the magnetic flux has been also repeated along a grid of points covering all the space of the machine, both near the coils space and the plasma region, in order to obtain the constant flux contours. The plasma current contribution to the fluxes has been calculated by modelling the plasma as a finite union of thin circular loops. Plasma and coils contributions to the magnetic flux has been represented separately and then together by adding one to the other.

5.4.1 Numerical analysis of the magnetic field sources

In order to compare the different models in terms of computated magnetic fluxes, it is necessary to introduce the percent relative error:

$$\epsilon = \frac{\psi - \psi_{ref}}{\psi_{ref}} 100 \tag{5.25}$$

where ψ is the computed flux by using a model and ψ_{ref} is the reference flux, assumed to be the flux computed by using the thick solenoid model. It is important to say that the error is calculated for each flux value computed in each point of the reference line, i.e. the definition in Eq. 5.25 can be extended by substituiting the single scalar flux quantities with a scalar vector quantities. The reference line is a rectilinear segment that covers the space in which the typical behaviour of the computed variables is "theoretically" known and will be numerically verified.

The lowest poloidal field coil, which is the one labelled as $P6$ in Fig. 5.6, is considered and all the considerations and procedures adopted for it can be extended to the central solenoid coils or the entire magnet system, i.e. central solenoid and poloidal field coils. The reference is therefore assumed to be a vertical line starting from the poloidal field coil $P6$ and finishing to the intersections with the r axis as shown in Fig. 5.6: in other words the r coordinate is fixed and constant while

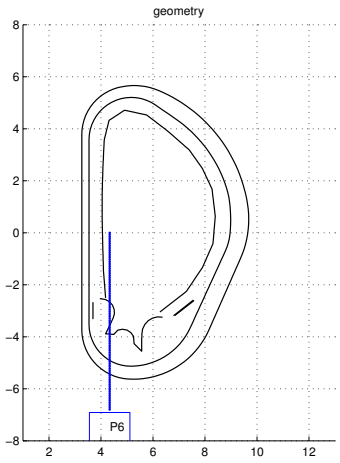

Figure 5.6: Reference line P6 case

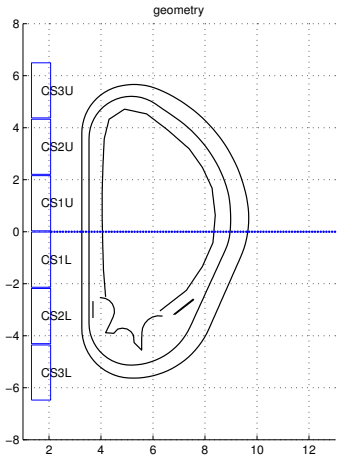

Figure 5.7: Reference line central solenoid case

the z coordinate is varying. Every point of the reference line can be viewed as the position for a magnetic flux sensor, ordered by integer values from the bottom (the number 1) up to the top (number 150), and along this line the flux is expected to decrease by moving away from the centre of the coil. In order to find the reference model it is interesting to see the different results obtained by using different coil models as shown in Fig. 5.8: the thick solenoid model is the most accurate despite the thin circular loop which is the less accurate one. The fourth order Gauss integration model's andament is so close to the thick coil curve that it is indistinguible in Fig. 5.8 and Fig. 5.9. Same considerations can be done for the central solenoid by assuming an horizontal reference line despite a vertical one, as shown in Fig. 5.7 and Fig. 5.9, and for both the magnet systems.

An important notice can be introduced by watching the residuals between the magnetic flux computed by every model and the magnetic flux computed by the thick solenoid model: in all the cases the residual is maximum at the nearest point to the coil while it decreases by moving away from the source. This is due to the fact that the numerical representation affects the results in the proximity of the source while at large distances the field is almost the same for every adopted model to represent the source. The relative percent error has been computed for all the models

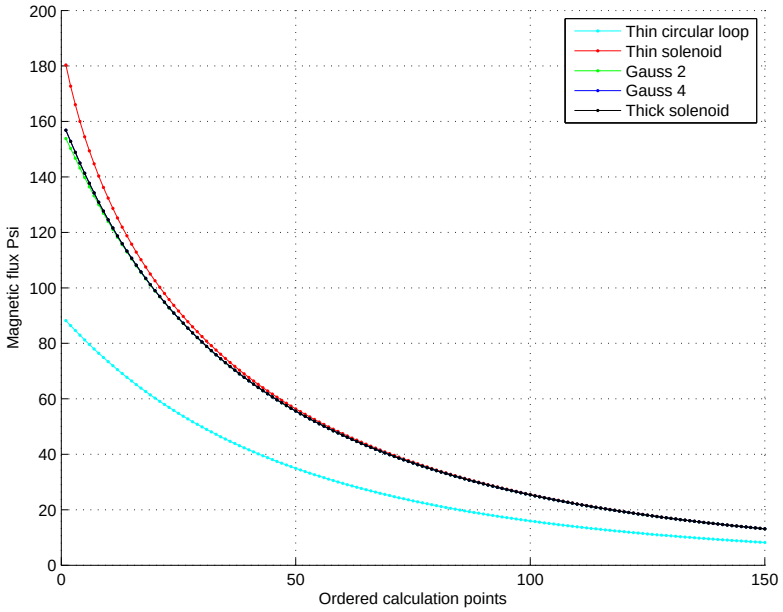

Figure 5.8: Flux PF

and plotted over the ordered points of calculation as shown in Fig. 5.10. As already said, all the numerical methods tend to be the same as the distance from the source is growing: this behaviour is notable in the relative percent error diagram which tends to zero for long distances. A similar diagram but relative to the central solenoid case is shown in Fig. 5.11.

5.4.2 Numerical analysis of the Gauss-Legendre quadrature integration model

An interesting case to analyze in terms of accuracy is the Gauss-Legendre quadrature integration model by varying the order of the integration over the two coordinates. The behaviour of the computed magnetic flux with respect of the calculation points for the central solenoid and the poloidal $P6$ coil are shown respectevely in Fig. 5.13 and Fig. 5.12. Assuming the thick coil model as reference, it is possible to define the relative percent errors for each order of integration and plot its andaments with respect of the ordered calculation points. Those andaments are shown in Fig. 5.15 and Fig. 5.14 respecively for the poloidal coil $P6$ and the central solenoid case. The integration is more accurate for order of integrations near the fourth, which is the same order used in the one dimension integration of the thick coil model so the accuracy of the integration increase with the order of integration since the fourth order is reached as shown in Fig. 5.16 and Fig. 5.17. As already seen, each integration tends to the thick model while the distance between source and calculation point increases.

5.4.3 Magnetic flux map contours

A first straightforward result from the numerical model of the source is the computation of the constant magnetic poloidal flux surfaces produced by the distribution of currents in the total magnet system, i.e. both poloidal field coils and central solenoid; this constant poloidal flux map

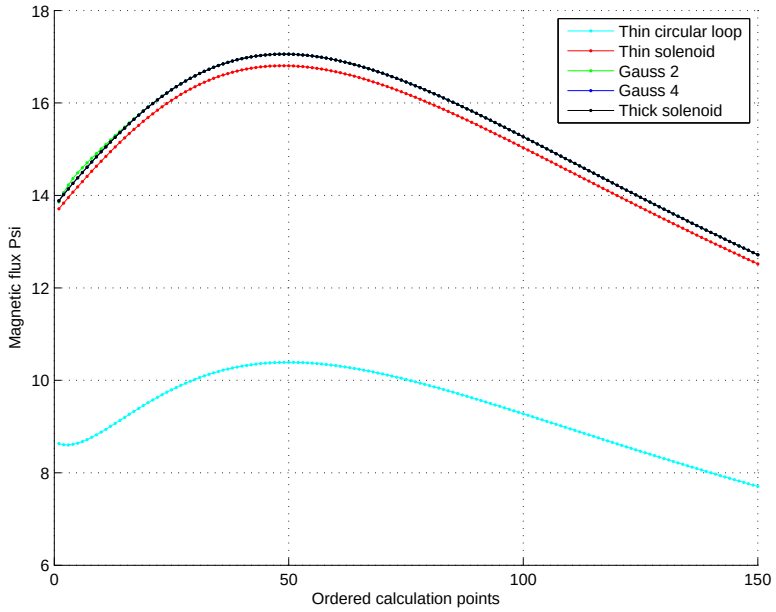

Figure 5.9: Flux CS

is shown in Fig. 5.18 and it is relative to a limited plasma equilibrium. The plasma shape is in fact controlled by position and currents in the poloidal field (PF) coils. Fig. 5.20 shows the PF coil system of ITER, together with a reference plasma equilibrium. The elongation of a plasma is mainly produced by PF coils above and below the plasma column, carrying a current parallel to the plasma current. This can also gives rise to x-points in the poloidal plasma cross-section. The current distribution in the coils produce a magnetic configuration which is the result of two type of contributions: a vertical magnetic field, which is necessary to guarantee the redial equilibrium, and a quadrupole magnetic field affecting the elongation. The vertical configuration is obtained by an up-down symmetric distributions which is similar to a cosine distribution over the six poloidal field coils: in other words the three upper coils drive positive current while the three lower one drive negative currents. In the case shown in Fig. 5.20 the currents are relative to an equilibrium set of data for a limited plasma therefore the distribution is such that the magnetic field act to hold the limited plasma in equilibrium force balance.

In order to obtain the set of nested closed toroidal flux surfaces which characterize a confined plasma, the plasma contribution to the magnetic flux must be computed and therefore added to the coil flux surfaces. The numerical model of a thin circular loop has been used to represent the filamentary plasma currents in the baricentric of the triangular mesh. The plasma magnetic flux surfaces, which are shown in Fig. 5.19, are similar to the concentric magnetic field lines produced by a rectilinear conductor. The final magnetic flux surfaces of the plasma equilibrium which involves both the coils and the plasma contriubutions, are shown in Fig. 5.20 where it is easy to recognize the limited plasma configuration.

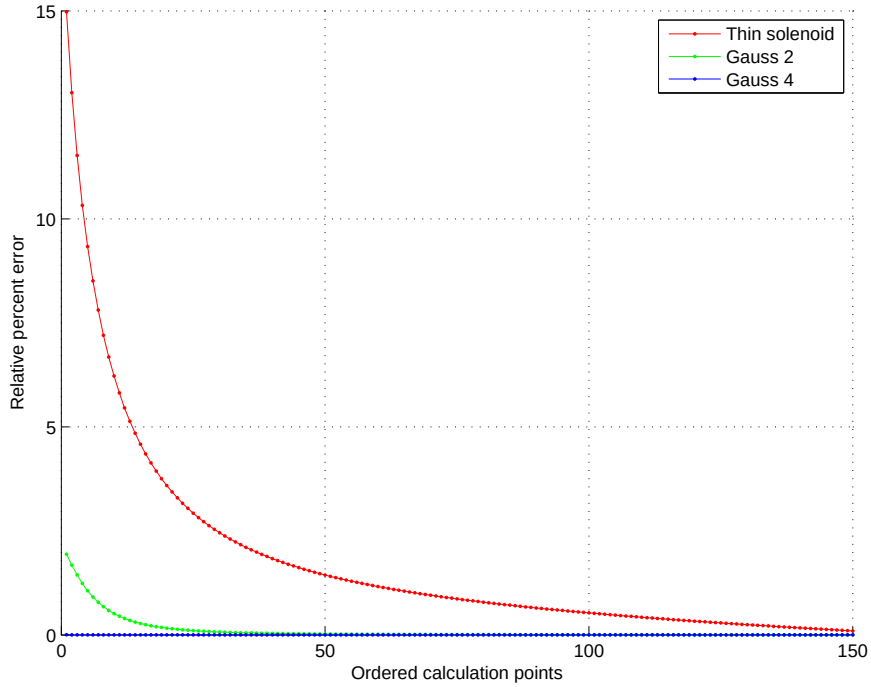

Figure 5.10: Relative percent error P6 case

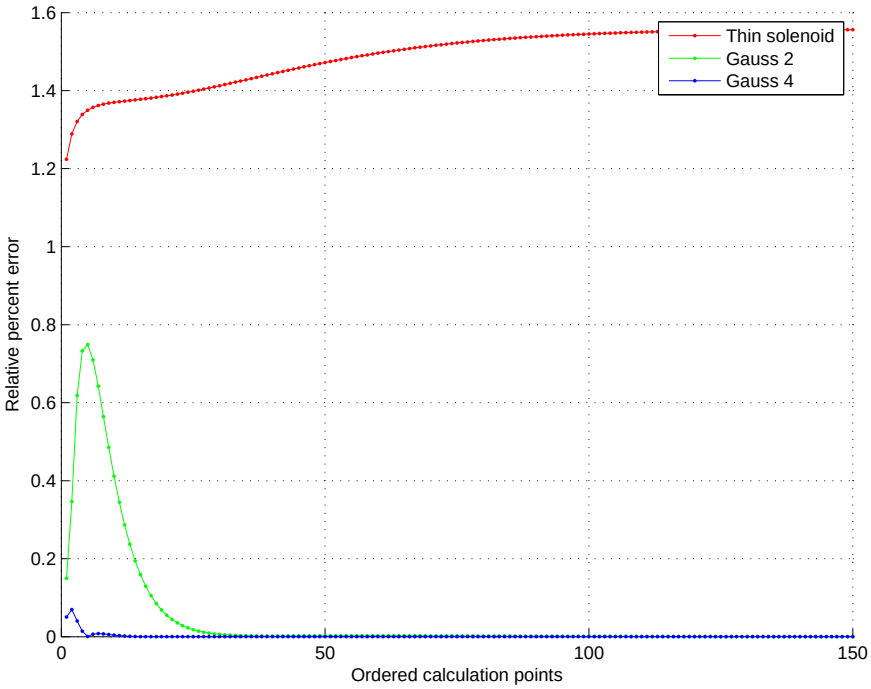

Figure 5.11: Relative percent error central solenoid case

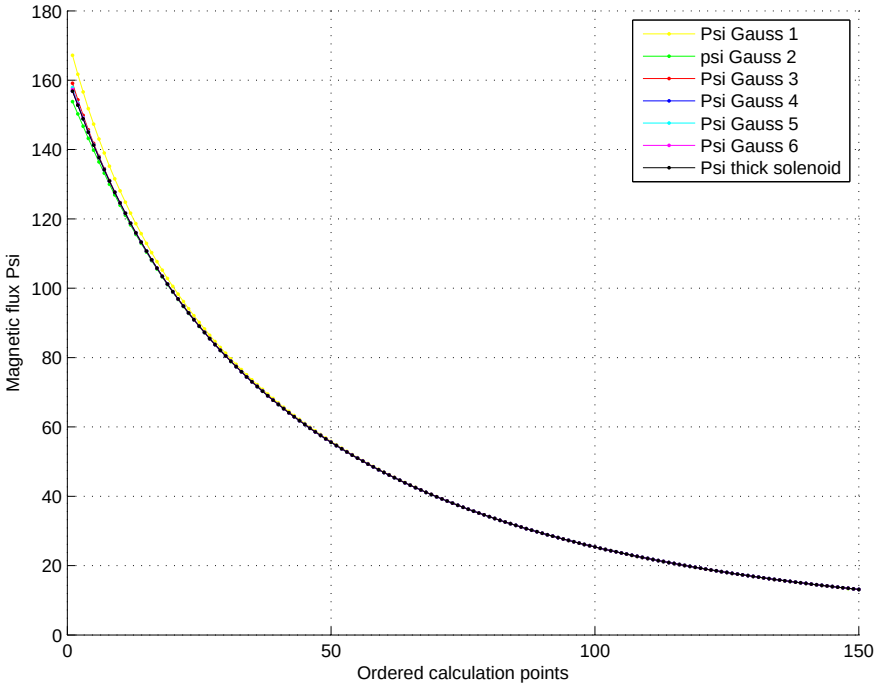

Figure 5.12: psi gauss p6

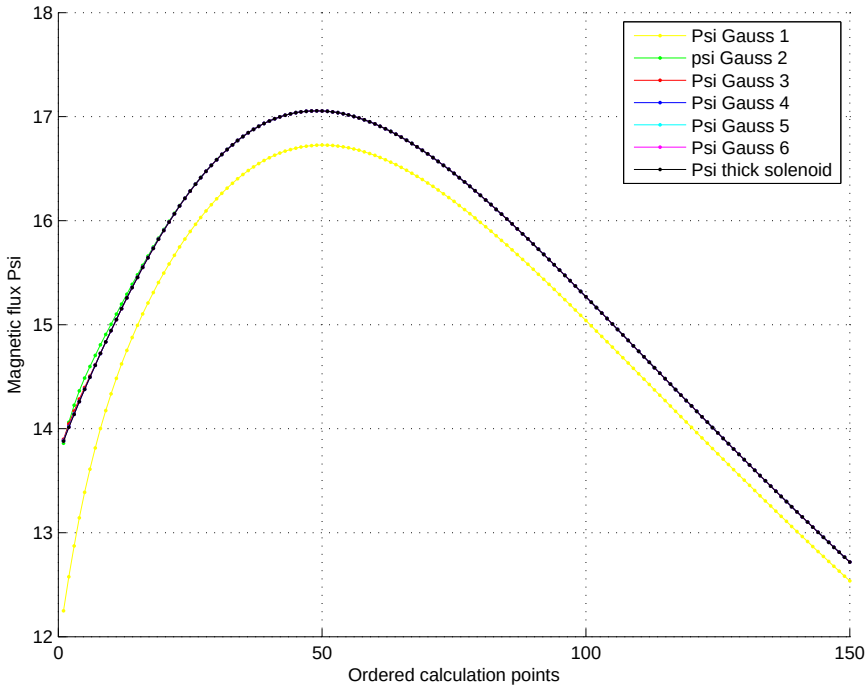

Figure 5.13: cs psi gauss

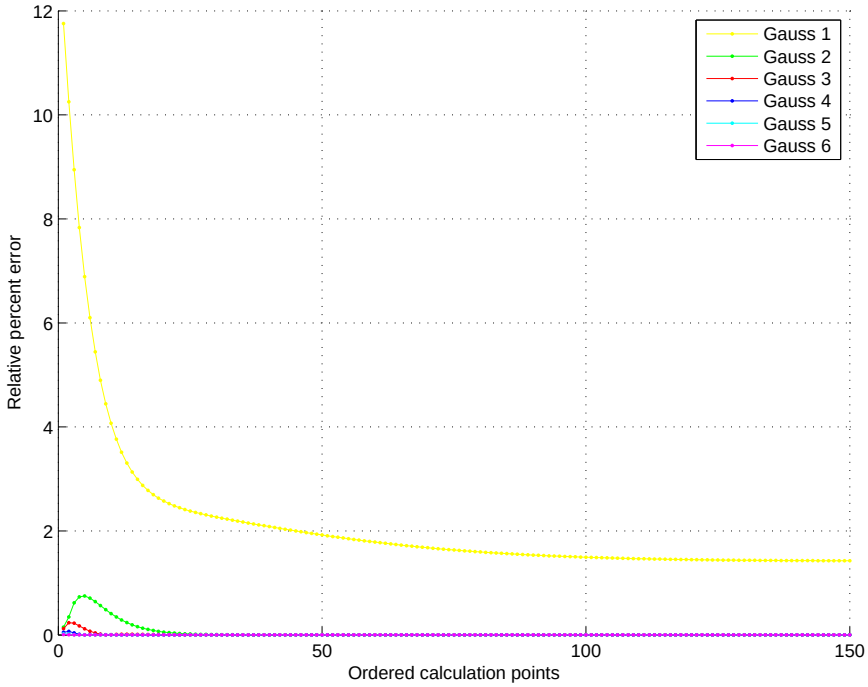

Figure 5.14: Central solenoid relative percent error for the Gauss integration method

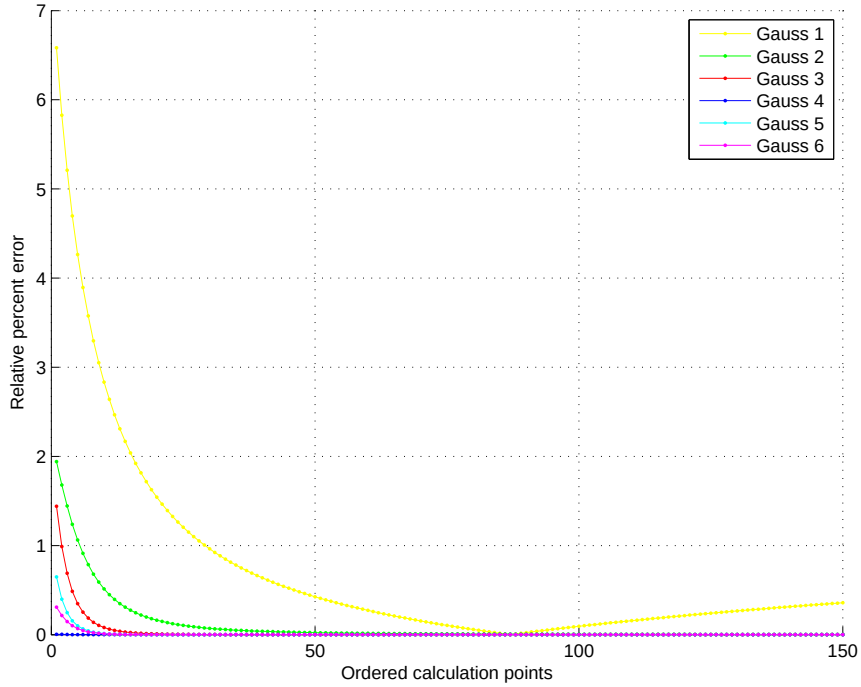

Figure 5.15: Poloidal coil P6 relative percent error for the Gauss integration method

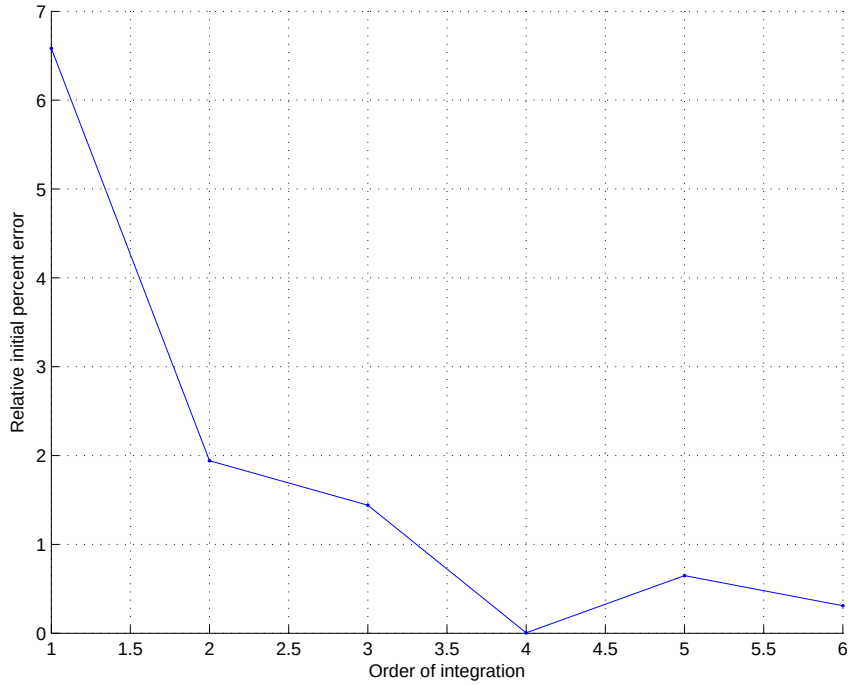

Figure 5.16: Poloidal coil P6 relative percent error with respect of the Gauss integration order

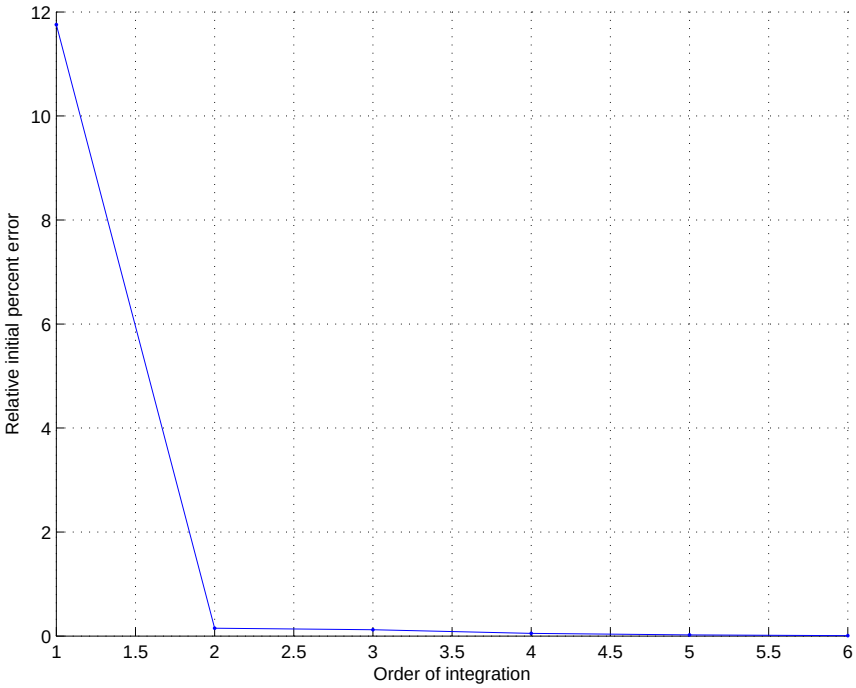

Figure 5.17: Central solenoid relative percent error with respect of the Gauss integration order

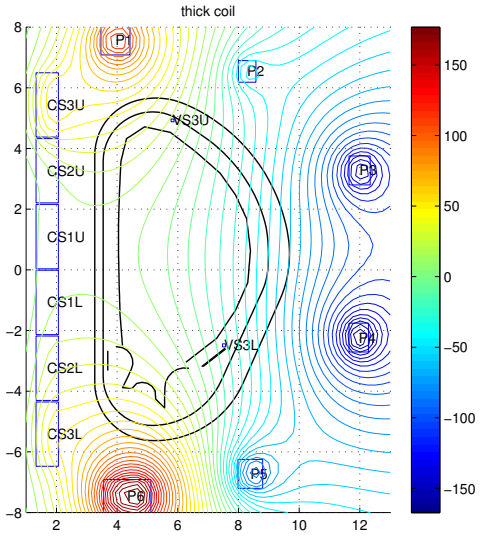

Figure 5.18: Magnetic flux surfaces due to coils currents

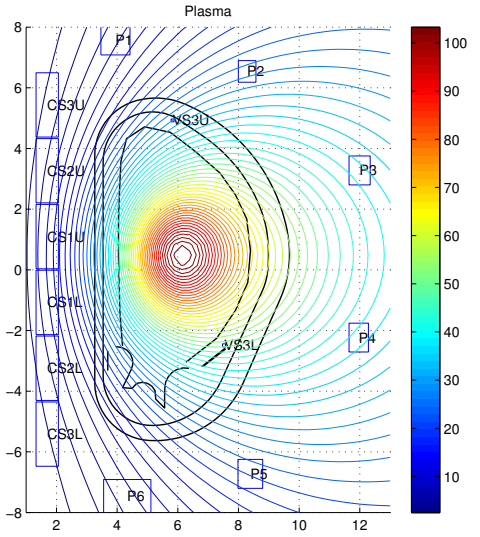

Figure 5.19: Magnetic flux surfaces due to plasma current

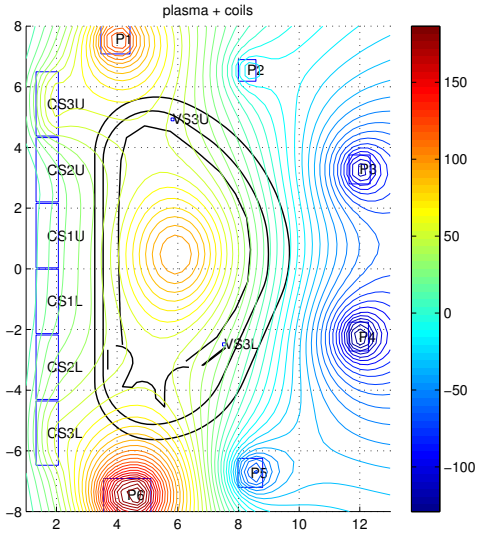

Figure 5.20: Magnetic flux surfaces due to plasma and coils contributions

Chapter 6

MHD plasma equilibrium

6.0.4 Introduction

The description of tokamak plasma equilibrium is given by the MHD equations which describe how a combination of externally applied and internally induced magnetic fields act to provide an equilibrium force balance that holds tha plasma together at the desired location inside the vacuum vessel and to isolate it from the first wall. While the physical goal is clear, the MHD equations allow a wide variety of different types of mathematical solutions and one must be certain to focus on those that correspond to confined equilibria [3]. In a qualitative view, the MHD equilibrium problem in a toroidal geometry can be split into two equilibrium: radial pressure balance and toroidal force balance. The radial pressure balance, which is shown in Fig. 6.1, is due to the nature of the plasma which is an extremely ho gas that naturally tends to expand uniformly along the minor radius r. This expansion force must be balanced by using external magnetic fields and currents. There are three basic configurations that can produce a radial pressure balance: the "θ-pinch", the "Z-pinch" and the "screw pinch" which is a combination of the two previous. The radial pressure balance problem is clearly present in both toroidal and linear geometries.

The toroidal force balance is a peculiar problem of toroidal machines: because of toroidicity, unavoidable forces are generated by both the components of the magnetic field, i.e. toroidal and poloidal magnetic fields, that tends to push the plasma horizontally along the direction of the major

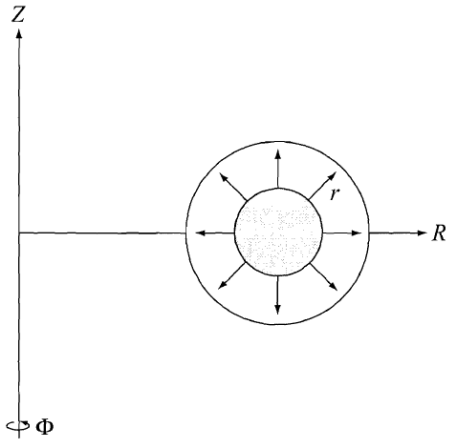

Figure 6.1: [3] Radial pressure expansion

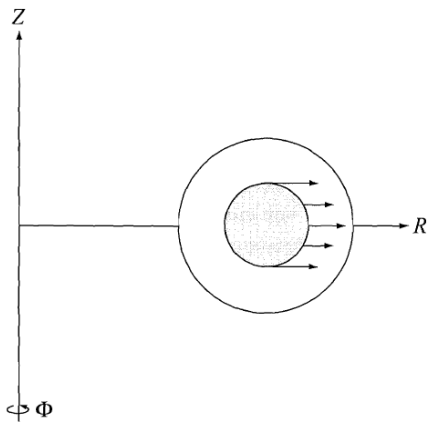

Figure 6.2: [3] Toroidal expansion

radius R as shown in Fig. 6.2. There are several methods to balance this outward toroidal force and prevent the plasma from striking the first wall such as "perfectly conducting wall" surrounding the plasma, "external verical field" and "toroidal-helical" fields [3].

The MHD ideal model can represent the plasma macroscopic equilibrium problem and it will be describe in the next sections in order to achieve the toroidal equilibrium in a 2-D axisymmetric torus.

6.0.5 MHD equilibrium model

A simple description of all the equilibrium properties of all magnetic configurations of fusion interest is given by the MHD ideal equlibrium model obtained from the entire set of MHD equations and Maxwell's equation by assuming ideal Ohm's law $\mathbf{E} = 0$, all quantities are indipendent of time $\partial/\partial t = 0$ and static plasma $\mathbf{v} = 0$:

$$\mathbf{J} \times \mathbf{B} = \nabla p \tag{6.1}$$

$$\nabla \times \mathbf{B} = \mu_0 \mathbf{J} \tag{6.2}$$

$$\nabla \cdot \mathbf{B} = 0 \tag{6.3}$$

The basic condition for equilibrium is that the force on every point of the plasma must be zero. This requires that, in equilibrium, the bulk force, i.e. the force due to plasma pressure $\mathbf{F}_p = -\nabla p$, acting on an element of plasma and directed from the center to the plasma boundary is compensated by the ampere force in every volume of the plasma as decribed by Eq. 6.1. This condition can be expressed also by the pressure balance equation which is derived from the Eq. 6.1 and Eq. 6.2:

$$\nabla(p + \frac{B^2}{2\mu_0}) - \frac{1}{\mu_0}(\mathbf{B} \cdot \nabla)\mathbf{B} = 0 \tag{6.4}$$

This equation can be rederived by expressing the magnetic induction $\mathbf{B}$ in terms of magnetic flux function labelling the magnetic surfaces: this result is known as the Grad-Shafranov equation.

It is important to notice that the plasma equilibrium set of equations are insensitive to a number of internal phenomena because they reflect the general law of conservation of momentum of the macroscopic plasma system: the processes associated with a non ideal plasma, do not change the momentum of the system, so that the form of the plasma equilibrium equations is not affected [16].

6.0.6 Axisymmetric toroidal configurations: Grad-Shafranov equation

The toroidal configuration of magnet confinement devices as Tokamaks, is the simplest and most important closed axisymmetric configuration. In order to study the equlibrium for a plasma with this geometry it is necessary to define the cylindrical coordinate system based on the major axis of the torus (R, ϕ, z) as shown in Fig. 6.3. The vector longitudinal, i.e. toroidal, components are denoted by an index ϕ. It is assumed an axisymmetric system, in which all the derivatives with respect of the toroidal direction ϕ are zero.

In these conditions, the magnetic induction field and the current density in the plasma have only poloidal and toroidal components:

$$\mathbf{B} = \mathbf{B}_p + \mathbf{B}_\phi \tag{6.5}$$

$$\mathbf{J} = \mathbf{J}_p + \mathbf{J}_\phi \tag{6.6}$$

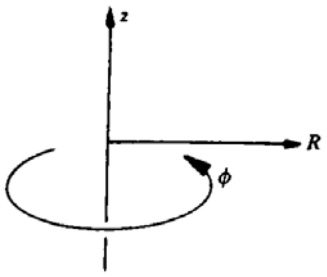

Figure 6.3: [4] Cylindrical coordinate system

From the conditions of free divergence fields:

$$\nabla \cdot \mathbf{B} = 0 \tag{6.7}$$

$$\nabla \cdot \mathbf{J} = 0 \tag{6.8}$$

and axisymmetric configurations $\partial/\partial\phi = 0$ it possible to express the poloidal components of the magnetic induction and current density fields in terms of scalar functions $\psi(R, z)$ and $F(R, z)$:

$$\mathbf{B}_p = \frac{1}{R}(\nabla\psi \times \mathbf{i}_\phi) = -\frac{1}{R}\frac{\partial\psi}{\partial z}\mathbf{i}_R + \frac{1}{R}\frac{\partial\psi}{\partial R}\mathbf{i}_z \tag{6.9}$$

$$\mathbf{J}_p = \frac{1}{R}\nabla(\frac{\psi}{\mu_0}) \times \mathbf{i}_\phi = -\frac{1}{R}\frac{1}{\mu_0}\frac{\partial F}{\partial z}\mathbf{i}_R + \frac{1}{R}\frac{1}{\mu_0}\frac{\partial F}{\partial z}\partial R\mathbf{i}_z \tag{6.10}$$

where $\psi(R, z)$ is the magnetic poloidal flux function per radian ϕ and $F(R, z)$ is the poloidal current function (or toroidal magnetic field function). Both of these functions are defined apart from an additive constant which can be chosen such that ψ represent the magnetic flux per radian and F the current within a circular contour defined by $R = const$ and $z = const$. By introducing the magnetic vector potential A_ϕ, which has only the toroidal component because of the assumption of axysimmetric system, it is possible to relate the scalar functions ψ and F to the integrals of A_ϕ and $\mathbf{B}$ around the circular contour:

$$\psi = \frac{\oint A_\phi d\mathbf{l}_\phi}{2\pi} = RA_\phi \tag{6.11}$$

$$F = \frac{\oint Bd\mathbf{l}_\phi}{2\pi} = RB_\phi \tag{6.12}$$

The poloidal flux function ψ represent the flux within the circular contour obtained by revolution of a point $(R = const, z = const)$ around the z-axis: this flux can be viewed as the flux of the central solenoid which serves to maintain the toroidal current in the plasma and does not affect the plasma equilibrium. The poloidal current function F represent the total current linked with the circular contour obtained in the same way of the poloidal flux: F can be viewed as the total current in the windings which produce the toroidal magnetic field.

Just by introducing the symmetry conditions and the definitions of scalar functions, important consequences can be derived if the equilibrium set of equations is take into account. First of all from Eq. 6.1 and Eq. 6.5 and Eq. 6.6 it is straighforward to find the relations $\mathbf{B} \cdot \nabla p = 0$ and $\mathbf{J} \cdot \nabla p = 0$: there is no pressure gradient along the magnetic field and current density lines which means that these fields lie on constant pressure surfaces. Therefore the magnetic surfaces $\psi(R, z) = const$

and the current surfaces $F(R,z) = const$ coincide and represent surfaces of constant pressure $p(R,z) = const$. Thus it is possible to demonstrate that $p = p(\psi)$ and $F = F(\psi)$.

The second consequence is the relation between the toroidal current density J_ϕ of a plasma in equilibrium and the static pressure $p(\psi)$ and poloidal current function $F(\psi)$ profiles:

$$J_\phi = \frac{1}{\mu_0 R} F \frac{dF}{d\psi} + R\frac{dp}{d\psi} \tag{6.13}$$

This dependence is important because means that the equilibrium condition restrict the possible toroidal current density distribution in a plasma instead of a two-dimenstional current distribution $J_\phi(R,z)$ in fact a one-dimensional one is obtained $J_\phi(\psi)$, depending on the profiles of $p'(\psi)$ and $FF'(\psi)$[16].

By giving the toroidal current density distribution, the equation for the poloidal flux function can be written as:

$$\triangle^*\psi = -FF' - R^2\mu_0 p' = -\mu_0 R J_\phi \tag{6.14}$$

where F' and p' are the derivatives of the poloidal current function $F(\psi)$ and the static pressure $p(\psi)$ and $\triangle^*$ is the "Shafranov operator", which applied to the poloidal flux ψ correspond to:

$$\triangle^*\psi = R\frac{\partial}{\partial R}\frac{1}{R}\frac{\partial \psi}{\partial R} + \frac{\partial^2 \psi}{\partial z^2} \tag{6.15}$$

Eq. 6.14 determines the equilibrium configuration for an axisymmetric plasma and represent a second-order elliptic semi-linear partial differential equation for the poloidal magnetic flux function ψ usually called as Grad-Shafranov-Schluter equation. The non-linearity is contained in the two functions $p'(\psi)$ and $FF'(\psi)$. In fact it is simply a magnetostatic equation with a non linear toroidal current distribution. A few considerations can be done by looking at Eq. 6.14: the pressure gradient p' is balanced by the terms FF' representing the $\mathbf{J}_p \times \mathbf{B}_t$ force and $\triangle^*\ \psi$ representing the $\mathbf{J}_t \times \mathbf{B}_p$ force [17]. The right hand side of Eq. 6.14 represents the plasma current: if it is a linear function of ψ or constant, it is possible to obtain an exact analytical solution of the equation. otherwise it is possible to rely on approximate solutions derived by numerical solutions. Usually, some simple distributions of $F(\psi)$ and $p(\psi)$ are assumed and the Grad-Shafranov equation is solved for $\psi(R,z)$.

The important difference between axisymmetric toroidal and straight cylinder equilibria is that it is impossible to the former without a toroidal, i.e. longitudinal, current [16]. It is clearly evident from Eq. 6.13 where the longitudinal current J_ϕ cannot vanish everywhere beacause of the additional dependence on the major radius R: the reason of this is the so called balooning effect. As introduced in Sect. 6.0.4 the force associated to the static pressure gradient is in the increasing major radius direction because of the difference in values on the outer and inner parts of the toroidal surface. Another reason is the global force directed along the major radius and acting on the poloidal currents in the toroidal magnetic field. These forces must be balanced by the interaction of the toroidal current and the poloidal magnetic field.

6.0.7 Global description of equilibrium configurations

The purpose of the magnetic system is to generate the magnetic fields that confine the plasma inside a vacuum vessel and keep it isolate from the first wall. The MHD equations that describe the plasma equilibrium allows several variety of different types of mathematical solutions. Obviously a plasma can be qualitatively defined as "confined" when the static pressure is zero at the boundary and

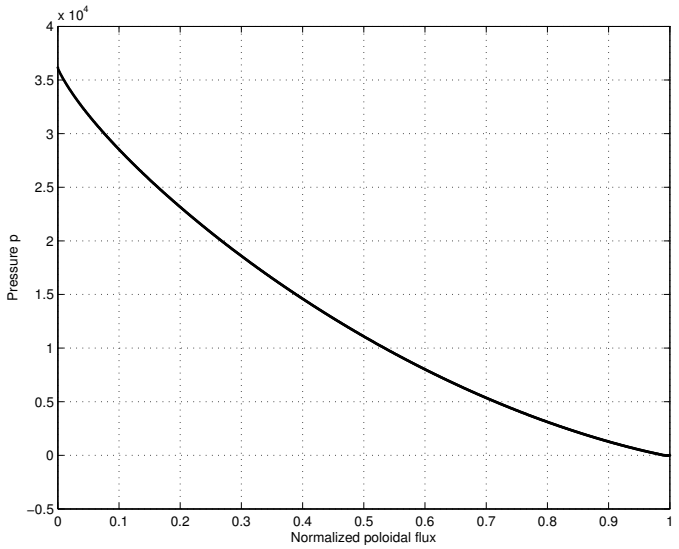

Figure 6.4: Static pressure profile

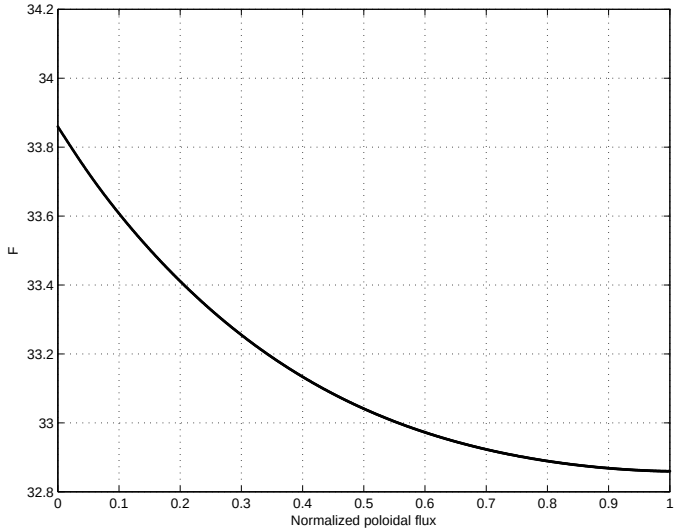

Figure 6.5: Poloidal current function profile

maximum at the centre. In order to obtain a well confined plasma, the theory of equilibrium says that the $p(\psi)$,$F(\psi)$,$p'(\psi)$ and $FF'(\psi)$ profiles are required because of the functional dependence of the toroidal current density J_ϕ. Since the range of variation of ψ is not known before-hand, the static pressure and poloidal current function profiles are generally expressed in terms of a dimensionless argument $\bar{\psi}$ called "normalized poloidal flux":

$$\bar{\psi} = \frac{\psi - \psi_a}{\psi_b - \psi_a} \tag{6.16}$$

where ψ_b is the poloidal flux at the boundary and ψ_a is the poloidal flux at the magnetic axis. The normalized poloidal magnetic flux defines the range of its variation from 0 to 1 and helps to represent the toroidal current distribution before equation is solved. Typical profiles of p,F,p' and FF' in terms of the normalized magnetic flux are shown for limiter and divertor plasmas equilibrium respectively in Fig. 6.4, Fig. 6.5, Fig. 6.6, Fig. 6.7 and Fig. 6.8, Fig. 6.9, Fig. 6.10,

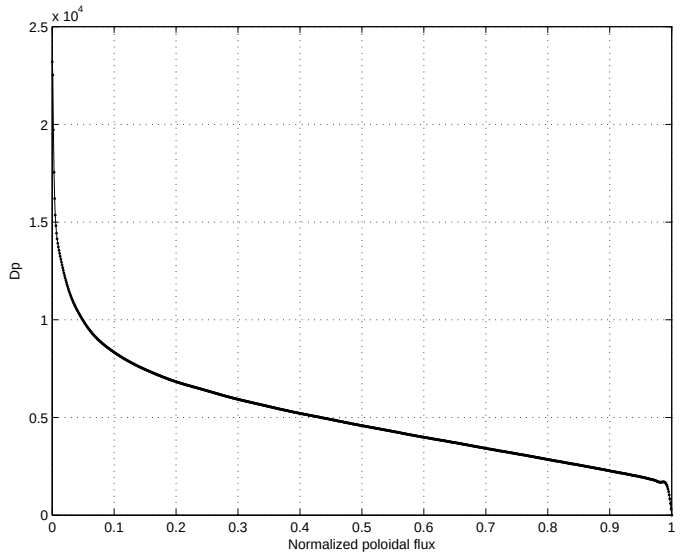

Figure 6.6: Pressure gradient profile

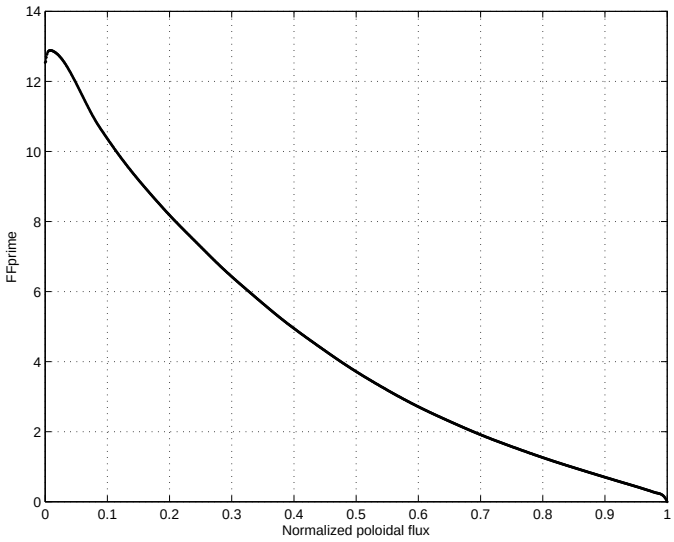

Figure 6.7: FF' profile

Fig. 6.11.

In presence of simmetry, the topology of magnetic configurations does not depend on equilibrium conditions and it is determined only by the property of magnetic field free divergence [16]. It is allowed to introduce the magnetic flux function ψ that detemines the existence of the magnetic surfaces. For every equilibrium configuration the magnetic flux and current surfaces also coincide with the surfaces of equal pressure since $\mathbf{B} \cdot \nabla p = 0$ and $\mathbf{J} \cdot \nabla p = 0$ [16]. These surfaces form a system of closed nested toroids because of the general properties of the fields. The innermost of the magnetic surfaces degenerates in a closed line called the "magnetic axis", where the magnetic flux is maximum. Any equilibrium configuration is characterized by a system of nested toroidal surfaces for the static pressure, poloidal current function and the poloidal magnetic flux. The two main plasma configurations as limiter and divertor plasmas, has been studied in order to obtain a graphic contour of these constant values nested surfaces.

The limiter plasma equilibrium is shown by means of these surfaces in Fig. 6.16, Fig. 6.17, Fig.

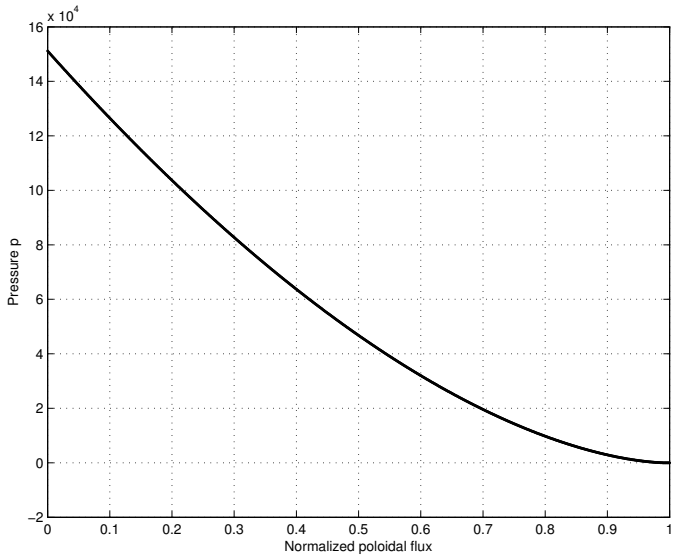

Figure 6.8: Static pressure profile

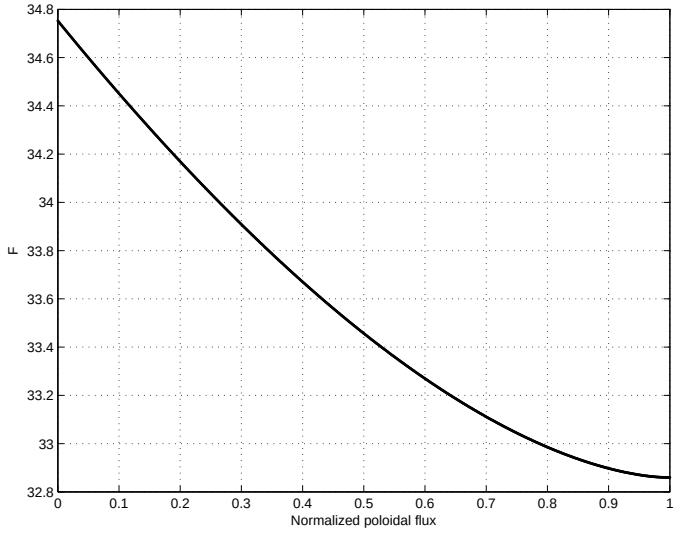

Figure 6.9: Poloidal current function profile

6.18, Fig. 6.19, Fig. 6.20, Fig. 6.21. The diverted plasma equilibrium surfaces are shown in Fig. 6.22, Fig. 6.23, Fig. 6.24, Fig. 6.25, Fig. 6.26, Fig. 6.27. The toroidal plasma current density is distributed in accordance with the function ψ as described in Eq. 6.13. Fig. 6.28 and Fig. 6.29 shows respectevely the toroidal current density distribution for the limiter and diverted plasma equilibrium obtained by using a baricentric filamentary representation of the plasma current over a triangular mesh.

6.1 Cell method for solving plasma equilibrium problem

The traditional mathematical treatment of physics is based on the differential formulation of its physical laws and it easily leads to differential equations or partial differential equations. The differential formulations are characterized by the fact that if these differential equations admit analytical solutions it is only for simple cases: in order to solve practical interest cases in physics

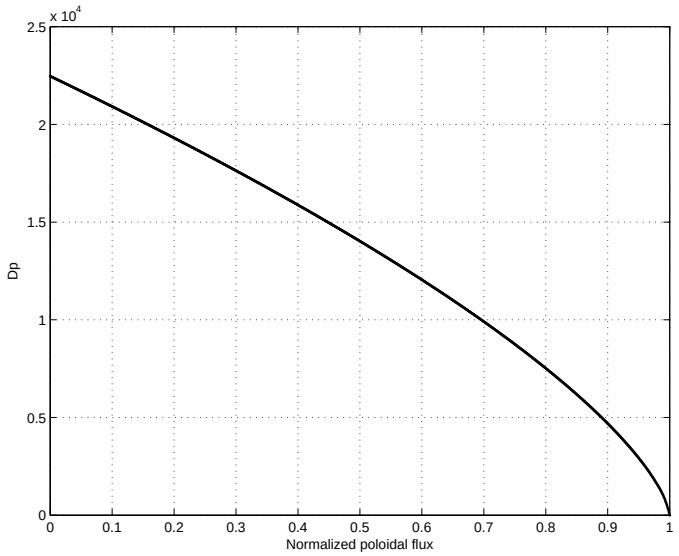

Figure 6.10: Pressure gradient profile

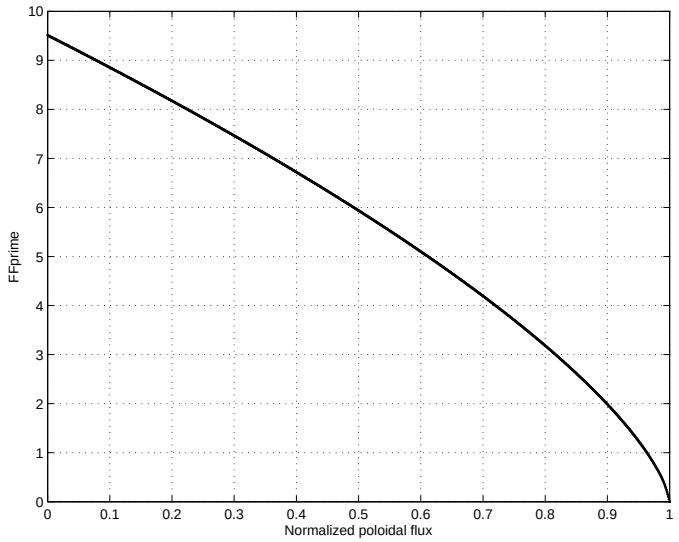

Figure 6.11: FF' profile

and engineering, the solution procedure must involve the use of numerical techniques which permits to solve these equations for more complex cases. Computational physics uses different methods to discretize differential equations, such as FEM, BEM, FDM, FVM, all based on purely mathematical approaches, i.e. without relation to the physical phenomenon described by the equation. Since the Galerkin method is based on energy principles, it appears more "physical" compared to other methods; however, the criterion to approximate the unknown solution of a physical problem by a linear combination of shape functions that are chosen in an arbitrary way, is a purely mathematical one [5]. Furthermore, in order to find the coefficients of the linear combination, the criterion to require that the residual of the differential equation is orthogonal to the every shape functions, is also a purely mathematical criterion [5].

In general partial differential equations are solved by first discretizing the equation, bringing it into a finite dimensional domain in order to reduce the problem to the solution of an algebraic equation. The typical resolutive steps involve the discretization of the domain of the problem into

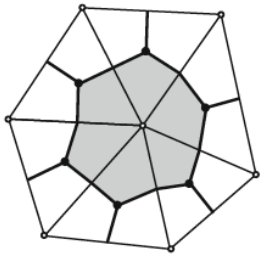

Figure 6.12: [5] Barycentric dual denoted by thick line

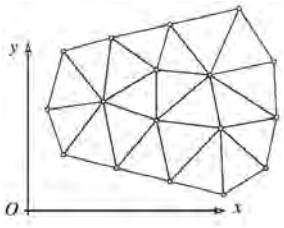

Figure 6.13: [5] A simplicial complex

a collection of subdomains, with each subdomain represented by a set of element equations to the original problem, followed by a systematically recombination of all sets of element equations into a global system of equations for the final calculation. The global system of equations has known solution techniques, and can be calculated from the initial values of the original problem to obtain a numerical answer. In the first step above, the element equations are simple equations that locally approximate the original complex equations to be studied, where the original equations are often partial differential equations (PDE). The process eliminates all the spatial derivatives from the PDE, thus approximating the PDE locally with a set of algebraic equations for steady state problems or with a set of ordinary differential equations for transient problems. These are called the element equations. In the second step, a global system of equations is generated from the element equations through a transformation of coordinates from the local subdomains nodes to the global nodes.

A different approach is possible and has been used to solve the plasma equilibrium problem. An analysis of the mathematical structure of physical theories allows for a numerical solution of any specific problem, because it directly provides an algebraic form of the equations. The algebraic formulation is obtained by using global variables and taking into account their association with the space (and time) elements, directly provides systems of algebraic equations needed for the numerical solution. This opens the way for a new method of calculation based on geometry rather than on mathematics, because it is not necessary to make the discretization of differential equations. The use of global variables leads to an algebraic (or discrete or direct or finite) formulation of physical theories, which is an alternative to the differential formulation. The most important aspect of the algebraic formulation is that it can be immediately used for computational physics by using a cell complex and its dual in the computational domain. The formulation avoids the traditional discretization of differential equations, which was described above, because of the use of global variables and global form of balance equations. In addition, from a computational point of view the direct algebraic formulation avoids all the typical difficulties linked to differentiability such as the use of generalized functions, the splitting of physical laws into differential equations in the regions of regularity and jump conditions across the surfaces of discontinuity [5]. The numerical method based on a direct algebraic formulation is called the "cell method" and requires the basic concepts of cell complexes.

6.1.1 Complexes basic concepts

A cell complex formed by simplices is called a *simplicial complex* and it is shown in Fig. 6.13. A mathematical description of physical fields using global variables needs to consider global variables as set functions, not point functions, i.e. they are associated with lines, surfaces and volumes, not only with points. Therefore a coordinate system is not the most appropriate framework: the most natural framework is a cell complex which is a subdivision of a space region into small elements called cells, i.e elements in FEM method. These cell complexes offer all the space elements needed for the algebraic formulation: points (vertices), lines (edges), surfaces (faces) and volumes (cells). In the algebraic formulation of physics cell complexes play the same role that coordinate systems play in the differential formulation [5]. The cell complex is obtained by a discretization of the space region by subdividing it into elements of an arbitrary shape. If triangles are used in the bi-dimensional case, the *simplicial complex* of cells is obtained because triangle elements are the simplest polygons. i.e simplices, in the two dimensional space. The most natural cell complexes are the *coordinate cell complexes* which are formed by the coordinate lines and surfaces of a coordinate system such the Cartesian coordinate system. The use of coordinate cell complexes is implicit in the customary derivation of gradient, curl and divergence in Cartesian and in curvilinear coordinate systems. A differential equation implies a neighbourhood of every point and not only the point itself. This neighbourhood acts as an auxiliary region of the point, and its extension is undefined. For example to evaluate the gradient of a scalar function, we must evaluate the function increments along the coordinate lines; to evaluate the curl of a vector field, we must perform the line integral of the vector along the boundary of a cell face; to evaluate the divergence of a vector field, we must evaluate the flow through the boundary of a cell [5]. Therefore the algebraic formulation requires a surrounding auxiliary region around every nodes of a cell complex. All these auxiliary regions constitute another cell complex, called a *dual* cell complex of the complex. A cell complex formed by simplices is called a *simplicial complex* and it is shown in Fig. 6.13. Starting with a cell complex called a *primal*, denote by $\mathbf{K}$, it is possible to construct another complex called a *dual* cell complex, or its *dual*, denote by $\widetilde{\mathbf{K}}$. The simplest way to construct a dual complex is by using the *barycentric cells* which are polygons obtained by connecting the barycentre of every triangle with the midpoint of the edges of the triangles, as shown in Fig. 6.12. The dual cell complexes for the limiter and divertor plasma cases are shown in Fig. 6.15 and Fig. 6.14. An important property of the cell complexes is the *duality relation* between the elements of the primal and dual complexes: every vertex of the primal cell complex lies in the centre of a dual cell; each edge of the primal complex crosses a face of the dual complex; each face of the primal is crossed by an edge of the dual, and each cell of the primal has a vertex of the dual as its centre [5].

6.1.2 Algebraic formulation of the plasma equilibrium problem

As introduced in Sect. 6.1 the algebraic formulation is obtained by using global variables providing systems of algebraic equations which can be directly used in computational analysis. These global variables are obtained by integration of the local classic variables over the different dimensions of the cell complexes which has been conventionally oriented with a prescribed law. Therefore the classical set of Maxwell's equation can be written in global algebraic form:

$$C^T F = I \tag{6.17}$$

$$\psi = CA \tag{6.18}$$

$$\psi = M_\mu F \tag{6.19}$$

$$F = M_\nu \psi \tag{6.20}$$

where C, $C^T = \widetilde{C}$ are respectevely the primal and dual geometrical matrix, related to the geometrical aspects that related the line integration of the magnetic field with the surface integration of the current density field and the line integration of the magnetic vector potential A with the surface integration of the magnetic field. Similarly for the M_μ and M_ν matrixes which are the material coefficients multiplied by geometrical factors related to the new global variables. F is the integration of the magnetic field over the cell's edge, so it is called the "magnetic tension".

As already said in Sect. 6.0.6, the Grad-Shafranov equation is a magnetostatic equation with a non linear toroidal current distribution. Therefore it can be formulated in an algebraic global form by substituiting one inside each other the Eq. 6.17, Eq. 6.18 and Eq. 6.20 obtaining the algebraic magnetostatic equation:

$$C^T M_\nu C A = I \tag{6.21}$$

and therefore because of the axysimmetric configuration, the Grad-Shafranov algebraic equation is obtained:

$$C^T M_\nu C \psi = I(\psi) \tag{6.22}$$

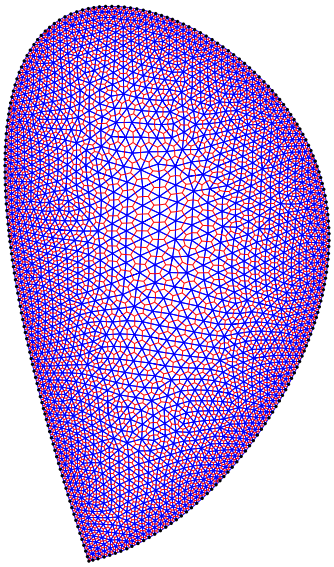

Figure 6.14: Diverted dual cell complex

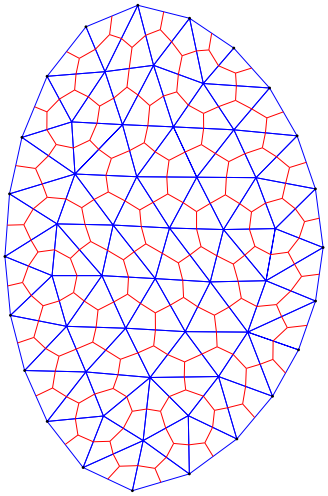

Figure 6.15: Limiter dual cell complex

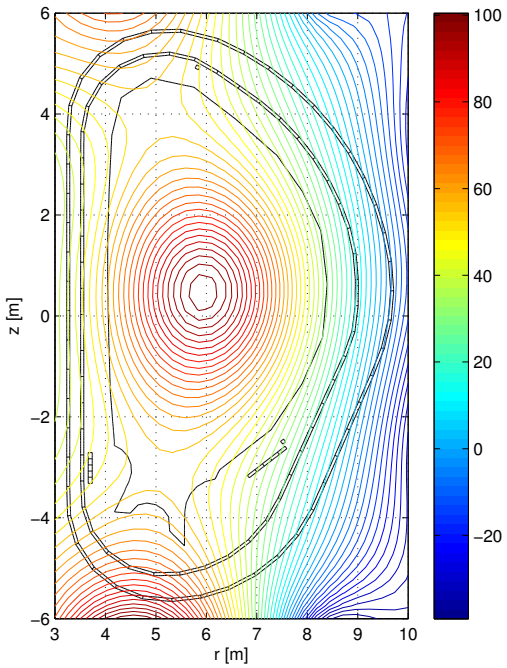

Figure 6.16: Magnetic poloidal flux surfaces for Limiter plasma

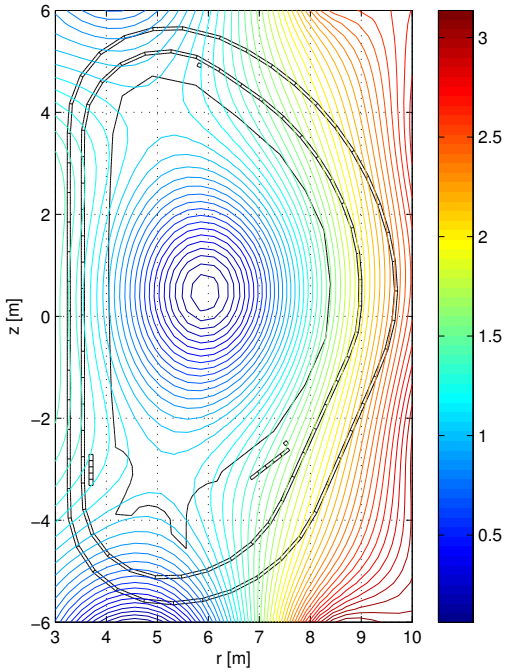

Figure 6.17: Normalized magnetic poloidal flux surfaces for Limiter plasma

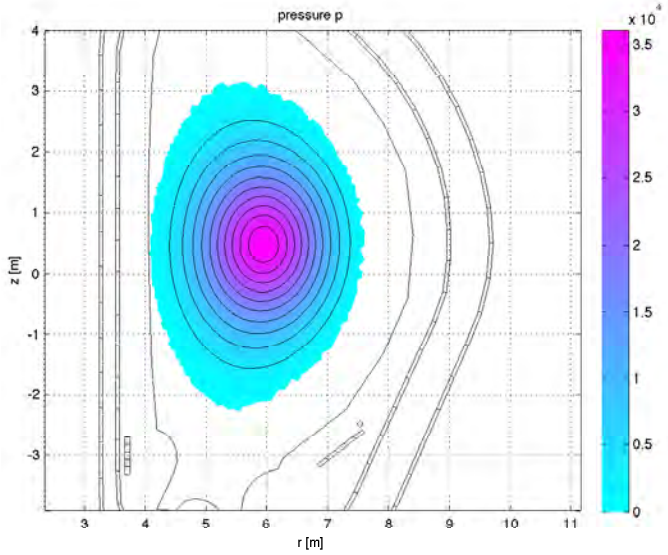

Figure 6.18: Pressure surfaces for Limiter plasma

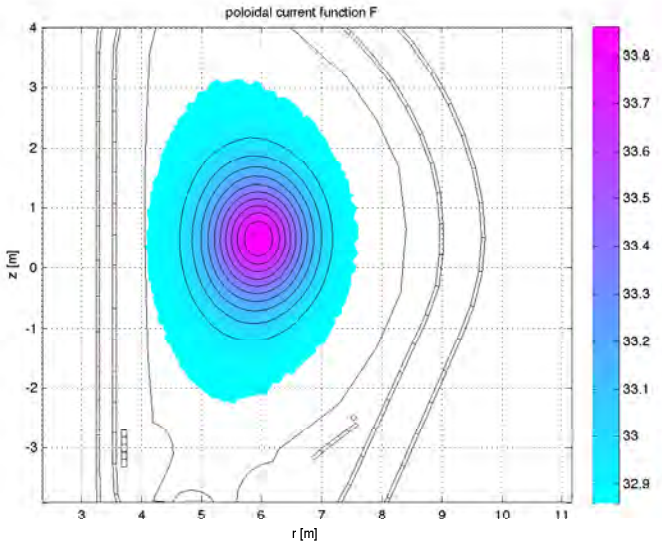

Figure 6.19: Poloidal current function surfaces for Limiter plasma

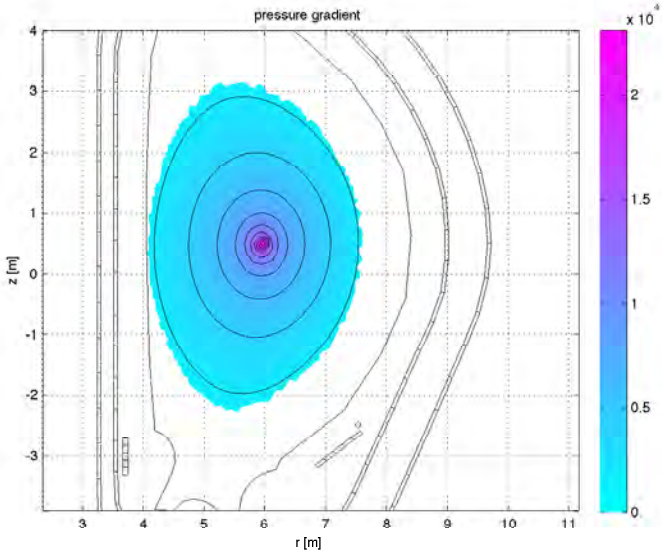

Figure 6.20: Pressure gradient surfaces for Limiter plasma

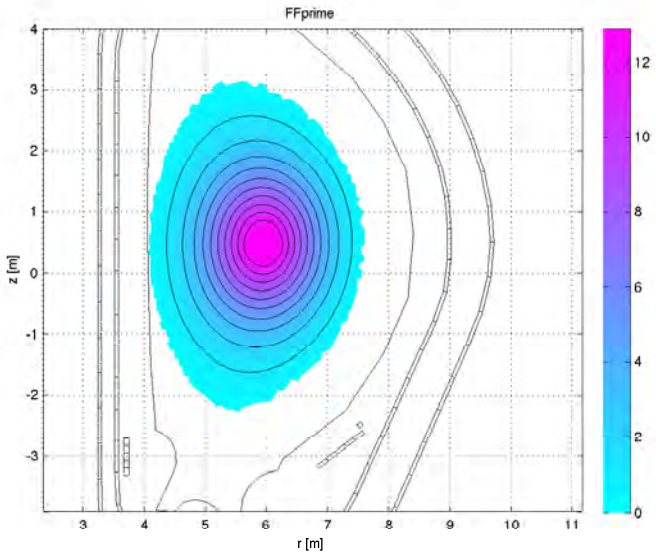

Figure 6.21: FF' surfaces for Limiter plasma

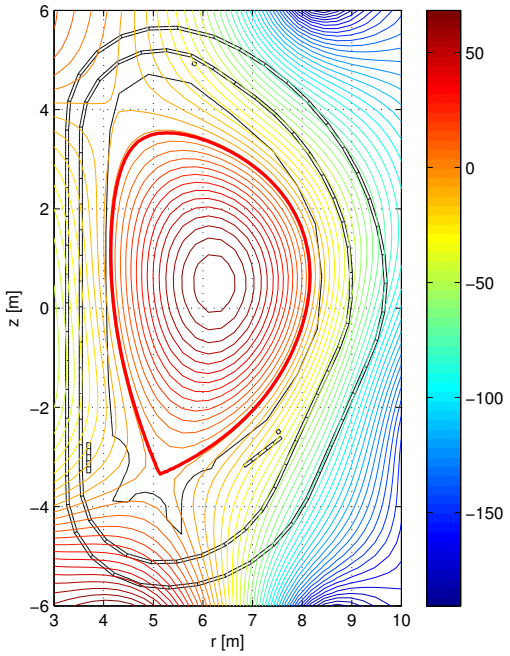

Figure 6.22: Magnetic poloidal flux surfaces for Divertor plasma

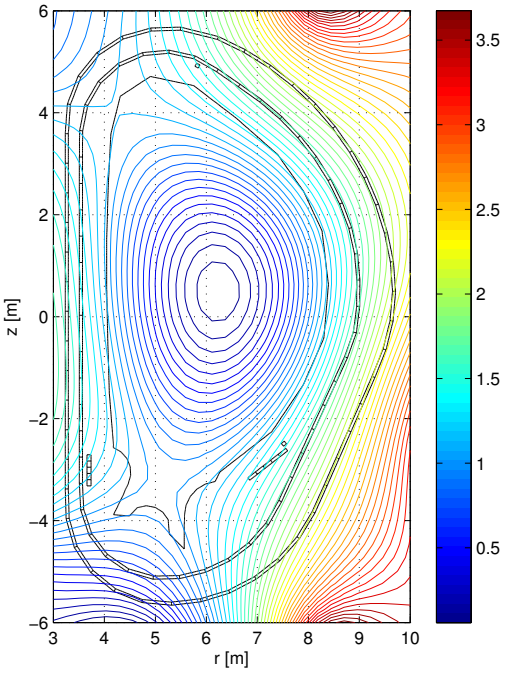

Figure 6.23: Normalized magnetic poloidal flux surfaces for Divertor plasma

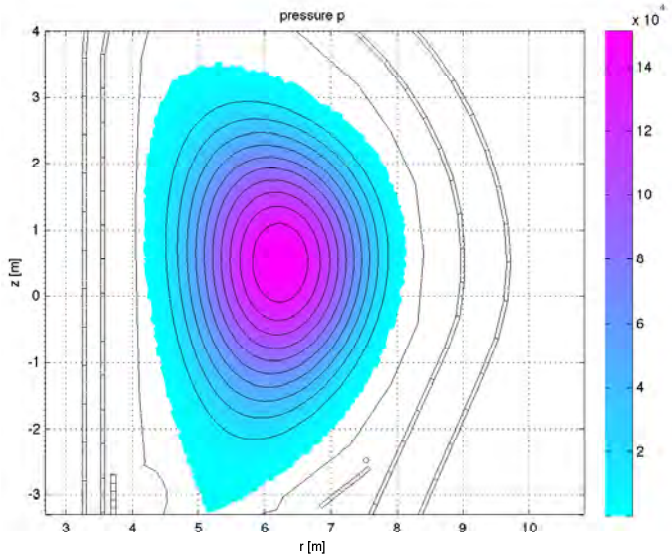

Figure 6.24: Pressure surfaces for Divertor plasma

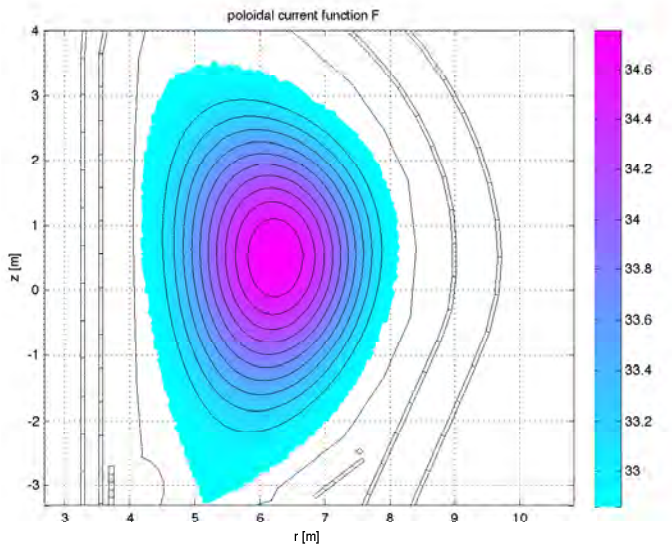

Figure 6.25: Poloidal current function surfaces for Divertor plasma

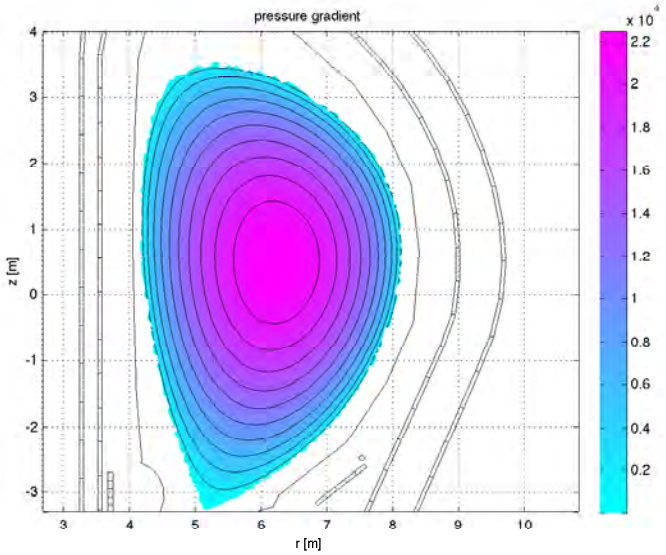

Figure 6.26: Pressure gradient surfaces for Divertor plasma

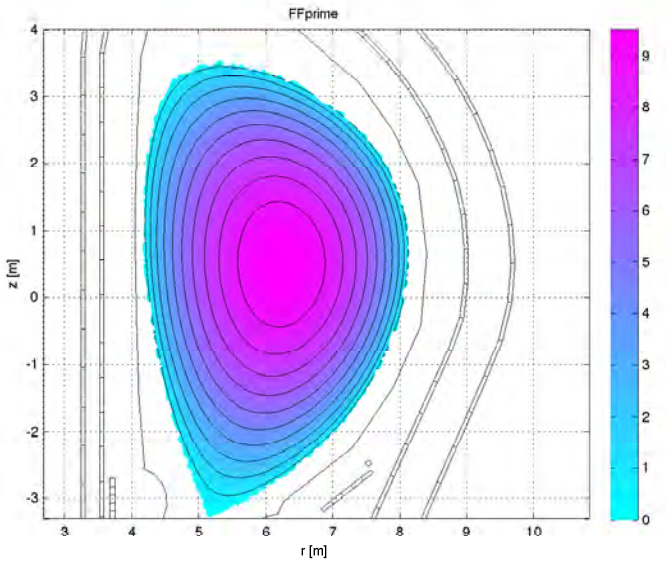

Figure 6.27: FF' surfaces for Divertor plasma

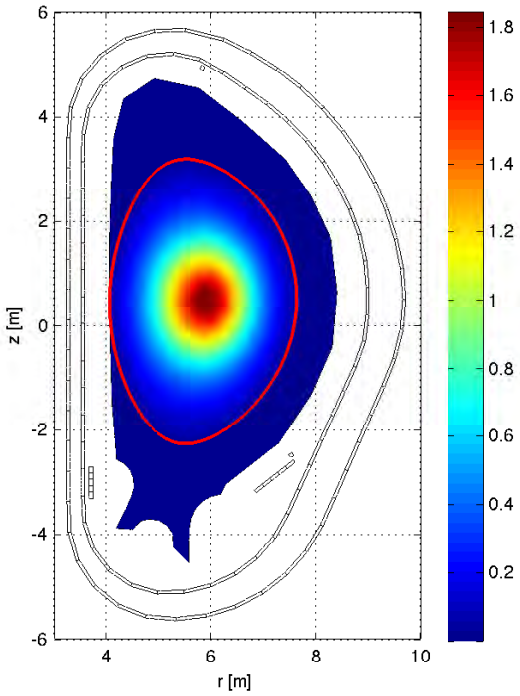

Figure 6.28: Limiter plasma current density

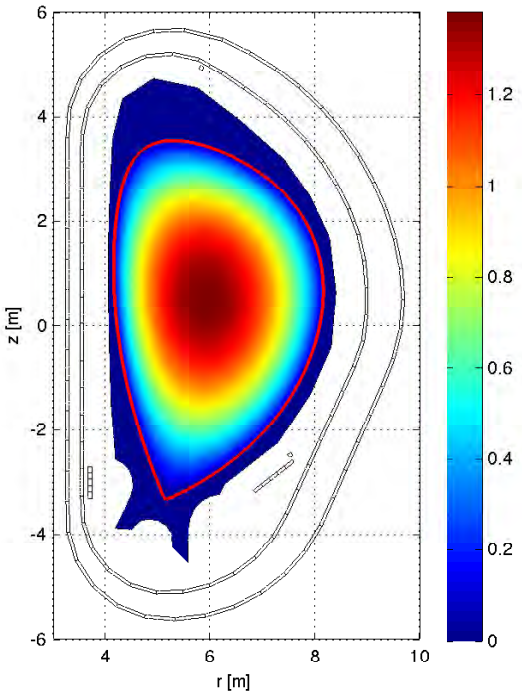

Figure 6.29: Divertor plasma current density

Chapter 7

The fixed boundary equilibrum problem

7.1 Introduction

The fixed boundary problem is defined by a fixed boundary condition over the magnetic flux on plasma edge which means that the plasma-vacuum boundary can be viewed as replaced by a surface of a perfect conductor: in this case the Grad-Shafranov equation is solved only inside the plasma region and the whole system including the vacuum region is calculated, if necessary, on the basis of the virtual casing principle by Zakharov and Shafranov [16].

In this study also the the spatial location of the plasma boundary is assumed to be given by using the analytical functional model introduced in Chap. 2 and the relative adaptive mesh. Therefore the Tokamak equilibrum problem consist of solving the equilibrum problem for the plasma inner region, i.e. plasma region, using a physical boundary condition $\psi = \psi_b = const.$ along the desired plasma boundary as it is surrounded by a perfect conducting wall. Thus the self-consistent determination of the plasma-vacuum interface, i.e. plasma boundary, is not a part of the solution procedure and therefore its important non-linearity is not applied to the Grad-Shafranov equation. The problem has a singular mild non-linearity due only to the dependence of the toroidal plasma current with the magnetic poloidal flux. The implementation of such a boundary condition has been handled directly using the cell method. The solution procedure is obtained with specified values of static pressure and poloidal current function, both refeered to the adimensional normalized poloidal flux function as already said in Sect. 6.0.7. The fixed boundary problem has been solved for two typical cases: Limiter plasma equilibrium and Divertor plasma equilibrium.

7.2 Iterative solution and results

The iterative procedure employed to solve the problem is basically a single loop Picard scheme which iterates over the non linear source term, i.e. the toroidal plasma current, and hence converge to a solution with fixed boundary values on the plasma boundary. The iteration procedure can be divided in the following steps.The first step is the "current initialization" which means the choose of a good initial soultion: this is an important aspect to start the iterative procedure. A

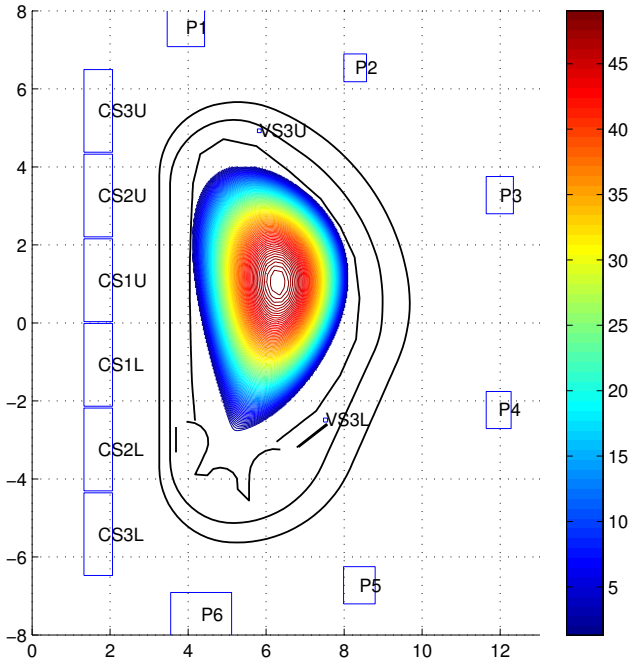

Figure 7.1: Magnetic flux surfaces of the first initial solution for the diverted plasma equilibrium

uniform distribution of plasma current density over the plasma nodes, i.e. the dual cell complex barycentrics, has been chosen not only for the first solution but also in the iterative scheme. The magnetic flux surfaces for Limiter and Divertor plasmas equilibrium first solution are shown in Fig. 7.1 and The second step is the main part of the iterative procedure and consist in updating the plasma current density distribution: the nodal values of the plasma current density are computed by using Eq. 6.13 by using an extrapolation of the $p'(\bar{\psi})$ and $FF'(\bar{\psi})$ values over the mesh nodes. The total plasma current is straightforward computed by using the dual cell complex areas and therefore boundary conditions can be imposed. The new total magnetic flux is computed and the magnetic axis is identified as the maximum value of the computed magnetic fluxes. The magnetic axis relative percent error has been calculated as a difference between the real magnetic flux axis value and the computed one.

The third step is the convergence of the iterative loop and it is tested by calculating the relative percent error of the magnetic flux in the iterative procedure:

$$\varepsilon_k = max(\frac{\psi_k - \psi_{k-1}}{max(\mid \psi_k \mid)}) * 100 \tag{7.1}$$

where k is the index of the iteration and ψ is the vector of magnetic values computed over the nodes of the mesh. The iteration procedure is stopped when $\varepsilon_k < 2$ percent. The procedure converges rapidly so that it is easy to get solutions with values of the magnetic axis error and the Picard relative error less than 1 percent. The convergence of the two equilibrium cases are shown in Fig. 7.3 and Fig. 7.4 where the relative percent error of the Picard scheme is plotted with respect of the number of iterations. Similar convergence diagrams has been obtained for the relative magnetic axis error, as shown in Fig. 7.5 and Fig. 7.6. The final magnetic flux surfaces for both cases are

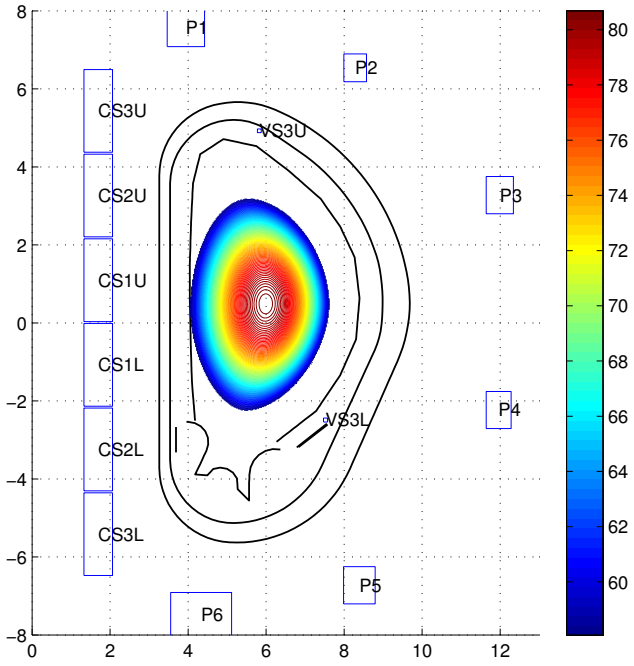

Figure 7.2: Magnetic flux surfaces of the first initial solution for the Limiter plasma equilibrium

shown in Fig. 7.7 and Fig. 7.8 and Fig. 7.9 and Fig. 7.10. The iterative procedure has been compared, for both equilibrum cases, with another solution of the Grad-Shafranov equation for the magnetic flux over another triangular mesh by using an extrapolation of these "original" values on the adaptive plasma mesh obtained in Chap. 4 in order to calculate a set of relative percent error for the computed magnetic flux. These values of the error represent the deviations between the two solutions and can be plot in a constant values error surfaces as shown in Fig. 7.11 and Fig. 7.12 respectevely for the Limiter and Divertor plasma equilibrium. It is possible to see that in the diverted plasma equilibrium, the error is higher close to the plasma boundary because this one has been characterized, starting from the data used as reference in this error analysis, by using the Bézier interpolating function.

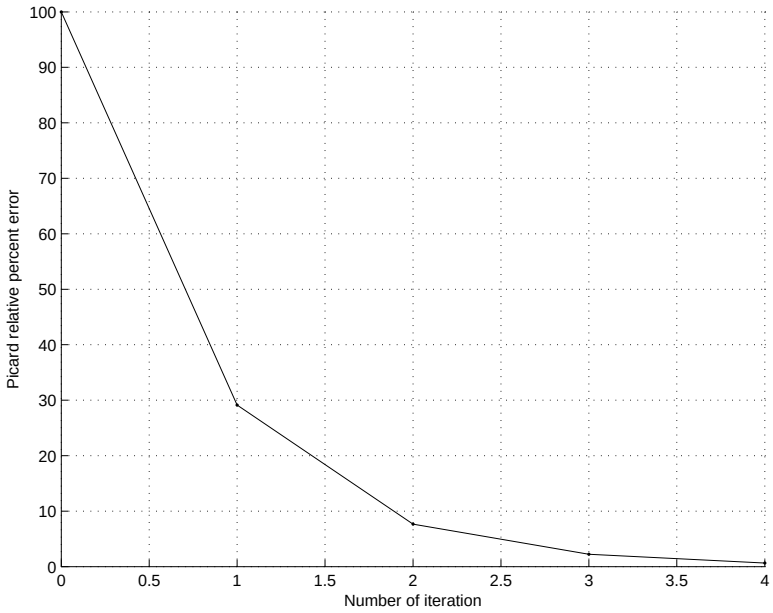

Figure 7.3: Relative percent error Limiter plasma equilibrium

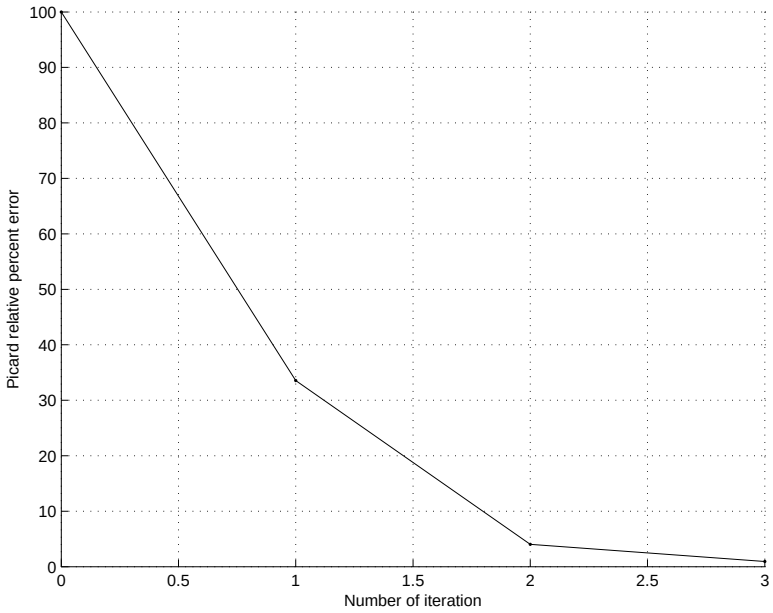

Figure 7.4: Relative percent error diverted plasma equilibrium

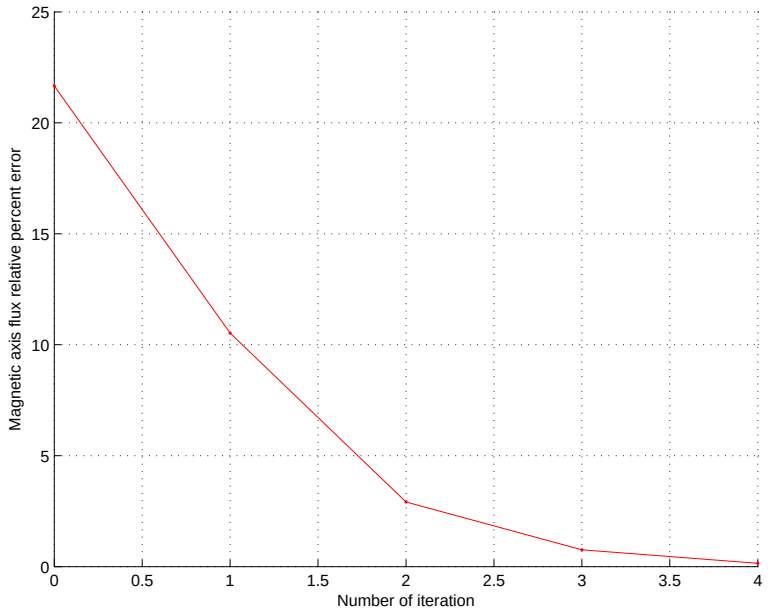

Figure 7.5: Relative magnetic axis percent error for Limiter plasma equilibrium

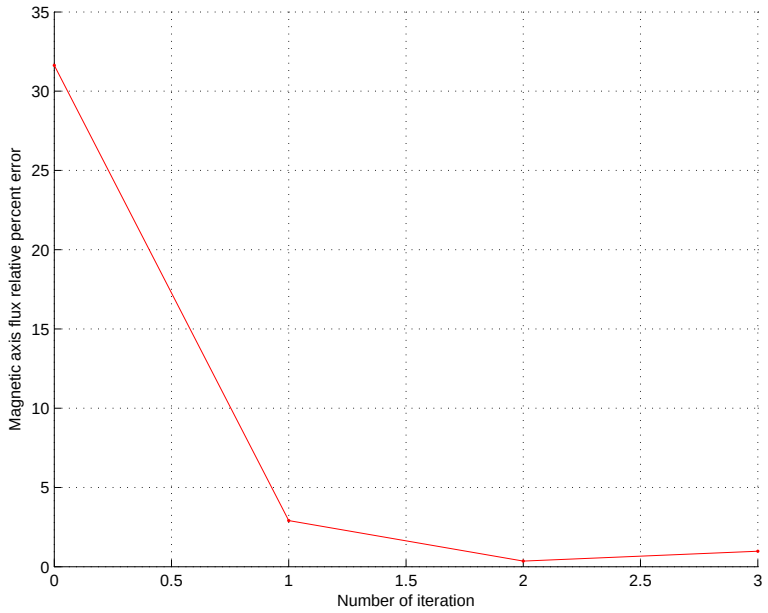

Figure 7.6: Relative magnetic axis percent error for diverted plasma equilibrium

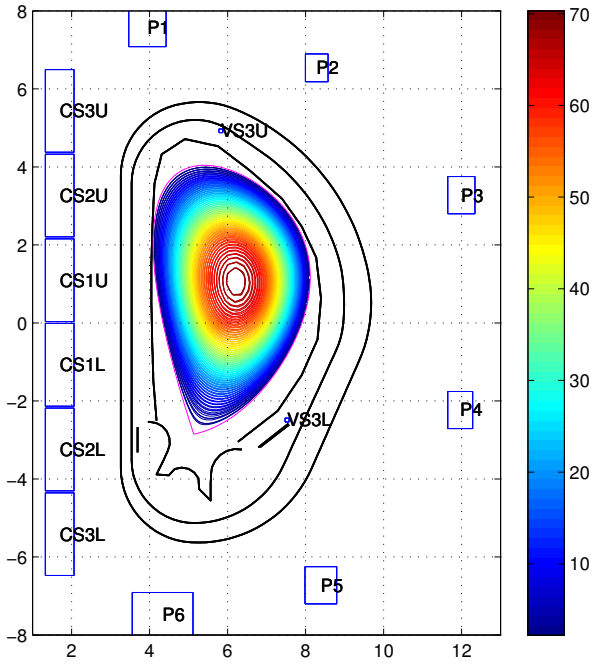

Figure 7.7: Magnetic flux surfaces of the final solution for diverted plasma equilibrium

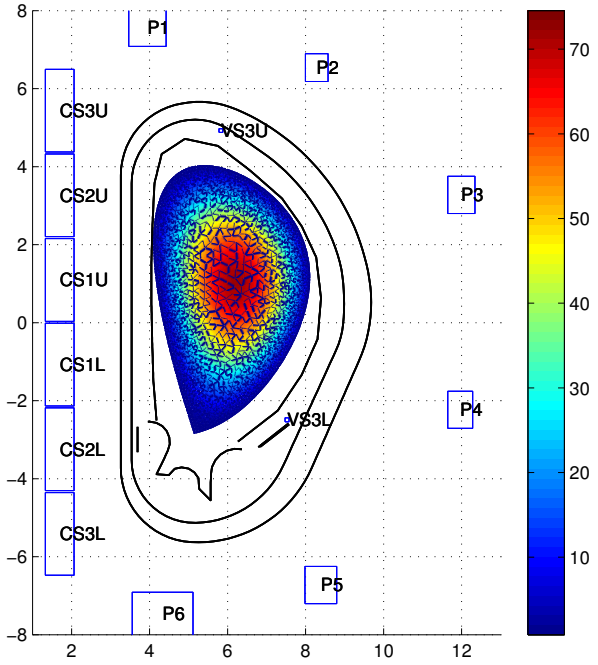

Figure 7.8: Magnetic flux patch of the final solution for diverted plasma equilibrium

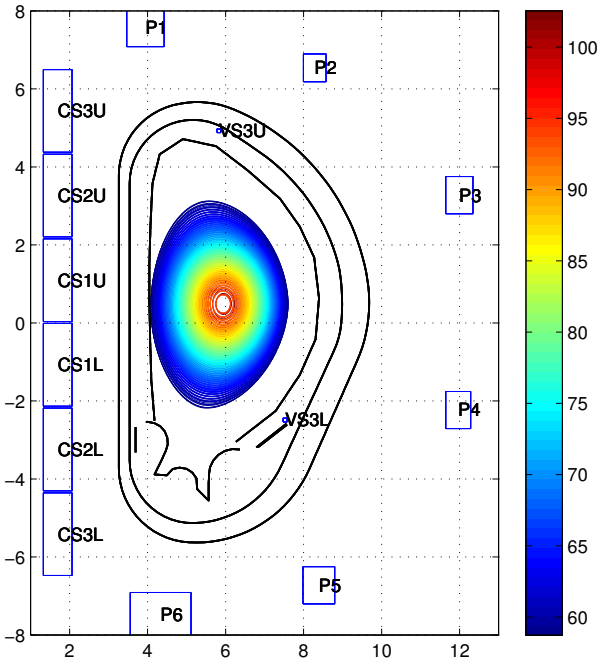

Figure 7.9: Magnetic flux surfaces of the final solution for Limiter plasma equilibrium

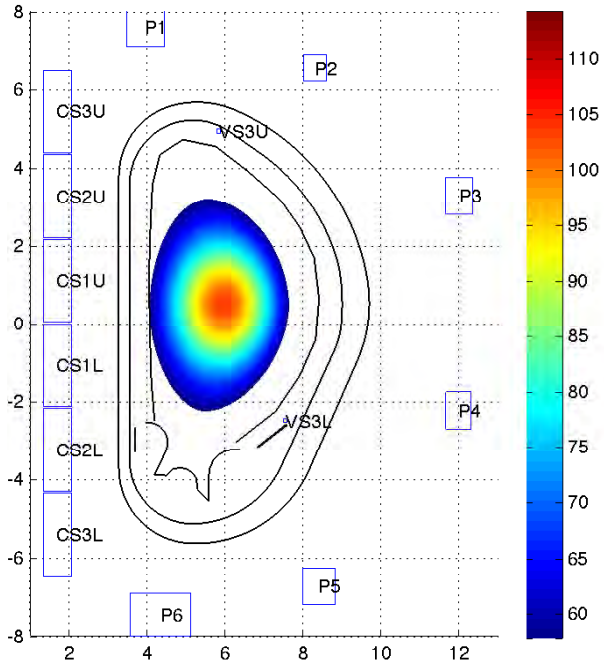

Figure 7.10: Magnetic flux patch of the final solution for Limiter plasma equilibrium

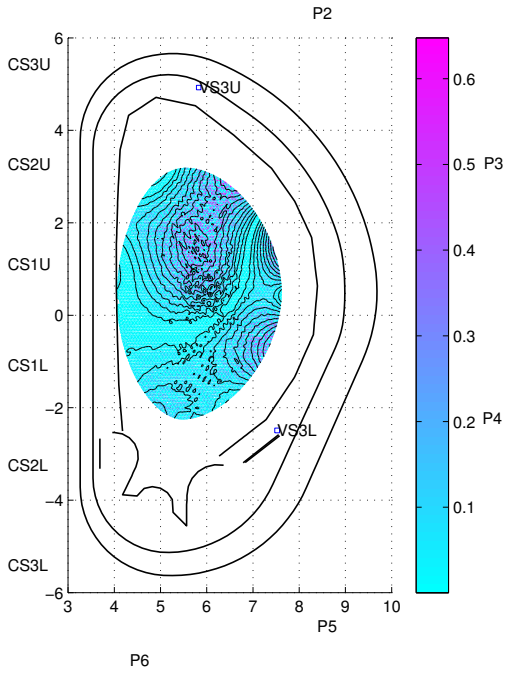

Figure 7.11: Magnetic flux error surfaces for Limiter plasma equilibrium

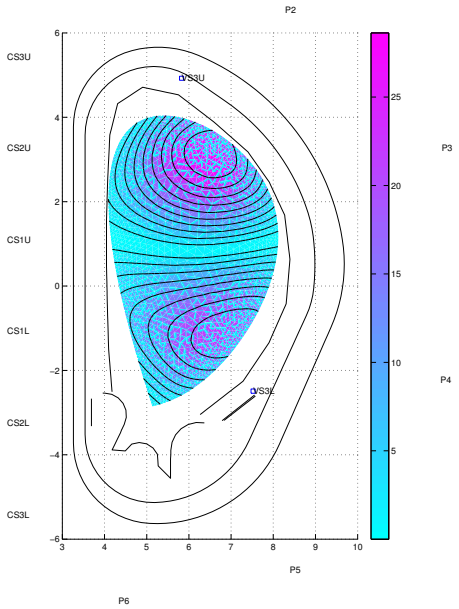

Figure 7.12: Magnetic flux error surfaces for diverted plasma equilibrium

Chapter 8

The inverse equilibrium problem

8.1 Introduction

The inverse fixed boundary plasma equilibrium problem requires to identificate the optimal values for the active coils currents in order to keep in equilibrium a plasma with a prescribed magnetic configuration (i.e. plasma shape and global parameters, namely I_p, li, β_p). The iterative solution procedure introduced in Sect. 7.2 gives the magnetic flux values due to both contributions of the plasma current density and the external conductors currents. At the boundary this relation can be obtained:

$$\psi_b = \psi_b^{coils} + \psi_b^{plasma} \tag{8.1}$$

Since the plasma is shaped by the external fields produced by the external conductors currents, it is of considerable interest for the purpose of this study to compute the singular contribution of these currents to the magnetic flux values at the boundary. The plasma boundary flux contribution ψ_b^{plasma} has been computed by using a filamentary approximation [1]. Then, the coefficients that link the filamentary currents to the plasma boundary flux are calculated and stored in a dense matrix, often referred to as Green matrix. The coils contribution to the flux at the boundary is straightforwardly obtained by subtracting the total flux at the boundary and the plasma current contribution already computed.

8.2 Problem statement

The fixed boundary problem is obviously characterized by a constant value of the flux at the boundary so the two contributions must be such that by adding them the flux value at the boundary does not change: the values of the two contributions are shown in Fig. 8.1 and Fig. 8.2 as a function of the angular coordinate along the plasma boundary ($\alpha = 3.1416$ rad outboard, $\alpha = 0$ rad top, $\alpha = -3.1416$ rad inboard) where it is clear that by adding them together, a constant boundary flux value is obtained. After these considerations, the inverse equilibrium problem can be expressed as:

$$R = GX - \psi_b^{coils} \tag{8.2}$$

[1] the singular plasma current density computed at the centroids of the triangular mesh is multiplied for each element area obtaining a set of plasma filamentary currents

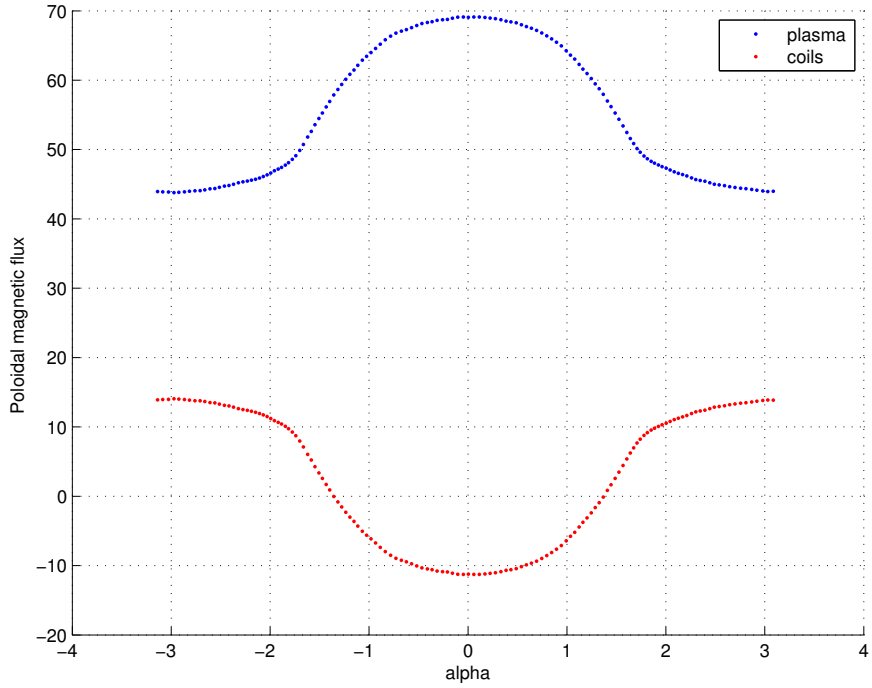

Figure 8.1: Contributions to the magnetic flux at the boundary for every point of the boundary in Limiter plasma equilibrium

where G is the Green matrix connecting each coil contribution to each boundary point, X is the vector of the unknown currents, ψ_b^{coils} is the coils contribution to the flux due to the unknown currents and F is the objective function which is to be minimized. The problem can be stated as:

$$GX - \psi_b^{coils} = 0 \tag{8.3}$$

The main objective function R is, in other words, a vector of residuals which is to be minimized.

In order to determine the necessary external currents that gives the prescribed plasma boundary it is necessary to resolve the well known overdetermined problem in which the Green matrix relates the external coils currents with the magnetic flux contribution of the same external coil currents. This problem can be roughly solved by using the Moore-Penrose generalized inverse matrix, i.e. SVD technique, without taking into account any kind of physical constraint on the current distribution. This is in general a not feasible solution because if one fixes the plasma shape very precisely, the coil currents tend to assume very large values with often in the form of dipoles which gives enormous electrodynamic loads on the conductors. In pratice the solution has to offer the best possible accuracy without excessively large coil currents. To achieve this, additionally objective functions must be introduced, each one for each physical constraint that one wants to impose.

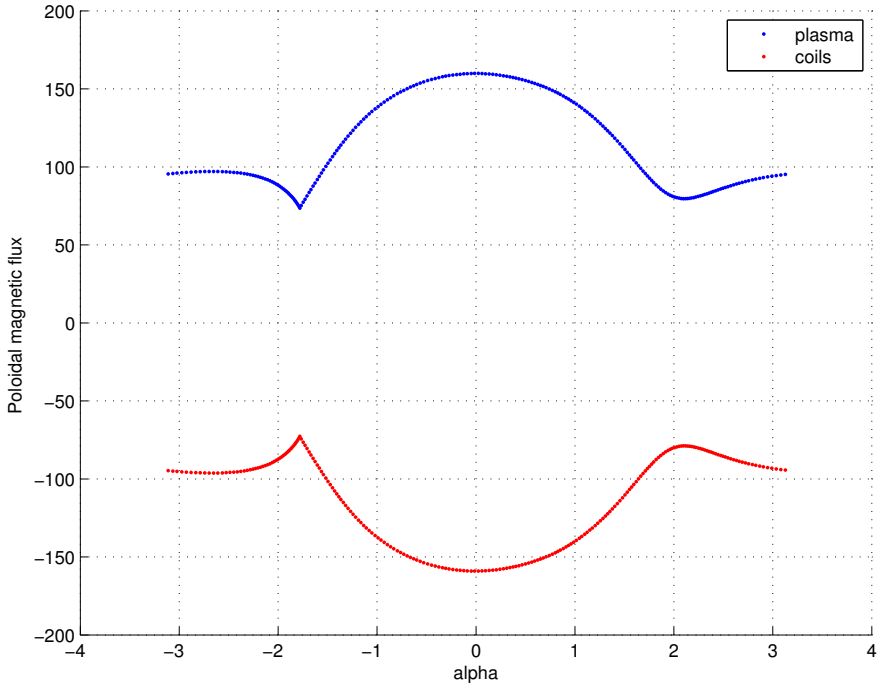

Figure 8.2: Contributions to the magnetic flux at the boundary for every point of the boundary in Divertor plasma equilibrium

8.3 Multi to single objective function: Fuzzy Logic

The multiobjective function optimization problem can be reduced to a single objective problem by using a fuzzy logic. The Fuzzy Logic is a mathematical tool for dealing with uncertainty that provides a mechanism for representing linguistic constructs such as "many", "low", "medium", "often", "few". On the contrary, the traditional binary set theory describes crisp events, events that either do or do not occur. The theory of fuzzy logic is based upon the notion of relative graded membership and so are the functions of mentation and cognitive processes [18]. The utility of fuzzy sets lies in their ability to model uncertain or ambiguous data and to preserve the standard selective single objective optimization procedure based on the direct comparisation of the value assumed by the objective function in different cases. The idea is to reformulate the multiobjective problem in a single objective form by using a set of weighting functions, i.e. membership functions, that could apply the fuzzy logic to each objective function of the original problem. The membership value is 1 if it belongs to the set or 0 if it is not a member of the set. Thus membership in a set is found to be binary i.e., the element is a member of a set or not. The fuzzy logic defines new fuzzy sets such that this membership is extended to possess various "degree of membership" on the real continuous interval $[0, 1]$. The concept of a fuzzy set contrasts with a classical concept of a bivalent set (crisp set), whose boundary is required to be precise, i.e., a crisp set is a collection of things for which it is known whether any given thing is inside it or not. It is clear that the degree of membership of any particular element of a fuzzy set express the degree of compatibility of the element with a concept represented by fuzzy set. Thus it is necessary in order to reformulate the optimization problem from multi to a single objective, to define the fuzzy set for each function. A

fuzzy system is a set of fuzzy rules that converts inputs to outputs. The fuzzy inference engine (algorithm) combines fuzzy $IF\text{-}THEN$ rules into a mapping from fuzzy sets in the input space f to fuzzy sets in the output space z based on fuzzy logic principles. The inputs and outputs can be numbers or vectors of numbers. These rule-based systems in theory model represents any system with arbitrary accuracy, i.e., they work as universal approximators. The Achilles' heel of a fuzzy system is its rules; smart rules give smart systems and other rules give smart systems and other rules give less smart or even dumb systems. The number of rules increases exponentially with the dimension of the input space (number of system variables). This rule explosion is called the principle of dimensionality and is a general problem for mathematical models [18].

In order to define the fuzzy rules that converts inputs to outputs with respect of the fuzzy sets, all the objective functions has been formulated in a scalar form. The main objective function, i.e. the residual, introduced in Eq. 8.2 which was in a vectorial form, has been used to introduce the three related objective functions. The first of those is the standard relative residual f_1, which is obtained by dividing the Euclidean norm of the residual vector for the norm of the known terms, i.e. the coils contribution to the flux at the boundary ψ_b^{coils}; it can be stated as:

$$f_1 = \frac{\|GX - \psi_b^{coils}\|}{\|\psi_b^{coils}\|} \tag{8.4}$$

Then, the other two new objective scalar functions has been defined:

$$f_2 = rms(\frac{GX - \psi_b^{coils}}{\psi_{b_{max}}^{coils}}) \tag{8.5}$$

$$f_5 = rms(\frac{GX - \psi_b^{coils}}{\psi_b^{coils}}) \tag{8.6}$$

Three objective functions,f_1, f_2 and f_5, related to the residual has been obtained.

The optimization is focused to the main problem of the physical constraints in the current values: the optimal solution is such that offers the best accuracy in the plasma boundary position, which is related to the residual, without excessively large coil currents. The accuracy is took into account by the three objective functions already defined. The physical constraints on currents can be obtained by introducing two new objective functions. The first one, f_3, is the sum of the squares of the current in each coil, which can be a flag of the total resistive power dissipation in the coils:

$$f_3 = \frac{\sum_i^{N_c} X_i^2}{k_3} \tag{8.7}$$

$$f_4 = \frac{\sum_i^{N_c} (X_{i+1} - X_i)^2}{k_4} \tag{8.8}$$

where N_c is the number of coils, X the unnknown current, $k_3 = 3 * 10^{10}$ is the sum of the squares of the maximum current in each coil. The second function f_4 is defined in Eq. 8.8 and it is the sum of the squares of the current differences in adjacent coils divided by the "worst dipole case" $k_4 = 1 * 10^{11}$, which correspond to have the same maximum value of current but with opposite sign in adjacent coils: this function is called the "dipole term", and it is related to the electrodynamic forces on the conductors.

The final result of the fuzzy logic is a new set of objective functions, each one equal to a value between 0 and 1, that can be related one from the other by using boolean operators. The

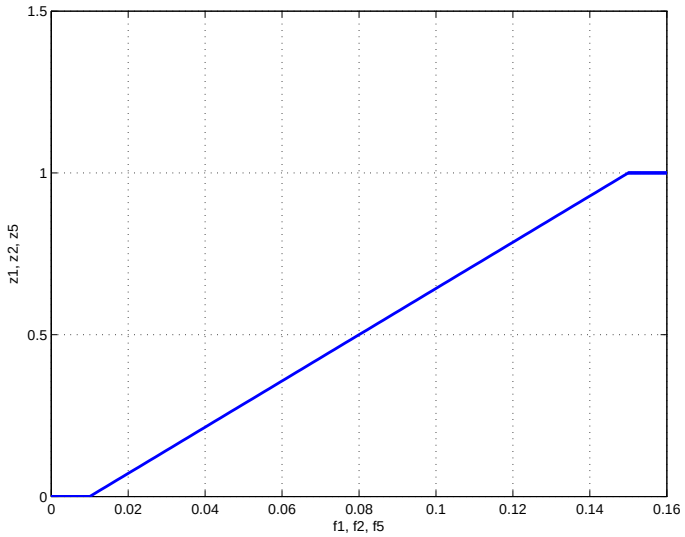

Figure 8.3: Fuzzy rule for f_1, f_2, f_5 objective functions

	Lower	Higher
f_1	0.01	0.15
f_2	0.01	0.15
f_5	0.01	0.15
f_3	0.5058	1
f_4	0.2446	1

Table 8.1: Fuzzy rules for Divertor plasma

result is a single objective function that express all the initial functions, each one graded with the predetermined fuzzy membership functions. The fuzzy rules adopted to converts input f_i to output z_i, with $i = 1, 2, 3, 4, 5$, has been diversified for each objective function but all of them are characterized by membership value, or output fuzzy set values z, equal to 0 if the function totally respects the rule or 1 if does not. Furthermore, all the fuzzy rules evolve from 0 to 1 with a linear behaviour.

The fuzzy rule of the accurcay objective functions, f_1, f_2 and f_5 has been imposed to give memebership function $z_1 = 0$ for values of the functions less greater than 0.01 and $z_1 = 1$ for values greater the 0.15 which corresponds to the 1 and the 15 per cent accuracy on the plasma boundary position defined by the residual. The fuzzy rule is shown in Fig. 8.3.

The two physical objective functions f_3 and f_4 have lower refenrence value, which corresponds to membership functions equal to 0, defined by substituting in Eq. 8.7 and Eq. 8.8 the coils current reference values of the analyzed plasma equilibrium. The higher reference value is equal to 1 which correpond to be in the worst case. The lower and higher values for Divertor plasma equilibrium are listed in Tab. 8.1. The f_3 and f_4 fuzzy rules and membership functions are respectevely shown in Fig. 8.4 and Fig. 8.5.

The final single objective function which is to be minimized is obtained by using logical "and" operation which correspond to adding up all the four membership functions:

$$f = z_1 + z_2 + z_3 + z_4 + z_5 \tag{8.9}$$

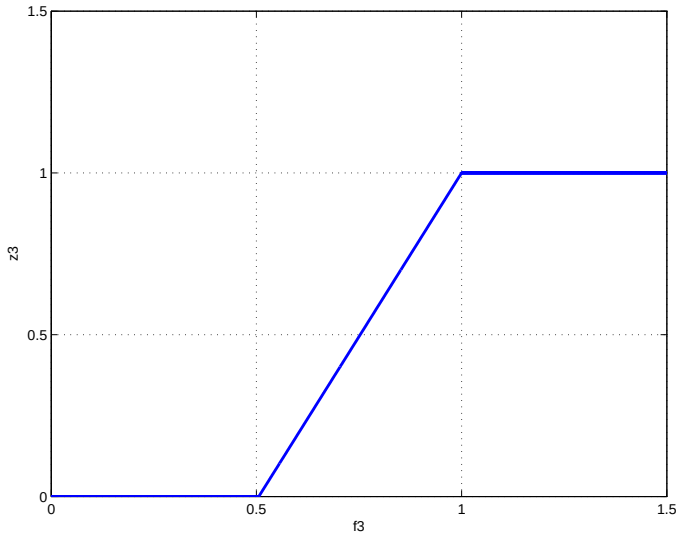

Figure 8.4: Fuzzy rule for f_3 objective function

8.4 Optimization strategy

The sigle objective function defined in Eq. 8.9 can be minimized by using an optimization approach based on evolutionary/metaheuristic alghorithms. In particular the evolutionary metaheuristic algorithm "Differential Evolution" and the swarm evolutionary "Particle Swarm Optimization" has been used for the solution of the problem. The use of evolutionary algorithms (EAs) to solve problems of this nature has been motivated mainly because of the population-based nature of EAs which allows the generation of several elements in a single run.

The two algorithms has been used in order to improve the initial solution based on the SVD technique with two different approaches: the first one is determined by using the DE and PSO algorithm with random initialization of the population. The second approach involves the use of the SVD solution as first known good point for the populations of the algoirthms. The two results has been compared between the SVD solution and a reference equilibrium solution. The optimization analysis has been execute to a Divertor plasma equilibrium. Further optimization analysis has been conducted for the reference Limiter plasma equilibrium and for a generated plasma based on the reference Limiter equilibrium by using the analytical functional model. These results are reported in App. A.1 and App. A.3.

8.4.1 Differential Evolution

Differential Evolution (DE) is an evolutionary (direct- search) algorithm which performs mutation based on the distribution of the solutions in the current population. In this way, search directions and pos- sible step sizes depend on the location of the individuals selected to calculate the mutation values. There is a nomenclature scheme developed to reference the different DE variants. The most popular is called "DE/rand/1/bin", where "DE" means Differential Evolution, the word "rand" indicates that individuals selected to compute the mutation values are chosen at random, "1" is the number of pairs of solutions chosen and finally "bin" means that a binomial recombination is used. It is important to note that, increasing either the population size or the number of pairs of solutions

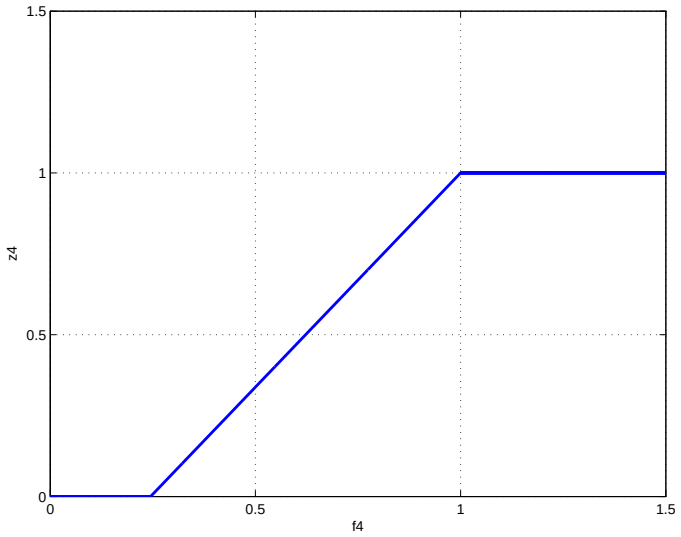

Figure 8.5: Fuzzy rule for f_4 objective function

to compute the mutation values will also increase the diversity of possible movements, promoting the exploration of the search space. However, the probability to find the correct search direction decreases considerably [19]. Another important factor when using DE is the selection of the variant. Each one varies the way mutation is computed and also the type of recombination operator. The "CR" parameter controls the influence of the parent in the generation of the offspring. Higher values mean less influence of the parent. The "F" parameter scales the influence of the set of pairs of solutions selected to calculate the mutation value

In this study the "DE/best/1/bin" has been used: the "rand" variants select all the individuals to compute mutation at random and the "best" variants use the best solution in the population besides the random ones.

8.4.2 Particle Swarm Optimization

The idea of this approach is to simulate the movements of a group (or population) of birds which aiming at finding food. The approach can be seen as a distributed behavioral algorithm that performs (in its more general version) multidimensional search. The behavior of each individual (or particle) is affected by either the best local (i.e., within a certain neighborhood) or the best global individual. The approach uses then the concept of population and a measure of performance similar to the fitness value used with evolutionary algorithms. Also, the adjustments of individuals are analogous to the use of a crossover operator. Additionally, this approach introduces the use of flying potential solutions through hyperspace (used to accelerate convergence). Note that PSO allows individuals to benefit from their past experiences whereas in an evolutionary algorithm, normally the current population is the only "memory" used by the individuals [19].

8.5 Results

The fuzzy approach to the opimization problem is necessary to redefine it in order to find a set of "good" solutions. The problem has two different class of objective functions: the first is related

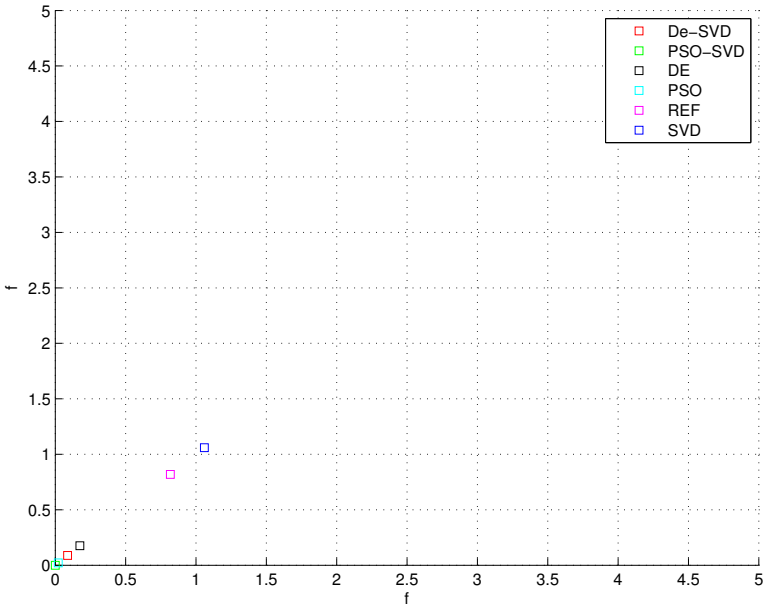

Figure 8.6: Objective function f space

to the physical feasibility of the solution and it is expressed by the objective functions f_3 and f_4 related to the coils currents values. The second one is the accuracy class of functions, f_1, f_2 and f_5 which provide the accuracy level of the residual and therefore on the magnetic flux values at the boundary. By analyzing the reference equilibrium solution it is possible to see the rigidity of the problem: those reference set of currents are a compromise between the accuracy and the physical feasibility. The "utopia" point in absolute terms is not considered in the solution of this class of inverse problems. Despite this, the "utopia" point in relative terms, i.e. related to the objective function f which results from the fuzzy logic, is considered but not as the most important factor. The variations of the single objective functions inside the intervals defined by the fuzzy rule are not considered because their value are imposed to be equal to 0 if the value is minor than the lower limit, a linear combination if it is between the lower and the higher limit and equal to 1 if it is greater than the higher limit.

The analysis of the results is done with a double focus: the minimization of the total objective function f and the minimization of the single objective functions values f_i, with $i = 1, 2, 3, 4, 5$, for each solution found. In other words it is important to see the quality of the solutions in terms of accuracy and physical feasibility as well as in absolute terms. The SVD solution has been set as reference value for the comparison between the evolutionary algorithm solutions obtained with the two different approaches of simple random generation and random generation with SVD solution as first known good point. The four different solutions are labelled as "DE", "PSO", "DE-SVD" and "PSO-SVD". An additional information is the reference equilibrium set of currents solution which is labelled as "REF".

The values of the main objective function f, for the four different solutions, are shown in Fig. 8.6 for the Divertor plasma equilibrium. The SVD solution, which is set as the reference, is the worst one in absolute terms. The reference solution is better than it as shown in Fig. 8.6 and in the first column of Tab. 8.3. Several evolutionary solutions found the zero value of f but with

Algorithm	ϵ_f
$DE-SVD$	91.6745
$PSO-SVD$	100
DE	83.4649
PSO	97.9732

Table 8.2: Main objective function f per cent values

Solution	f	z_1	z_2	z_5	z_3	z_4
SVD	1.0601	0	0	0	0.6665	0.3936
REF	0.8182	0.2017	0.3618	0.2547	2.3701e-05	0
$DE-SVD$	0.0883	0.0093	0.0566	0.0224	0	0
$PSO-SVD$	0	0	0	0	0	0
DE	0.1753	0.0361	0.0991	0.0401	0	0
PSO	0.0215	0	0.0215	0	0	0

Table 8.3: Global f and related membership values for each solution

this analysis it is impossible to see how this minimum point is reached. The values of the singular objective functions are not shown and therefore it is possible for a solution to give a high improve in the accuracy but with an equally aggravation of the physical feasibility. The per cent values of the evolutionary f related to the SVD total objective function values can be expressed as:

$$\epsilon_f = \frac{f_{SVD} - f^*}{f_{SVD}} 100 \tag{8.10}$$

where f^* is the objective function value reached by using one of the evolutionary algorithms and f_{SVD} is the value of the objective function by using the SVD solution. The per cent optimization values are listed in Tab. 8.2. It is possible to see from Tab. 8.3 and Fig. 8.6 that only the PSO-SVD algorithm reaches the "relative utopia" point, $f = 0$, which does not corresponds to the absolute utopia point in which all the objective functions should be zero. The relative utopia point is reached when all the membership functions z_i are equal to zero which means that all the objective functions f_i are within the desired limits. The total results of the optimization process are shown in Tab. 8.4, where it is possible to see the partial values of the five objective functions for all different solutions in the Divertor equilibrium case.

In order to analyze the optimization in the relative sense, which means with respect of the single objective functions values expressed in Tab. 8.4, the variation of these values with respect of the reference SVD solution has been expressed in a per cent form, each one referred to the different

Solution	f_1	f_2	f_5	f_3	f_4
SVD	0.0016	0.0025	0.0016	0.8352	0.5419
REF	0.0382	0.0607	0.0457	0.5058	0.2446
$DE-SVD$	0.0113	0.0179	0.0131	0.3727	0.1535
$PSO-SVD$	0.0056	0.0089	0.0062	0.4712	0.2305
DE	0.0151	0.0239	0.0156	0.3979	0.2269
PSO	0.0082	0.0130	0.0088	0.3767	0.1750

Table 8.4: Objective functions values for each solution

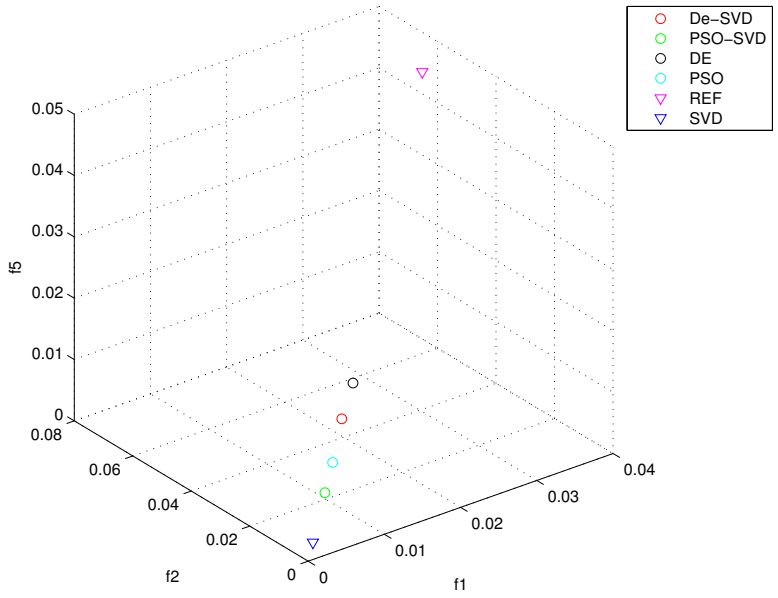

Figure 8.7: f_1 f_2 f_5 space

Solution	σ_{f_1}	σ_{f_2}	σ_{f_5}	σ_{f_3}	σ_{f_4}
$DE-SVD$	-0.9691	-1.5370	-1.1497	46.2466	38.8461
$PSO-SVD$	-0.4013	-0.6365	-0.4519	36.3967	31.1399
DE	-1.3448	-2.1330	-1.3963	43.7251	31.5051
PSO	-0.6595	-1.0460	-0.7135	45.8464	36.6933

Table 8.5: Objective functions variations per cent values for each solution

normalization value:

$$\sigma_{f_i} = (f_{iSVD} - f_i^*)100 \tag{8.11}$$

where f_{iSVD} is the i-th objective function for the SVD solution, f_i^* is the i-th objective function for the evolutionary solution with $i = 1, 2, 3, 4, 5$. It is important to note that the values defined in Eq. 8.11 can be positive or negative which means respectevely that the i-th objective function of the SVD solution has been improved or degradated.

The five dimensional space of the objective functions can be split into a bidimensional space for the physical feasibility objective functions f_3, f_4 and a three dimensional space for the accuracy set of objective functions f_1,f_2 and f_5. The values of the objective functions in Tab. 8.4 can be represented in these two spaces as shown in Fig. 8.7 and Fig. 8.8. It is notable from Fig. 8.7 and Fig. 8.8 that the SVD solution is the best solution in terms of accuracy but the worst in therms of physical feasibility. An opposite behaviour is denoted for the reference solution which is more focused on the feasibility of the solution rather than the accuracy on the residual.

The behaviour of a solution in the accuracy space is the opposite in the physical feasibility space. For example the PSO-SVD solution is one of the best in terms of accuracy, and also in global terms of f, but it results as the worst in terms of physical feasibility. Its objective functions f_3 and f_4 are slightly minor than, respectively, the 50 and 30 per cent of the worst case. The same analysis but with opposite behaviours can be done for the DE-SVD solution which provide one of

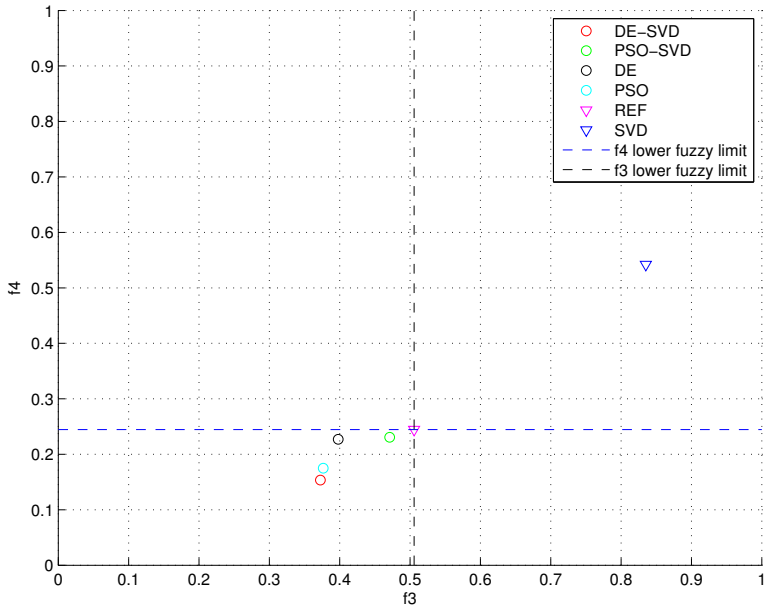

Figure 8.8: f_3 f_4 space

Solution	$\sum_1^4 \sigma_{f_i}$
$DE-SVD$	81.4370
$PSO-SVD$	66.0468
DE	70.3561
PSO	80.1208

Table 8.6: Optimization global per cent results for the objective functions

the best physical feasibility solution but with worst accuracy on the residual. In order to compare the solutions in the two different spaces, the variations defined in Eq. 8.11 has been expressed in per cent with respect of each normalization value. The results are listed in Tab. 8.5 where the previous considerations are more evident and readable.

Since the SVD solution is the best in terms of accuracy it is clear that the aim of the optimization is to make this solution more feasible with the lowest decay in terms of accuracy. In other words the optimization procedure has to provide the highest positive variations for the f_3 and f_4 functions with the lowest negative variations for the accuracy set of functions f_1,f_2 and f_5. This analysis can be done by adding together the variations values of Tab. 8.5 for each solution and by compare these results, which are listed in Tab. 8.6. It can be noticed that the DE-SVD offers the best compromise between the improvement of feasibility and decay of accuracy, followed by the PSO, DE and PSO-SVD.

Other results can take into account the global optimization of the total objective function f with respect of the SVD solution: this can be done by adding for each type of solution the percent values in Tab. 8.6 with the percent values in Tab. 8.2. The solution that gives the highest total improvement to the main and singular objective functions, which means that gives the large improvements in the f and the best balance between feasibility improvements and accuracy decay, is the PSO followed by DE-SVD, PSO-SVD and the DE.

Chapter 9

Conclusions

The aim of this study is to provide numerical solutions of the Inverse equilibrium problem for magnetically confined fusion plasmas with an optimization approach based on fuzzy logic and evolutionary/metaheuristic algorithms. The problem requires to identificate the optimal values for the active coils currents in order to keep in equilibrium a plasma with a prescribed magnetic configuration (i.e. plasma shape and global parameters, namely I_p, li, β_p). The objective function has been splitted into two sets of objective functions: the first is the "accuracy set" defined by three objective functions for the residual. The second one is the "physical feasibility set" defined by two objective functions for the coils currents constrained values. The optimization procedure is able to provide a family of feasible solutions starting from the unfeasible SVD solution with an accuracy between the 1 and the 15 per cent on the residual. The solutions found are better than the reference set of coils currents in terms of accuracy and physical feasibility. This last aspect is extremely important because it is related to the electrodynamic forces on the conductors and the power dissipation: it involves engineering and physics aspects that are crucial for the correct operations of the magnetic confinement device. The optimiation has been obtained for both Limiter and Divertor plasma equilibria. The optimization process is important to show the rigidity of the problem and the extremely dependence of the results on the values assumed by the fuzzy logic lower limits. The acceptable values for the objective functions are in fact determined by these lower limits. The optimization results for the Limiter case are reported in App. A.1.

Additional results has been reached by using the analytical functional model, which provide the means to generate a family of solutions by varying only a single parameter: it is possible to generate a series of boundaries where the "freedom parameter" is changed but the remaining shape parameters are fixed. These variations can then be used to determine whether the distribution of coil currents required to make a desired shape that has not been made previously are within the capabilities of a given coil set. A further optimization process, which is reported in App. A.3, has been applied to a plasma boundary generated by the analytical functional model by using the Limiter plasma equilibrium as starting point. The equilibirum of the plasma characterized by this new plasma boundary has been studied as in Chap. 7 in order to determine the coils contribution to the magnetic flux at the boundary and the coils Green matrix, which are necessary to solve the inverse equilibrium problem with the optimization procedure. The fixed boundary problem for this new plasma boundary is solved in App. A.2.

A suggestion for the future is to include the squareness parameter, which is given by the analytical functional model, in the optimization process as a degree of freedom: by relaxing this

parameter it could be possible to obtain better results in terms of accuracy an feasibility. Furthermore it would be interest to study the variations on the current values distribution by varying the plasma global parameters. In other words, variations on the p', FF' profiles (or the li, β_p) change the plasma equilibrium and it modify the computed active coils currents values. Future works may be also focused on the application of the procedure developed in this thesis to real experiments, e.g. RFX-mod machine, a medium size device which can operate both as Tokamak and RFP. In particular the proposed procedure could be used for the sinthesys of the equilibrium currents of the field shaping coils for Tokamak operations with circular plasmas and shaped plasmas with single or double null point.

Appendix A

Additional results

A.1 Optimization of the limiter plasma case

The optimization of the Limiter plasma equilibrium coils currents has been done with the same procedure adopted for the divetor case. The previous lower and higher limits to define the membership functions, introduced in Sect. 8.3, has been modified because they were too restictive for physical feasibility and residual accuracy. It is shown in Fig. A.1 and Fig. A.2 that the only solution that stays under the physical feasibility lower limits is the PSO solution which, at the same time, does not respect the residual limits. This fact is evident and quantifiable in Tab. A.1 where it can be noticed that the PSO solution is not able to match the residual limits. Another important consideration is that even the REF solution is far from respecting these limits that are too restrictive for this plasma equilibrium. All the method, excepted the PSO-SVD, can not fully improve the SVD solution as shown in Tab. A.2. The SVD solution is slightly improved in the physical feasibility, which means an improve on the f_3 and f_4 functions, by the PSO-SVD, PSO and DE as shown in Tab. A.3. The DE-SVD equals the SVD solution. The only method which improve the f_3 and f_4 functions without an excessevely decay on the other three objective functions is the PSO-SVD. All the other methods can't improve the physical aspects of the solution without degrade the accuracy on the residual. The values assumed by each objective function for the different solutions are listed in Tab. A.4 which shows that the SVD values in accuracy are better than the REF solution and the physical feasibility is slightly worse only for the dipole term. This term varies from the 0.0673 of the REF solution to the 0.1138 of the SVD which is 5 per cent worse. The SVD solution is therefore already a good solution for the Limiter plasma equilibrium problem since it shows a good accuracy on the residual's objective functions (f_1, f_2,

Solution	f	z_1	z_2	z_5	z_3	z_4
SVD	0.8819	0.0032	0	0.8288	0	0.0499
REF	3.0000	1	1	1	2.4773e-05	0
$DE-SVD$	0.8819	0.0032	0	0.8288	0	0.0499
$PSO-SVD$	0.1835	0.0115	0	0.1238	0	0.0481
DE	2.4211	0.8331	0.5715	1	0	0.0165
PSO	3	1	1	1	0	0

Table A.1: Global f and related membership values for each solution

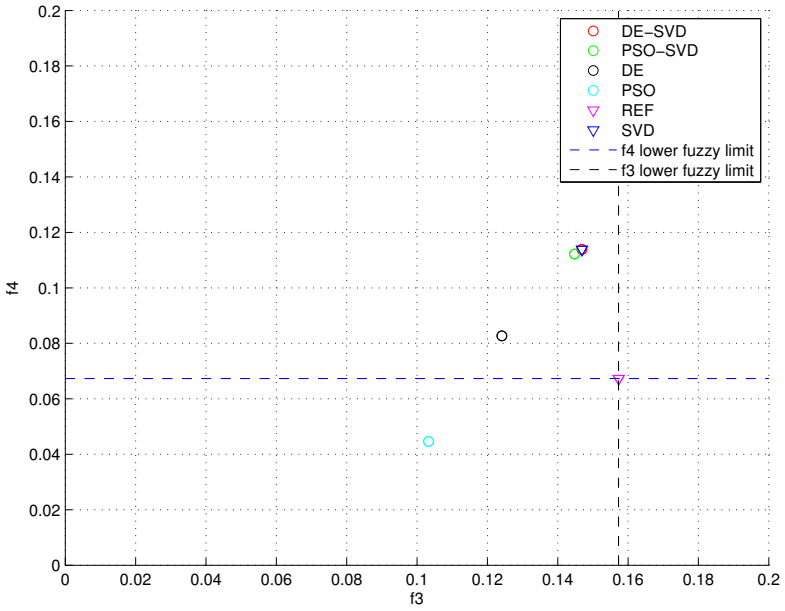

Figure A.1: f_1 f_2 f_5 space

Algorithm	ϵ_f
$DE-SVD$	0
$PSO-SVD$	79
DE	-175
PSO	-240

Table A.2: Main objective function f per cent values

f_5) and acceptable values on the feasibility objective functions f_3 and f_4, as listed in Tab. A.4.

A.2 Solution of the fixed boundary equilibrium problem for a plasma generated by the analytical functional model

The fixed boundary problem has been solved for the generated plasma boundary obtained by using the analytical functional model. The squareness values for the new Limiter plasma boundary are listed in Tab. A.5 and they are the same of the original Limiter plasma but instead to be negative they have been changed to be positive: this means that the boundary is more square than the reference ellipse. The mesh related to this new plasma boundary is shown in Fig. A.4.

Solution	σ_{f_1}	σ_{f_2}	σ_{f_5}	σ_{f_3}	σ_{f_4}
$DE-SVD$	0	0	0	0	0
$PSO-SVD$	-0.1164	-0.0827	9.8692	0.2114	0.1652
DE	-11.6188	-8.2582	-438.9740	2.2774	3.1170
PSO	-554.3278	-393.9985	-19197	4.3597	6.9208

Table A.3: Objective functions variations per cent values for each solution

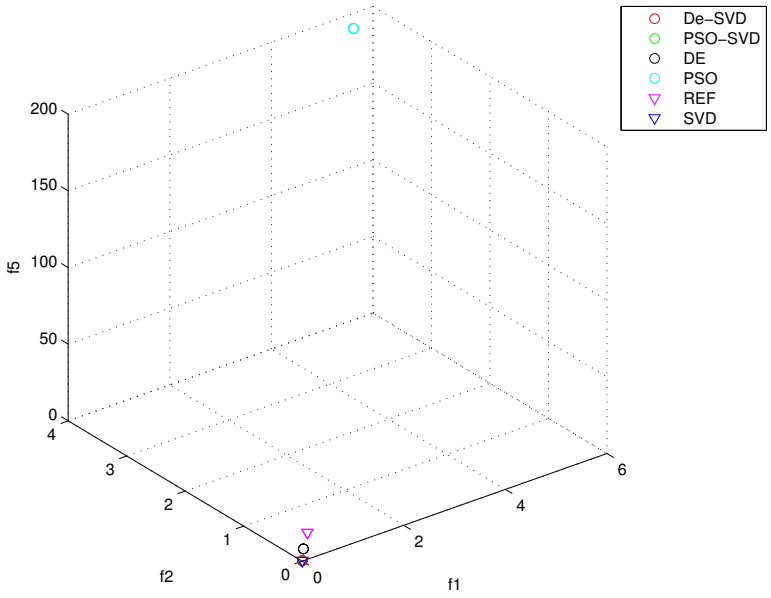

Figure A.2: f_3 f_4 space

Solution	f_1	f_2	f_5	f_3	f_4
SVD	0.0104	0.0074	0.1260	0.1469	0.1138
REF	0.5648	0.4014	2.9275	0.1573	0.0673
$DE-SVD$	0.0104	0.0074	0.1260	0.1469	0.1138
$PSO-SVD$	0.0116	0.0083	0.0273	0.1448	0.1122
DE	0.1266	0.0900	4.5158	0.1241	0.0827
PSO	5.5537	3.9474	192.0979	0.1033	0.0446

Table A.4: Objective functions values for each solution

The solution of the problem follows the same steps of Chap. 7 and reaches the convergence after 4 iterations with a magnetic flux error at axis equal to 3.1425 and a Picard error equal to 0.72102. The convergence is shown in Fig. A.6 for the Picard error and in Fig. A.7 for the magnetic flux error at axis.

The magnetic flux surfaces for the first and final solution are shown in Fig. A.5, Fig. A.8 and Fig. A.9.

	ξ_I	ξ_{II}	ξ_{III}	ξ_{IV}
$referenceLimiter$	-0.0749	-0.0235	-0.0707	-0.1075
$newLimiter$	0.0749	0.0235	0.0707	0.1075

Table A.5: Optimization results

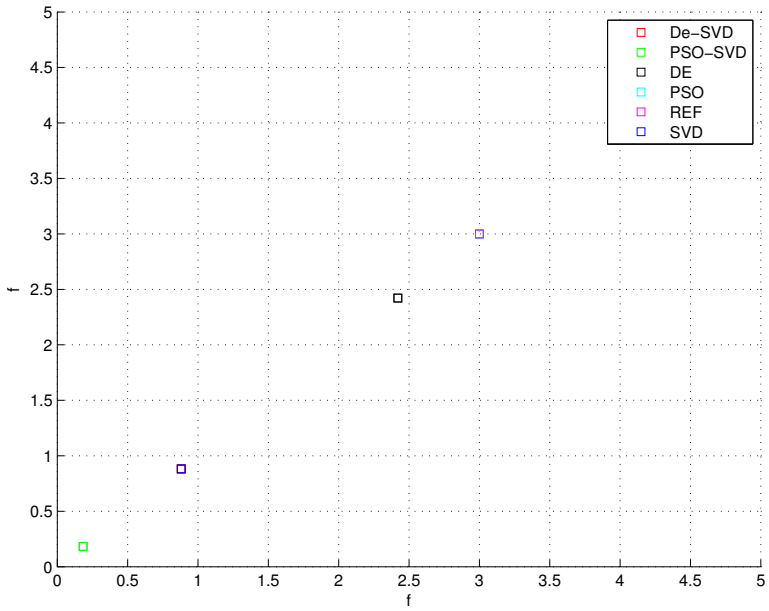

Figure A.3: Objective function f space

Solution	f	z_1	z_2	z_5	z_3	z_4
SVD	2	0	0	0	1	1
REF	3	1	1	1	2.4773e-05	0
$DE-SVD$	1.3224	0.1584	0.0502	1	0.0414	0.0725
$PSO-SVD$	0	0	0	0	0	0
DE	1.3168	0.2221	0.0947	1	0	0
PSO	0.0514	0.0240	0	0.0274	0	0

Table A.6: Global f and related membership values for each solution

A.3 Inverse equilibrium problem for a plasma generated by the analytical functional model

The solution of the inverse equilibrium problem for a plasma with a boundary generated by using the analytical functional model described in Chap. 2 follows the same steps already seen in Chap. 8 and App. A.1. The generated plasma is the same of the fixed boundary equilibirium problem solution in App. A.2, and it is easy to expect that, because of its shape, the SVD solution for the coil currents can not satisfy both accuracy and physical feasibility objective functions limits. This fact is reported in Tab. A.6 where it is possible to notice the classic behaviour of the SVD solution which respects the accuracy limits but not the physical ones. The unfeasable character of the SVD solution can be also noticed in Fig. A.11 while the good accuracy of this solution is visible in Fig. A.10. It is important to say that the REF solution is considered in this analysis only in terms of physical feasibility, because it is referenced to the reference Limiter plasma equilibrium which is characterized by a different plasma boundary: the lower fuzzy limit in the feasibility of the coil currents can be set by using the values of the REF solution which correspond to the 10.2 per cent for the f_3 objective function and the 6.38 per cent for the f_4 objective function. The percentage

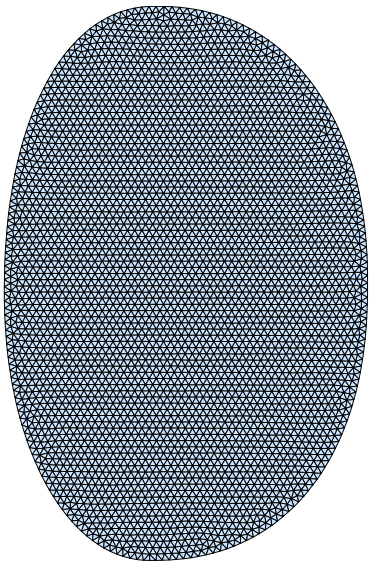

Figure A.4: Mesh of the generated plasma region

Algorithm	ϵ_f
$DE-SVD$	33.8801
$PSO-SVD$	100
DE	34.1587
PSO	97.4298

Table A.7: Main objective function f per cent values

values are both referred to the worst case of f_3 and f_4.

The improvements on the SVD main function f can be expressed in absolute terms, as in Tab. A.6, and in percent terms, as in Tab. A.7, dor each type of solution. It can be noticed that the PSO and the PSO-SVD solutions reaches the "relative utopia point" for the objective function f. It is important to see how this point is reached which means how the optimization process improves or degrades the single objective functions. This can be done by analyzing the per cent variations of the single objective functions values with respect of the reference SVD solution; in Tab. A.8 and Tab. A.9 are respectevely listed the absolute and percent values of the single objective functions for each solution. From Tab. A.9 and Fig. A.10 it is clear that each solution degrades the SVD solution in terms of accuracy but improve it in terms of physical feasibility. The solution with the

Solution	f_1	f_2	f_5	f_3	f_4
SVD	0.0092	0.0065	0.0245	1.2159	1.1134
$DE-SVD$	0.0896	0.0625	2.1207	0.1922	0.1349
$PSO-SVD$	0.0331	0.0231	0.0499	0.1020	0.0638
DE	0.1055	0.0737	1.0875	0.0413	0.0121
PSO	0.0560	0.0391	0.0569	0.0491	0.0288

Table A.8: Objective functions values for each solution

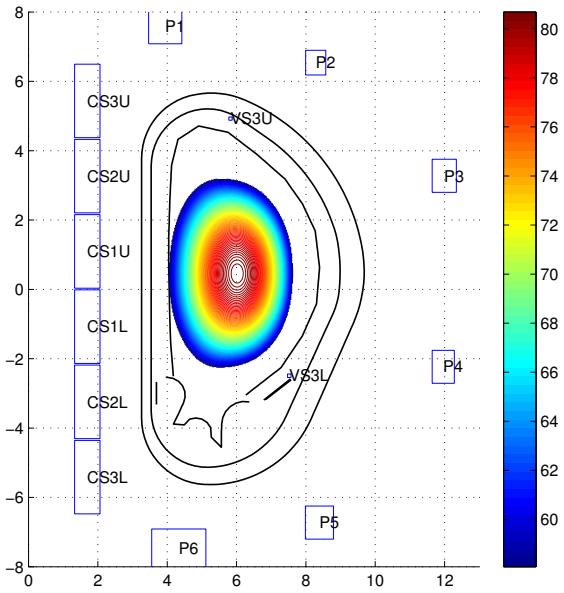

Figure A.5: Magnetic flux surfaces of the first initial solution for the generated plasma

Solution	σ_{f_1}	σ_{f_2}	σ_{f_5}	σ_{f_3}	σ_{f_4}
$DE-SVD$	-8.0353	-5.6095	-209.6179	102.3707	97.8517
$PSO-SVD$	-2.3857	-1.6655	-2.5393	111.3866	104.9637
DE	-9.6293	-6.7222	-106.3003	117.4535	110.1307
PSO	-4.6755	-3.2640	-3.2367	116.6786	108.4609

Table A.9: Objective functions variations per cent values for each solution

better response in total sense is the one which provides the higher positive variaions for the f_3 and f_4 functions with the lowest negative variations for the accuracy set of functions f_1,f_2 and f_5. Tab. A.10 indicates the PSO and the PSO-SVD as the two best solutions in this terms. By adding for each solution the per cent values of the main objective function optimization, which are reported in Tab. A.7, with the values of Tab. A.10 it is possible to determine the solutions which gives the large improvements in the f and the best balance between feasibility improvements and accuracy decay which are the PSO and the PSO-SVD.

Solution	$\sum_1^4 \sigma_{f_i}$
$DE-SVD$	10.8399
$PSO-SVD$	309.7597
DE	139.0911
PSO	311.3930

Table A.10: Optimization global per cent results for the objective functions

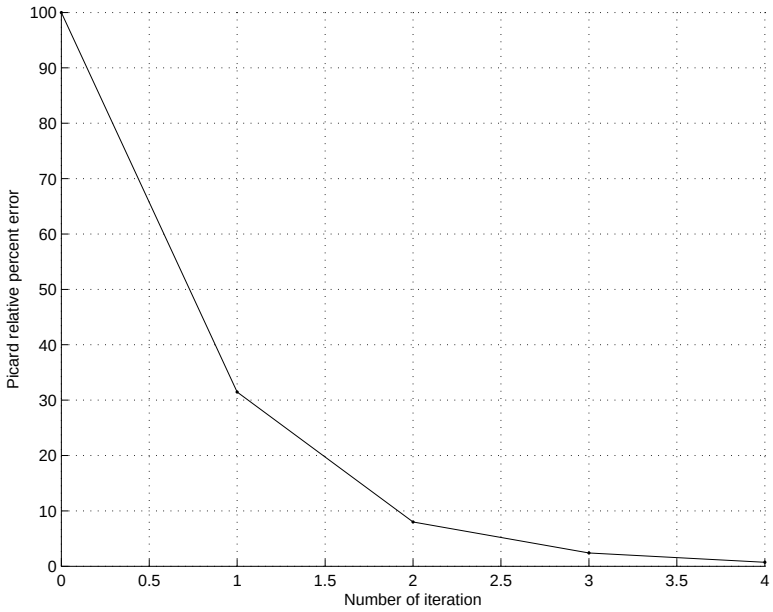

Figure A.6: Relative percent error generated plasma equilibrium

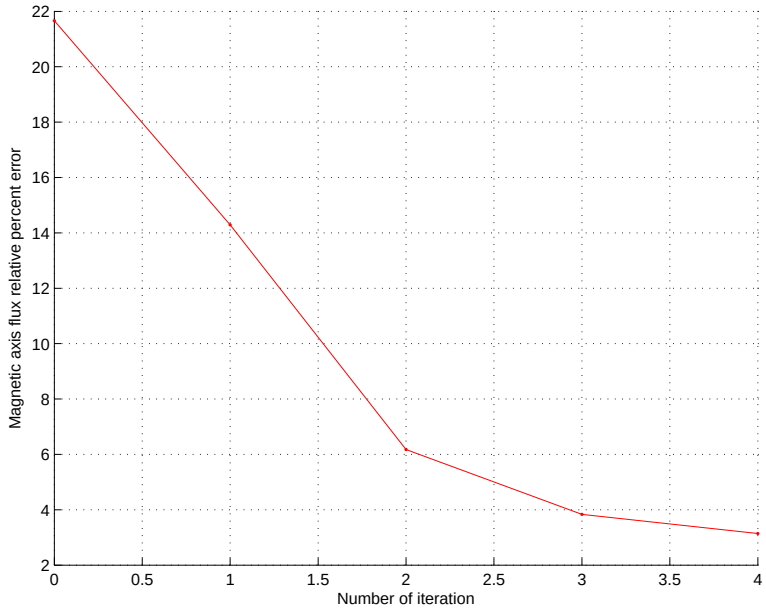

Figure A.7: Relative magnetic axis percent error generated plasma equilibrium

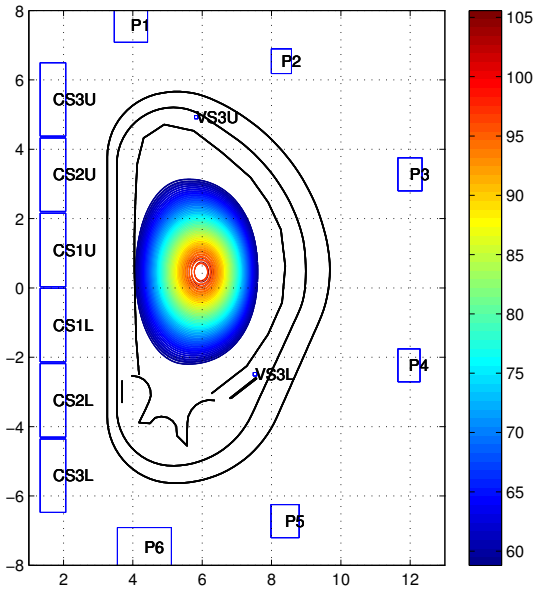

Figure A.8: Magnetic flux surfaces for the final solution of the generated plasma equilibrium

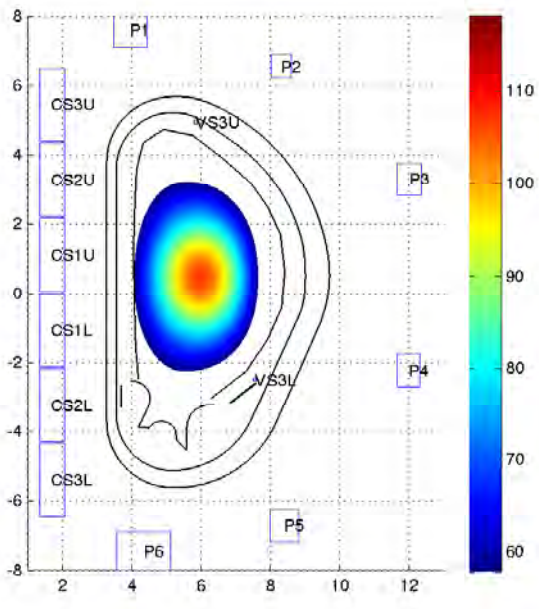

Figure A.9: Magnetic flux patch of the final solution for the generated plasma equilibrium

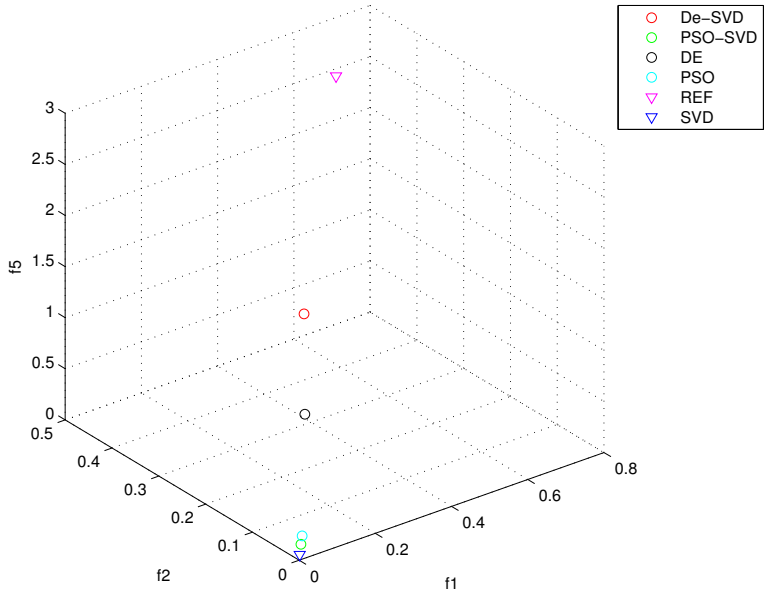

Figure A.10: f_1 f_2 f_5 space

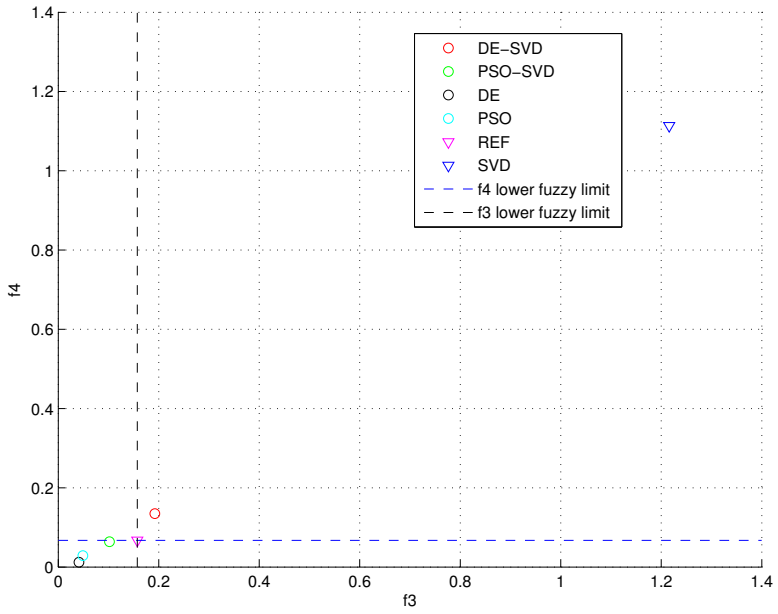

Figure A.11: f_3 f_4 space

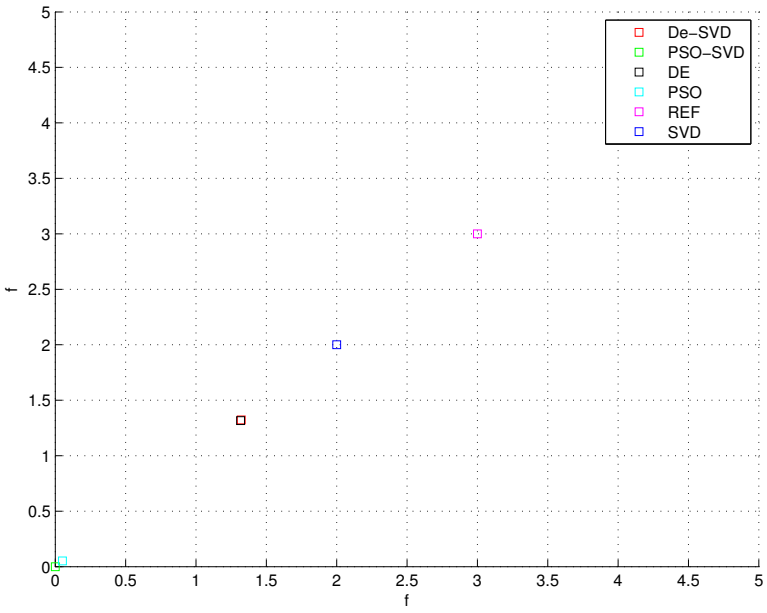

Figure A.12: Objective function f space

Bibliography

[1] Alessandro Beghi and Angelo Cenedese, "Advances in real-time plasma boundary reconstruction," *IEEE Control Systems Magazine*, Vol. 25, 2005.

[2] Mitsuru Kikuchi, Karl lackner, and Mihn Quang Tran, "Fusion Physics," Tech. rep., IAEA - International Atomic Energy Agency, 2012.

[3] Freidberg, J. P., *Plasma physics and fusion energy*, Cambridge University Press, 2008.

[4] Wesson, J., *Tokamaks*, Clarendon Press - Oxford, 2004.

[5] Tonti, E., *The Mathematical Structure of Classical and Relativistic Physics*, Springer Science+Business Media, 2010.

[6] Tatsuoki Taked and Shinji Tokuda, "Computation of MHD Equilibrium of Tokamak Plasma," *Journal of computational physics, 93, 1-107*, 1990.

[7] Portone, A., "Ideal MHD Equilibria Of Tokamak Plasmas," Tech. rep., Fusion for Energy, C. Josep Pla 2, B3, 11/18, 08019 Barcelona (Spain).

[8] T C Luce, "An analytical functional form for characterization and generation of axisymmetric plasma boundaries," *Plasma physics and controlled fusion*, Vol. 55, 2013.

[9] Gabriel Lamé, "Examen des différentes méthodes employées pour résoudre les problémes de geometrie," *Paris*, 1818.

[10] Angelo Cenedese, Filippo sartori, Gabriella Saibene, and Mario Cavinato, "Analysis of real time magnetic reconstruction in ITER," Tech. rep., Fusion For Energy.

[11] Thomas Sederberg, "BYU Bézier curves," Tech. rep., http://www.tsplines.com.

[12] Salomon, D., *Curves and Surfaces for Computer Graphics*, Springer, 2006.

[13] Pastva, T. A., *Bézier curve fitting*, Master's thesis, Mater's Thesis, Naval Postgraduate School, Monterey, California, 1998.

[14] Persson, P.-O., *Mesh Generation for Implicit Geometries*, Ph.D. thesis, Department of Mathematics, MASSACHUSETTS INSTITUTE OF TECHNOLOGY, 2005.

[15] Kiusalaas, J., *Numerical methods in engineering with MATLAB*, Cambridge University Press, 2005.

[16] V. D. Shafranov and L. E. Zakharov, "Equilibrium of current-carrying plasmas in toroidal configurations," *Reviews of plasma physics, Vol. II*, 1982.

[17] Dolan, T. J., *Fusion Research*, Pergamon Press, 2000.

[18] S.N. Sivanandam, S. Sumathi, and S.N. Deepa, *Introduction to Fuzzy Logic using MATLAB*, Springer Science+Business Media, 2007.

[19] Carlos A. Coello Coello, Gary B. Lamont, and David A. Van Veldhuizen, *Evolutionary Algorithms for Solving Multi-Objective Problems*, Springer Science+Business Media, 2007.